eman ta zabal zazu

Universidad del País Vasco
Euskal Herriko Unibertsitatea

Doctoral Thesis

HIGH FIELD, HIGH FREQUENCY AND TEMPERATURE ADJUSTABLE AC MAGNETOMETER FOR MAGNETIC HYPERTHERMIA CHARACTERIZATION

Author:
IRATI RODRIGO ARRIZABALAGA

Supervisors:
FERNANDO PLAZAOLA MUGURUZA
JOSÉ ÁNGEL GARCÍA MARTÍNEZ

2020

Resumen

El cáncer es, por su naturaleza, una enfermedad increíblemente resistente y, por lo tanto, increíblemente compleja.

Se estima que en 2017, 9.6 millones de personas fallecieron por cáncer, convirtiéndola así en la segunda causa de muerte en el mundo.

La investigación en el campo de la oncología, se centra principalmente en el desarrollo de técnicas alternativas de diagnóstico y terapia, con el fin de tratar cánceres que los tratamientos convencionales como la quimioterapia, la radioterapia y la cirugía no pueden de curar.

Varias terapias alternativas como la inmunoterapia, la terapia génica y la hipertermia magnética están siendo actualmente desarrolladas en laboratorios y hospitales.

La hipertermia magnética, es una terapia innovadora contra el cáncer, que consiste en destruir células cancerosas mediante el uso de nanopartículas magnéticas. Éstas, son situadas estratégicamente en los tejidos tumorales y posteriormente, son calentadas mediante la aplicación de un campo magnético alterno de frecuencias comprendidas entre 100 kHz y 1 MHz. El calor generado por las nanopartículas incrementa la temperatura de los tejidos tumorales lo que termina destruyendo el cáncer. A diferencia de otras terapias oncológicas, la hipertermia magnética tiene el potencial de atacar selectivamente, los tejidos cancerígenos sin dañar los sanos y sin necesidad de cirugía.

Para poder diseñar un buen tratamiento de hipertermia, es crucial estudiar varios parámetros a definir durante el mismo, entre ellos la tasa de absorción específica (en inglés, specific absorption rate (SAR)). Este parámetro, mide la cantidad de energía que absorben las nanopartículas por unidad de masa y es altamente dependiente de las propiedades intrínsecas de éstas. El SAR se puede medir mediante dos métodos distintos: calorimetría y magnetometría de corriente alterna (CA).

La calorimetría consiste en medir el aumento de temperatura de las nanopartículas al aplicarle un campo magnético alterno. Aunque la calorimetría es el método más

empleado, la dificultad de diseñar equipos adiabáticos, proporciona valores imprecisos del *SAR*.

La magnetometría CA, por otra parte, se basa en la determinación de la magnetización dinámica de las nanopartículas, cuando son excitadas por un campo magnético alterno. En este método, el *SAR* se calcula a partir del área de los ciclos de histéresis. La magnetometría CA surge como un método reproducible, rápido y preciso. Además, proporciona información magnética adicional que no es accesible mediante la calorimetría, ya que, la determinación del ciclo de histéresis, contiene mucha mas información que simplemente el valor del *SAR*.

En los últimos años, se han diseñado diversos magnetómetros CA que trabajan en distintas intensidades y frecuencias de campo. Aunque estos magnetómetros CA miden la magnetización de manera diferente, todos ellos tienen una arquitectura similar. Por una parte, cuenta con un generador de campo magnético alterno y por otra, con un sistema de detección de la magnetización de las nanopartículas. Generalmente el campo magnético es creado mediante el uso de solenoides y la magnetización de las nanopartículas es medida con bobinas captadoras.

La presente Tesis proporciona un estudio completo del desarrollo de un nuevo magnetómetro CA y su potencial, tras haber realizado un estudio exhaustivo de las limitaciones de la instrumentación existente.

El trabajo se divide en tres bloques principales, precedidos por una introducción de la hipertermia magnética.

En el primer bloque (Capítulo 3) se han realizado medidas de magnetometría CA para analizar cómo afectan las características de las nanopartículas magnéticas en su calentamiento. Además, se ha podido observar, que la instrumentación existente de magnetometría CA tiene ciertas limitaciones que restringen el estudio del comportamiento magnético de las nanopartículas.

El segundo bloque (Capítulo 4) se centra en el diseño, implementación y caracterización de un magnetómetro CA, que pretende subsanar las limitaciones observadas en el bloque anterior.

Finalmente, el último bloque (Capítulo 5) está dirigido al estudio de la potencialidad del magnetómetro CA diseñado en esta tesis. A continuación, se presentan los resultados y conclusiones obtenidos en cada uno de los bloques.

Para lograr un tratamiento de hipertermia magnética eficiente, las nanopartículas tienen que generar tanto calor como sea posible, para poder así disminuir la cantidad de nanopartículas inyectadas en el paciente.

Comprender los parámetros que aumentan el *SAR* es vital para poder diseñar nanopartículas con un calentamiento óptimo.

Como se ha mencionado previamente, el *SAR*, depende en gran medida de las propiedades fisicoquímicas de las nanopartículas, como por ejemplo, la composición, el tamaño, la forma y la cristalinidad. Además, los arreglos formados por interacciones dipolares también afectan al comportamiento del calentamiento de las nanopartículas.

En general, se ha demostrado que las interacciones dipolares disminuyen el *SAR*. Sin embargo, se ha estudiado que algunos arreglos específicos, como las cadenas, aumentan la eficiencia de calentamiento debido a su capacidad de orientarse con el campo magnético aplicado.

Por otra parte, los medios de dispersión de las nanopartículas también juegan un papel importante en el *SAR*. Los medios con viscosidad alta, como el medio celular, tienden a disminuir considerablemente el *SAR*, bien por la formación de arreglos o la supresión de la rotación de las nanopartículas.

Con el fin de explorar el potencial de la magnetometría CA, en el Capítulo 3, se han estudiado el comportamiento magnético de distintas nanopartículas mediante esta técnica.

De esta manera, se ha deducido que el origen de la alta capacidad de calentamiento de la bacteria magnetotáctica *Magnetospirillum gryphiswaldense*, viene dado por la habilidad de ésta para alinearse con el campo magnético aplicado.

Por otra parte, también se ha podido observar que la forma octaédrica de las nanopartículas magnéticas aumenta su capacidad de calentamiento. Además, se ha podido desarrollar y optimizar una técnica de recubrimiento de nanopartículas magnéticas para mantenerlas estables en medio fisiológico.

En estos estudios (y en muchos otros más) se ha podido observar que el régimen de saturación de las nanopartículas magnéticas está generalmente fuera de los límites experimentales, de campo magnético y frecuencia, de los magnetómetros CA actuales.

Esto proporciona una información incompleta de las propiedades magnéticas de las nanopartículas.

Con el fin de poder realizar estudios mas avanzados y completos del comportamiento de calentamiento de las nanopartículas magnéticas, en el Capítulo 4 se ha desarrollado un magnetómetro CA que es capaz de trabajar en un amplio rango de frecuencias (50 kHz- 1 MHz) y generar campos magnéticos mas altos que los existentes hasta ahora: 90 mT a 50 kHz y 30 mT a 1 MHz.

El campo magnético es generado con un solenoide, alimentado con un amplificador de potencia de 1 kW. El solenoide forma parte de un circuito resonante variable, que permite que el magnetómetro CA trabaje a distintas frecuencias. Las propiedades geométricas del solenoide que maximizan el campo magnético han sido optimizadas para poder generar campos altos.

Además, este magnetómetro incorpora una sistema de temperatura que permite medir los ciclos de histéresis CA y el SAR entre 220 y 380 K.

Por otra parte, se ha implementado una mecanismo de control automatizado para desplazar las bobinas captadoras (que miden la magnetización de las nanopartículas) dentro del solenoide. De esta manera, se minimiza la señal de campo inducida en las bobinas captadoras.

Asímismo, para medir la magnetización de una manera más precisa se ha añadido un mecanismo de desplazamiento de la muestra para situarla en cada una de las bobinas captadoras.

Todo el control de las instrumentos del magnetómetro CA y el tratamiento de los datos se realiza mediante un programa LabVIEW diseñado para tal fin.

Finalmente, en el capítulo 5 se ha estudiado la potencialidad del magnetómetro CA diseñado en el anterior capítulo.

Para ello se han medido los ciclos de histéresis CA y el SAR de nanopartículas de magnetita con tamaños comprendidos entre 16 y 29 nm. Las medidas se han realizado con intensidades de campo de hasta 90 mT y tres frecuencias distintas, a temperatura ambiente y en medio congelado.

El medio de dispersión de las nanopartículas magnéticas, se ha congelado mediante el sistema de temperatura incorporado al nuevo magnetómetro CA. La congelación del medio de dispersión permite desacoplar los efectos de rotación de las nanopartículas de los de relajación intrínseca de la magnetización. Esto resulta sumamente útil para poder estudiar la influencia de diferentes arreglos en el SAR.

Comparando los ciclos de histéresis CA en medios liquidos y congelados se ha podido observar que las nanopartículas de mayor tamaño tienden a orientarse con el campo magnético formando cadenas.

Además, se ha demostrados que el campo magnético generado por el magnetómetro CA es capaz de saturar las nanopartículas utilizadas para este estudio.

De esta manera, se ha confirmado que el SAR máximo depende en gran medida del tamaño de las partículas y de la distribución angular de los ejes de fácil magnetización.

La obtención de la saturación ha permitido validar experimentalmente, por primera vez, las teorías basadas en el modelo de Stoner-Wohlfarth (en ingles, Stoner-Wohlfarth Model Based Theories (SWMBT)), que permiten analizar la influencia del campo magnético en la magnetización de las nanopartículas monodominio con anisotropía uniaxial.

Este modelo resulta muy útil para poder calcular el valor de la anisotropía de las nanopartículas. Hasta el momento los ciclos CA y el SAR no saturado no permitían calcular la anisotropía de una manera precisa.

Por ultimo, cabe mencionar que el campo magnético podría producir efectos adversos en el paciente al aplicársele el tratamiento de hipertermia magnética.

Estos efectos se producirían cuando se sobrepasa un limite establecido que viene dado por el producto del campo magnético y la frecuencia.

Por ello, resulta de vital importancia calcular para cada muestra la intensidad y la frecuencia óptimas del campo magnético para maximizar el SAR y asegurar la seguridad del paciente.

Para poder realizar este estudio el magnetómetro CA necesita trabajar en un amplio rango de intensidad y frecuencia, como el desarrollado en esta tesis.

De esta manera, en este trabajo se han podido calcular por primera vez la intensidad y frecuencias óptimas para maximizar el SAR de partículas de distinto tamaño dentro de los límites de seguridad del paciente.

Estos tres bloques ofrecen una descripción detallada del diseño y potencial de un magnetómetro CA, tras realizar un exhaustivo estudio de las limitaciones de la instrumentación existente.

Este equipo permite realizar diferentes estudios del comportamiento de nanopartículas magnéticas, lo que da pie a colaborar con distintos grupos para desarrollar nanopartículas con alta capacidad de calentamiento.

Acknowledgments

Alguien, al principio de la tesis me dijo, que me pegara como una lapa a todas aquellas personas que me pudieran enseñar algo, y seguramente, fue uno de los mejores consejos que he recibido durante este tiempo.

Esta tesis va dedicada a todas aquellas personas que me han trasmitido su conocimiento, que han invertidos su tiempo en mí y que me han apoyo durante estos años. Siempre os voy a llevar en mi corazón.

En primer lugar, me gustaría agradecerles a mis directores, Fernando y José Ángel, por darme la oportunidad de incorporarme al grupo sin apenas conocerme. Habéis sido unos buenos padres científicos, exigentes pero respetuosos. Me habéis dado espacio y libertad para poder hacer mi propio camino, pero a su vez me habéis dado vuestra sabia opinión como investigadores experimentados. Mila esker bihotz bihotzetik.

Por otra parte, quisiera agradecer a Eneko Garaio, por ayudarme y apoyarme. Sin duda eres una de esas personas a las que me pegué como una lapa. Todavía recuerdo, los primeros meses en los que te seguía a todos los lados... ¡Qué paciencia tuviste conmigo! Somos personas muy distintas, pero nos hemos complementado a la perfección. Gracias por ensenarme tanto durante estos años.

Esta tesis no hubiera sido posible sin la ayuda de Iñaki Orue. He aprendido muchísimas cosas gracias a ti. Todavía puedo sentir los momentos de ilusión cuando por fin nos funcionaba algo en el laboratorio y también los de frustración cuando las cosas no salían como queríamos. Pero nada de esto es comparable a los momentos humanos que he vivido contigo, gracias por apoyarme y por tan buenos consejos. Siempre he pensado que cuando todo el mundo opina que alguien es buena persona, es porque esa persona es buena de verdad. Y tú, Iñaki, eres un claro ejemplo de ello. Necesitaría una tesis entera para agradecerte todo lo que has hecho por mi. Que afortunada soy de que hayas aparecido en mi camino. Gracias tato.

No quisiera perder esta oportunidad para darles las gracias a todos los miembros de mi grupo de investigación. En especial a Eneko Axpe, que aunque no compartimos mucho tiempo juntos, calaste en mi y dejaste una huella difícil de borrar. Gracias por tramitarme tus ganas de vivir y tu energía interminable. ¡Vuelve ya!

También quisiera darle las gracias a Javier Alonso Hamilton y a Jorge Feuchtwanger por estar siempre dispuestos a ayudar.

Gracias a la universidad, mi casa. Gracias también al BC Materials por darme el apoyo económico y al Gobierno Vasco por financiarme la tesis.

La ciencia me ha dado muchas cosas durante estos años, pero me quedo con las personas. Siempre, con las personas. Gracias a mis chicas del *Akelarre*: Maite, Lulu, Anabel, Catarina y Libe por tantos momentos vividos, por tantos consejos y tanto cariño. Gracias Maite por aparecer en mi vida, por enseñarme tantas cosas y por darme tan buenos consejos y amor infinito. Gracias a Lulu por ser como eres, simplemente genial y amorosa. Gracias a Anabel por ser siempre tan positiva y por ver el lado bueno de las cosas. Tener alguien como tu cerca siempre es un privilegio. Con vosotras he aprendido que las amistades de verdad pueden surgir en cualquier momento de la vida. También quisiera darles las gracias a Idoia y Oihane, que aunque aparecisteis al final de la tesis hemos vivido muchos momentos divertidos juntas. Gracias también a Popi, Edu, Oscar, Jorge, Nerea, Inari, los Javis, Borja, David G., Bea, Andoni, Mattin, Iraultza, Luca, Dani, Eugen, Ivan, Rosa, Ana Maria, Esti y todos los demás. Cada uno de vosotros me habéis enseñado algo. La universidad es conocimiento, y no solo científico, sino también filosófico, político y social. Nuestras tertulias me han enriquecido enormemente y he podido crecer como persona gracias a ellas.

Una de las cosas mas increíbles que me han pasado durante la tesis ha sido poder ir a congresos y cursos en el extranjero. ¡He podido conocer a gente maravillosa, de países que a veces, ni siquiera sabía que existían! Gracias a todos vosotros, en especial a mi amiga del alma Daniela, pequeña loca argentina...ven pronto a visitarme, te espero con los brazos abiertos.

Y por ultimo y más importante, gracias a mi familia, sois mi motor y me brújula. Siempre me habías ayudado a encontrar el norte, cuando lo había perdido. Gracias a mis tías, aitites, familia política. Gracias aita por haber existido en mi vida, te echo tanto de menos...Gracias a mi madre, por quererme incondicionalmente y por ser la mejor persona que conozco. Si pudiera alguna vez ser la mitad de buena que tú, yo ya me daba por satisfecha en la vida.

Finalmente, gracias a Ibai, mi compañero de viaje. Por apoyarme tanto y por valorarme simplemente por ser quien soy. Gracias por tu apoyo incondicional y por tus consejos. Gracias por tu amor y cariño. Eres la suerte de mi vida.

Seneca dijo que hace falta toda una vida para aprender a vivir. De igual manera, yo creo que hace falta toda una carrera científica para aprender a investigar. Pero por el momento, disfrutemos del viaje.

"Voici mon secret: seulement avec le cœur que l'on peut voir à juste titre Ce qui est essentiel est invisible pour les yeux."

Le Petit Prince - Antoine de Saint-Exupéry

A mi aita

Abbreviations

AC	Alternating current
AMF	Alternating Magnetic Field
FC	Field Cooled
FEM	Finite Element Method
FFT	Fast Fourier Transform
F-MNPs	Fixed moments magnetic nanoparticles
MH	Magnetic Hyperthermia
HT	Hyperthermia Therapy
LRT	Linear Response Theory
MNP	Magnetic Nanoparticle
MPI	Magnetic Particle Imaging
MRI	Magnetic Resonance Imaging
MTB	Magnetotactic Bacteria
NCI	National Cancer Institute
SAR	Specific Absorption Rate
SC	Section Constant
SP-MNP	Superparamagnetic nanoparticles
SQUID	Superconducting Quantum Interference Device
SWMBTs	Stoner-Wohlfarth Model Based Theories
PA	Power Amplifier
PBS	Phosphate-buffered saline
PID	Proportional Integral Derivative Controller
TEM	Transmission Electron Microscopy
TGA	Thermogravimetric Analysis
TSG	Tumor Suppressor Gene
VSM	Vibrating Sample Magnetometer
ZFC	Zero-Field Cooled

Contents

Chapter 1

Introduction

1.1 Cell biology of cancer

Cancer is, by its nature, an incredibly resilient, and thus, incredibly challenging, disease. Globally, it is estimated that 100 million people were diagnosed with cancer in 2017, and almost 9.6 million people died, making it the second leading cause of death in the world (only surpassed by cardiovascular diseases) [1]. Due to population growth and aging, the morbidity and mortality associated with cancer are rapidly increasing.

Cancers are defined by the National Cancer Institute (NCI) as a collection of diseases in which abnormal cells grow out of control and spread to nearby tissue. Growing in an uncontrollable manner and unable to recognize its own natural boundary, the cancer cells may spread to areas of the body where they do not belong to [2].

In a cancer cell, several genes mutate and the cell becomes defective. A gene is a segment of DNA that determines the structure of a protein, which is needed for development and growth as well as carrying out vital chemical functions in the body. Genes are arranged in pairs, each one from one biological parent.

Cancer is driven by two classes of genes: oncogenes and tumor suppressor genes (TSGs), each providing an essential function in normal cells. Oncogenes are derived from mutated versions of normal cellular genes (proto-oncogenes) that control cell proliferation, survival and motility. In normal cells, expression of proto-oncogenes is very carefully regulated to avoid uncontrolled cell growth. In cancer, activating mutations

of proto-oncogenes cause uncontrolled cell division, enhanced survival (even after anti-cancer treatment) and dissemination. Oncogenes are described as phenotypically dominant, so a single mutated copy of a proto-oncogene is sufficient to promote cancer.

On the other hand, TSGs are normal cellular genes that function to inhibit cell proliferation and survival. They are frequently involved in controlling cell cycle progression and programmed cell death (apoptosis). In contrast to oncogenes, TSGs are phenotypically recessive, so both copies of TGS genes must be functionally altered to promote cancer. Therefore, cancer can occur either when active oncogenes are expressed or when tumor suppressor genes are lost [3].

1.2 Cancer treatment

Cancer treatment involves medical procedures to destroy, modify, control, or remove primary or metastatic cancer tissue. The goals of cancer treatment include eradicating known tumors entirely and preventing the recurrence or spread of the primary cancer. At present, conventional approaches in use for cancer treatment include surgery, radiation therapy, chemotherapy, or a combination of them.

Surgery involves removing the obvious cancerous tissue and it is the primary treatment for most cancers, particularly solid tumors. It has served as the only curative therapy for most solid tumors at an early stage. However, a majority of cancer cases are diagnosed at locally advanced or even metastatic stages, limiting the applicability of curative surgery. Surgical techniques used for surgery include cryosurgery, electrocauterization surgery, laser surgery, gamma knife, and “en bloc” resection [4].

Radiotherapy is based on the use of ionizing radiation to destruct cancer cells. Tumor cells show an increased metabolism, higher rates of glycolysis and enhanced radiosensitivity as compared to normal cells, making them more vulnerable to radiation. The efficiency of radiotherapy relies on the irreversible damage that the ionizing radiation provokes to the DNA of cancer cells, which eventually kills them or avoids their reproductive cycle, controlling in this way the progress of the tumor. However, the therapeutic efficacy of radiotherapy alone for treating locally or regionally advanced cancer is often limited by tumour radio-resistance, systemic tumor progression, and local or distant metastases [5].

Finally, chemotherapy uses chemical agents (anti-cancer or cytotoxic drugs) to interact with cancer cells to eradicate or control the growth of cancer. In chemotherapy, drugs that interfere primarily with DNA synthesis and mitosis are used to destroy cancer cells. Different agents work through many different mechanisms: some damage a cell's genetic material; some prevent the cell from dividing. Since chemotherapeutic drugs cannot distinguish between normal cells and cancer cells, both types of cells are affected by chemotherapy causing unpleasant side effects [6].

The toxicity to surrounding healthy cells, drug resistance of cancers, ineffectiveness against metastatic disease, difficulty in overcoming the biological barriers, and tumor relapse have limited the efficacy of this common therapies. Therefore, the development of new advanced techniques to replace or partner conventional treatments is strongly demanded. Nowadays, various new techniques that exhibit reduced side effects, including photothermal therapy, gene therapy, immunotherapy, photodynamic therapy and hyperthermia therapy among others, have been developed in the laboratory and few of them are now under clinical investigation.

Hyperthermia therapy (HT) is an important novel treatment, which consists in damaging and destructing cancer cells increasing the temperature of the tumors between 41-46 °C. The term hyperthermia comes from the Greek words *hyper*, meaning raise and *therme*, meaning heat.

Historically, the clinical use of hyperthermia goes back to Egyptian times over 5000 years ago when an Egyptian medical papyrus recounts an attempt to treat breast cancer with a "heated stick" [7]. Many ancient cultures, including Roman, Chinese, Indian, and Japanese, have used this concept in curative and preventive medicine. Hippocrates, a Greek physician (479–377 BC) who is referred to as the "father of modern medicine", was aware of the potential of heat to cure or shrink tumors. He recognized hyperthermia as follows: "Those who cannot be cured by medicine can be cured by surgery. Those who cannot be cured by surgery can be cured by fire. Those who cannot be cured by fire, they are indeed incurable". Cancer treatment by hyperthermia was also cited in ancient Rome by Cornelius Celsus Aulus, a Roman doctor (25BC–50AD), who observed that the earliest stages of cancer are enormously thermosensitive. During the late 1800s initial publications on hyperthermia appeared in Bush [8] and Westermark [9]. Dr. William B. Coley (1862–1936) developed the Coley's toxin in the late 19^{th} century as a treatment

for cancer. The Coley's toxin is a mixture of fever inducing bacteria that was given to cancer patients. Until the Second World War hyperthermia was one of the most effective cancer treatment [10].

Cancer cells are not more sensitive to the increase of temperature than normal cell. It has been shown *in vitro* that cell viability following hyperthermia treatment is heavily influenced by both the temperature and the duration of hyperthermia. One of the possible mechanisms behind the reduction in cell viability is protein denaturation that is thought to affect several downstream pathways including inactivation of protein synthesis, cell cycle progression and DNA repair [11, 12]. Furthermore, hyperthermia can have an adverse impact on the cytoskeleton, organelles, intracellular transport, and RNA processing [13]. Another potential contributor to reduction in cell viability is heat-induced alterations in the plasma and subcellular organelle membranes, as well as membrane protein [14, 15]. On the other hand, the chaotic vasculature in solid tumors, resulting in regions with hypoxia and low pH, make them more sensitive to HT [16].

Despite the multitude of mechanisms by which hyperthermia can induce cell death, it is not efficient as a single agent treatment, mainly due to its poor specificity and the development of thermotolerance which may make subsequent hyperthermia treatments less effective. However, in combination with radiotherapy or chemotherapy, hyperthermia can lead to improved patient outcomes [16, 17].

There are several methods to increase the temperature of tumors in hyperthermia, including microwaves, ultrasound, radiofrequency, laser and magnetic nanoparticles (MNPs).

1.3 Magnetic hyperthermia therapy

Magnetic hyperthermia (MH) is a novel treatment that is induced diffusing MNPs systemically to target cancer tissues by means of antibodies and applying an alternating magnetic field (AMF) of frequencies ranging between 100 kHz and 1 MHz in the target area. Under such conditions, magnetic nanoparticles act as very local heat sources, which are capable of rising the temperature of cancer tissues and consequently destructing the tumor [18–24] (see Figure 1.1).

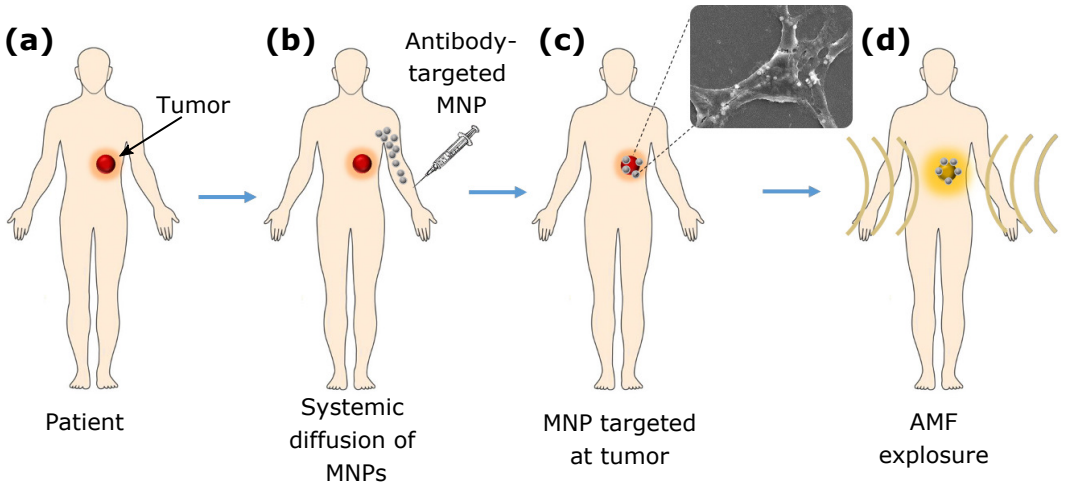

FIGURE 1.1: Sketch showing the general procedure for the magnetic hyperthermia treatment: (a) A patient is diagnosed with cancer, (b) antibody-targeted MNPs are injected systemically into the human body, (c) the magnetic nanoparticles are targeted at the tumor and (d) an alternating magnetic field is applied to induce the hyperthermia.

Magnetic hyperthermia can be dated back to 1957, where Gilchrist *et al.* selectively heated the tumors by exploiting magnetic particles in the presence of an AMF[25]. With the rise in nanotechnology, the introduction of MNPs has further evolved this approach into a well-researched field.

In 1993, Jordan *et al.*[24] showed that delivering magnetic nanoparticles via direct injection into the tumor could result in much more effective and selective heating of tumors when compared to other heating techniques such as radiofrequency heating and ultrasound. Since then, significant efforts have gone into the development of a clinical AMF system [26]. In 2012, MagForce company (Berlin, Germany) obtained the European Union Regulatory Approval to perform the Nanotherm® therapy to treat the glioblastoma multiforme at the Charité Hospital in Berlin. The Nanotherm® therapy is carried out using an AMF operating at a fixed frequency of 100 kHz and a variable field strength of 0 - 23 mT [27–29].

Magnetic hyperthermia is also being employed as supplementary therapy to chemotherapy or radiotherapy [16, 30]. Magnetic hyperthermia and these conventional therapies are synergistic because the conditions contributing to radio-resistance (hypoxia, acidification, etc.) generally enhance sensitivity to heat and chemosensitizing effects occur due to hyperthermia through several routes (intracellular drug accumulation, inhibition of DNA repair, enhanced free radical production, etc.) [17]. Additionally, MH can also be applied with Magnetic Particle Imaging (MPI) as it is explained below.

Magnetic nanoparticles delivered systemically accumulate in off-target organs such as liver and spleen, resulting in collateral heat damage to these organs when magnetic field is applied for the treatment [31]. Therefore, the control of the position of the magnetic nanoparticles is vital during magnetic hyperthermia therapy. MPI is a molecular imaging technique that directly detects and quantifies MNP by exploiting their dynamic magnetization in frequencies between 20 kHz and 50 kHz. MPI is an non-invasive 3D tomographic image method with high sensitivity and contrast (no tissue signal unlike Magnetic resonance imaging (MRI)) and excellent safety profile [32].

For minimizing the heat damage to the healthy tissues, image-guided treatments are being explored. Tay *et al.* [33] have developed a novel MPI-MH platform with quantitative MPI image guidance for treatment planning and localization of MH to selected regions (see Figure 1.2).

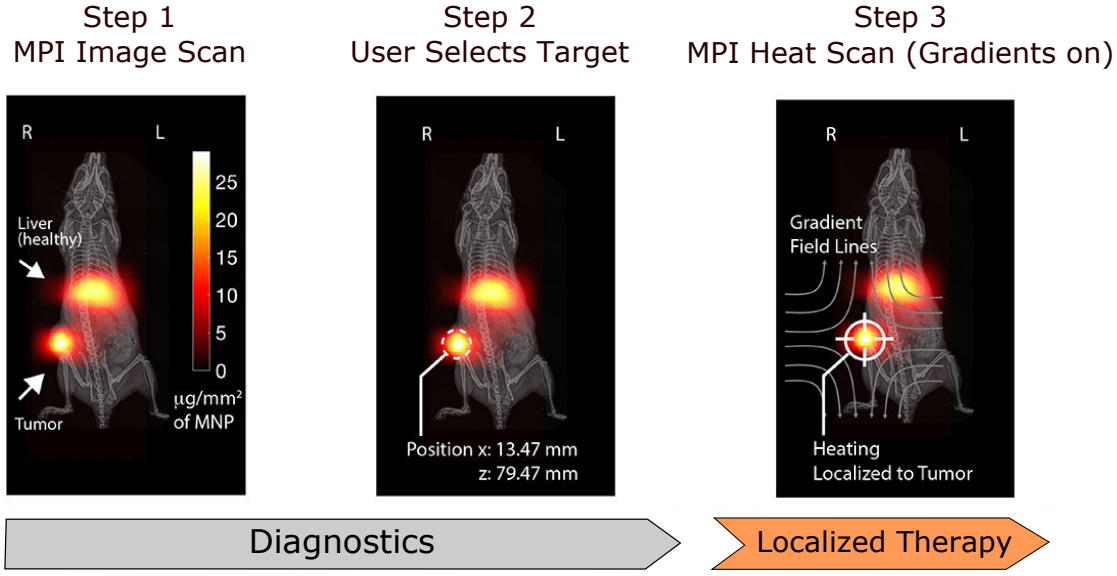

FIGURE 1.2: Step 1: MPI scan enables clear visualization with high contrast of the MNPs biodistribution in regions of pathology (tumor) and also in healthy clearance organs (liver). Step 2: User selects a region, in this case the tumor, to localize the MH. Step 3: MH is performed while the MPI gradients are on and held in the target position. Heating is experimentally localized centered at tumor while minimizing collateral heat damage to the liver. Figure taken from Tay *et al.*[33].

During MH treatment, eddy current effects generated by AMF produce a non-specific heating in the body that can affect negatively healthy tissues of potential human patients. The strength of these eddy currents depends on the product of the magnetic field intensity and frequency, $H \cdot f$, so different safety limits for the maximum acceptable $(H \cdot f)$ have been proposed. For several years, the so-called Atkinson-Brezovich criterion [34, 35], $(H \cdot f)$ fixed to 4.85×10^8 $\mathrm{Am^{-1}s^{-1}}$ was considered as the acceptable threshold

for the safe clinical use. However, experiments and analysis performed have shown that $H \cdot f$ should be much larger than the Atkinson-Brezovich limit. For instance, Hergt proposed a new limit of 5×10^9 $Am^{-1}s^{-1}$ [36] whereas Mamiya fix the new limit up to 18.7×10^9 $Am^{-1}s^{-1}$ [37]. There is still ongoing discussion of this matter, so further experiments are needed to set the truthful safety limit.

Bibliography

[1] M. Roser and H. Ritchie, "Cancer," *Our World in Data*, 2015.

[2] B. Alberts, A. Johnson, J. Lewis, M. Raff, K. Roberts, and P. Walter, "The Molecular Basis of Cancer-Cell Behavior," *Molecular Biology of the Cell. 4th edition*, 2002.

[3] P. Nenclares and K. J. Harrington, "The biology of cancer," *Medicine*, vol. 48, no. 2, pp. 67–72, 2020.

[4] C.-Y. Huang, D.-T. Ju, C.-F. Chang, P. M. Reddy, and B. K. Velmurugan, "A review on the effects of current chemotherapy drugs and natural agents in treating non–small cell lung cancer," *BioMedicine*, vol. 7, no. 4, p. 23, 2017.

[5] M. Bañobre-López, A. Teijeiro, and J. Rivas, "Magnetic nanoparticle-based hyperthermia for cancer treatment," *Reports of Practical Oncology & Radiotherapy*, vol. 18, no. 6, pp. 397–400, 2013.

[6] V. Schirrmacher, "From chemotherapy to biological therapy: A review of novel concepts to reduce the side effects of systemic cancer treatment (Review)," *International Journal of Oncology*, vol. 54, no. 2, pp. 407–419, 2018.

[7] "The Edwin Smith Surgical Papyrus, Volume 1: Hieroglyphic Transliteration, Translation, and Commentary | The Oriental Institute of the University of Chicago."

[8] W. Bush, "Uber den Finfluss wetchen heftigere Eryspelen zuweilen auf organlsierte Neubildungen dusuben.," *Verh Natruch Preuss Rhein Westphal*, no. 23, pp. 28–30, 1886.

[9] F. Westermark, "Uber die Behandlung des ulcerirenden Cervix carcinoma mittels Knonstanter Warme," *Zentralbl Gynkol*, pp. 1335–1339, 1898.

[10] R. W. Y. Habash, "Chapter 53 - Therapeutic hyperthermia," in *Handbook of Clinical Neurology* (A. A. Romanovsky, ed.), vol. 157 of *Thermoregulation: From Basic Neuroscience to Clinical Neurology, Part II*, pp. 853–868, 2018.

[11] W. C. Dewey, L. E. Hopwood, S. A. Sapareto, and L. E. Gerweck, "Cellular Responses to Combinations of Hyperthermia and Radiation," *Radiology*, vol. 123, no. 2, pp. 463–474, 1977.

[12] L. Roizin-Towle and J. P. Pirro, "The response of human and rodent cells to hyperthermia," *International Journal of Radiation Oncology*Biology*Physics*, vol. 20, no. 4, pp. 751–756, 1991.

[13] K. Richter, M. Haslbeck, and J. Buchner, "The Heat Shock Response: Life on the Verge of Death," *Molecular Cell*, vol. 40, no. 2, pp. 253–266, 2010.

[14] P. d. A. Mello, S. Bian, L. E. B. Savio, H. Zhang, J. Zhang, W. Junger, M. R. Wink, G. Lenz, A. Buffon, Y. Wu, and S. C. Robson, "Hyperthermia and associated changes in membrane fluidity potentiate P2X7 activation to promote tumor cell death," *Oncotarget*, vol. 8, no. 40, pp. 67254–67268, 2017.

[15] D. Chang, M. Lim, J. A. C. M. Goos, R. Qiao, Y. Y. Ng, F. M. Mansfeld, M. Jackson, T. P. Davis, and M. Kavallaris, "Biologically Targeted Magnetic Hyperthermia: Potential and Limitations," *Frontiers in Pharmacology*, vol. 9, 2018.

[16] J. v. d. Zee, D. González, G. C. v. Rhoon, J. D. v. Dijk, W. L. v. Putten, and A. A. Hart, "Comparison of radiotherapy alone with radiotherapy plus hyperthermia in locally advanced pelvic tumours: a prospective, randomised, multicentre trial," *The Lancet*, vol. 355, no. 9210, pp. 1119–1125, 2000.

[17] M. Hurwitz and P. Stauffer, "Hyperthermia, Radiation and Chemotherapy: The Role of Heat in Multidisciplinary Cancer Care," *Seminars in Oncology*, vol. 41, no. 6, pp. 714–729, 2014.

[18] Q. A. Pankhurst, J. Connolly, S. K. Jones, and J. Dobson, "Applications of magnetic nanoparticles in biomedicine," *Journal of Physics D: Applied Physics*, vol. 36, no. 13, pp. R167–R181, 2003.

[19] A. Jordan, P. Wust, R. Scholz, H. Faehling, J. Krause, and R. Felix, "Magnetic Fluid Hyperthermia (MFH)," in *Scientific and Clinical Applications of Magnetic Carriers* (U. Häfeli, W. Schütt, J. Teller, and M. Zborowski, eds.), pp. 569–595, Boston, MA: Springer US, 1997.

[20] A. Jordan, R. Scholz, P. Wust, H. Fähling, and Roland Felix, "Magnetic fluid hyperthermia (MFH): Cancer treatment with AC magnetic field induced excitation of biocompatible superparamagnetic nanoparticles," *Journal of Magnetism and Magnetic Materials*, vol. 201, no. 1, pp. 413–419, 1999.

[21] S. Mornet, S. Vasseur, F. Grasset, and E. Duguet, "Magnetic nanoparticle design for medical diagnosis and therapy," *Journal of Materials Chemistry*, vol. 14, no. 14, pp. 2161–2175, 2004.

[22] S. Dutz and R. Hergt, "Magnetic particle hyperthermia—a promising tumour therapy?," *Nanotechnology*, vol. 25, no. 45, p. 452001, 2014.

[23] E. A. Périgo, G. Hemery, O. Sandre, D. Ortega, E. Garaio, F. Plazaola, and F. J. Teran, "Fundamentals and advances in magnetic hyperthermia," *Applied Physics Reviews*, vol. 2, no. 4, p. 041302, 2015.

[24] A. Jordan, P. Wust, H. Fählin, W. John, A. Hinz, and R. Felix, "Inductive heating of ferrimagnetic particles and magnetic fluids: Physical evaluation of their potential for hyperthermia," *International Journal of Hyperthermia*, vol. 9, no. 1, pp. 51–68, 1993.

[25] R. K. Gilchrist, R. Medal, W. D. Shorey, R. C. Hanselman, J. C. Parrott, and C. B. Taylor, "Selective Inductive Heating of Lymph Nodes," *Annals of Surgery*, vol. 146, no. 4, pp. 596–606, 1957.

[26] X. Liu, Y. Zhang, Y. Wang, W. Zhu, G. Li, X. Ma, Y. Zhang, S. Chen, S. Tiwari, K. Shi, S. Zhang, H. M. Fan, Y. X. Zhao, and X.-J. Liang, "Comprehensive understanding of magnetic hyperthermia for improving antitumor therapeutic efficacy," *Theranostics*, vol. 10, no. 8, pp. 3793–3815, 2020.

[27] A. Jordan, R. Scholz, K. Maier-Hauff, M. Johannsen, P. Wust, J. Nadobny, H. Schirra, H. Schmidt, S. Deger, S. Loening, W. Lanksch, and R. Felix, "Presentation of a new magnetic field therapy system for the treatment of human solid tumors with magnetic fluid hyperthermia," *Journal of Magnetism and Magnetic Materials*, vol. 225, no. 1, pp. 118–126, 2001.

[28] B. Thiesen and A. Jordan, "Clinical applications of magnetic nanoparticles for hyperthermia," *International Journal of Hyperthermia*, vol. 24, no. 6, pp. 467–474, 2008.

[29] U. Gneveckow, A. Jordan, R. Scholz, V. Brüss, N. Waldöfner, J. Ricke, A. Feussner, B. Hildebrandt, B. Rau, and P. Wust, "Description and characterization of the novel hyperthermia- and thermoablation-system MFH 300F for clinical magnetic fluid hyperthermia," *Medical Physics*, vol. 31, no. 6, pp. 1444–1451, 2004.

[30] D. T. Ohguri, H. Imada, H. Narisada, K. Yahara, T. Morioka, K. Nakano, Y. Miyaguni, and Y. Korogi, "Systemic chemotherapy using paclitaxel and carboplatin plus regional hyperthermia and hyperbaric oxygen treatment for non-small cell lung cancer with multiple pulmonary metastases: Preliminary results," *International Journal of Hyperthermia*, vol. 25, no. 2, pp. 160–167, 2009.

[31] C. Kut, Y. Zhang, M. Hedayati, H. Zhou, C. Cornejo, D. Bordelon, J. Mihalic, M. Wabler, E. Burghardt, C. Gruettner, A. Geyh, C. Brayton, T. L. Deweese, and R. Ivkov, "Preliminary study of injury from heating systemically delivered, nontargeted dextran–superparamagnetic iron oxide nanoparticles in mice," *Nanomedicine*, vol. 7, no. 11, pp. 1697–1711, 2012.

[32] B. Gleich and J. Weizenecker, "Tomographic imaging using the nonlinear response of magnetic particles," *Nature*, vol. 435, no. 7046, pp. 1214–1217, 2005.

[33] Z. W. Tay, P. Chandrasekharan, A. Chiu-Lam, D. W. Hensley, R. Dhavalikar, X. Y. Zhou, E. Y. Yu, P. W. Goodwill, B. Zheng, C. Rinaldi, and S. M. Conolly, "Magnetic Particle Imaging-Guided Heating *in Vivo* Using Gradient Fields for Arbitrary Localization of Magnetic Hyperthermia Therapy," *ACS Nano*, vol. 12, no. 4, pp. 3699–3713, 2018.

[34] W. J. Atkinson, I. A. Brezovich, and D. P. Chakraborty, "Usable Frequencies in Hyperthermia with Thermal Seeds," *IEEE Transactions on Biomedical Engineering*, vol. BME-31, no. 1, pp. 70–75, 1984.

[35] I. Brezovich, "Low frequency hyperthermia: capacitive and ferromagnetic thermoseed methods," *Medical physics monograph*, vol. 16, pp. 82–111, 1988.

[36] R. Hergt, S. Dutz, R. Müller, and M. Zeisberger, "Magnetic particle hyperthermia: nanoparticle magnetism and materials development for cancer therapy," *Journal of Physics: Condensed Matter*, vol. 18, no. 38, pp. S2919–S2934, 2006.

[37] H. Mamiya, Y. Takeda, T. Naka, N. Kawazoe, G. Chen, and B. Jeyadevan, "Practical Solution for Effective Whole-Body Magnetic Fluid Hyperthermia Treatment," 2017.

Chapter 2

Magnetic nanoparticles and metrology tools

2.1 Magnetic nanoparticles

The potential of MNPs as magnetic hyperthermia agents arises from their unique size-dependent physical, chemical and biological properties. The major benefit of the small size of magnetic nanoparticles, from a biological point of view, is that they are capable of interacting with living cells and organisms. Figure 2.1 shows a size scale for different nanoparticles ranging from 1 to 100 nm. As it can be appreciated the MNPs have a size comparable to proteins, DNA and viruses. Therefore, they are able to move across the blood stream, and even cross the blood barrier, that allow them to penetrate and distribute more homogeneously inside the tumor, provoking a heat diffusion that would kill a bigger number of neighboring tumor cells [1].

Iron oxide magnetic nanoparticles, like magnetite (Fe_3O_4) and maghemite (γ-Fe_2O_3), are considered to be one of the best candidates for biomedical applications due to their biocompatibility, accessibility, facile synthesis and magnetic behavior [3]. Currently Mn, Ni, Co or Zn doped iron oxides MNPs are also being explored as new magnetic hyperthermia agents [4, 5].

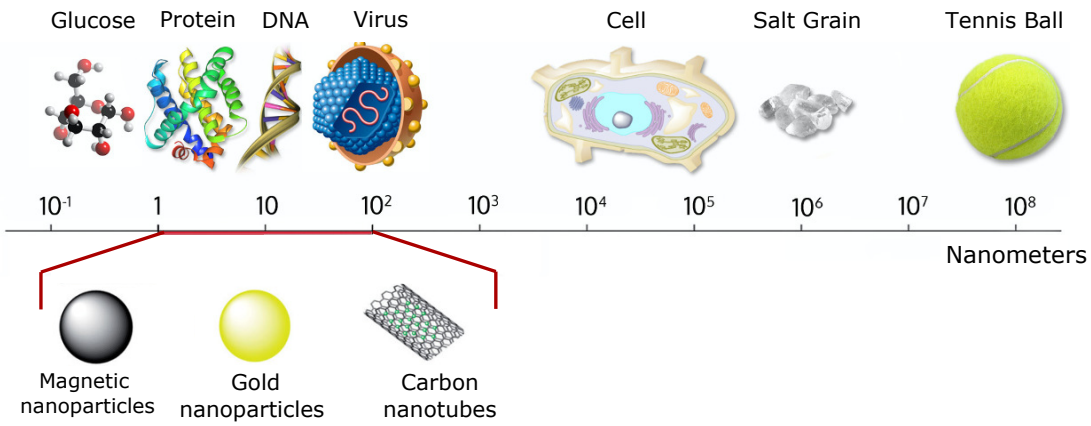

FIGURE 2.1: Size scale for different nanoparticles (bottom) as compared to other materials (top). The comparable size of nanoparticles to some biological entities, like virus, DNA and proteins, makes them ideal candidates for biomedical applications. Figure modified from Hulkoti *et al.*[2].

2.1.1 Synthesis methods

The synthesis method of the nanomaterials represents one of the most important challenges that determines the shape, size distribution, particle size, surface chemistry of the particles, and consequently their magnetic properties. In the last decades, three main synthesizes routes have been developed: chemical, physical, and biological.

Chemical methods, especially co-precipitation and thermal decomposition, are the most widely used routes to synthesize iron oxide magnetic nanoparticles due to their simple procedure and capabilities to more effectively control the size, shape, and composition of the nanoparticles [5].

Coprecipitation method is a classical and perhaps the simplest approach for synthesizing iron oxide nanoparticles. Basically, this process involves the precipitation of Fe^{2+} and Fe^{3+} salt aqueous solutions by addition of a base (e.g., NaOH). The size, morphology, and composition of the as-prepared nanoparticles can be controlled by a series of experimental parameters, like the precursors type, precursors ratio, the reaction temperature, and the pH [6]. One of the main advantages of this method is that it can directly obtain water-soluble nanoparticles with high yields in a simple process. Nevertheless, a few challenges still limit this method such as the control of the particle size and crystallinity [7].

Thermal decomposition methods involve the thermolysis of organometallic complex precursors (e.g., $Fe(acac)_3$ and $Co(acac)_3$) in boiling organic solvents in the presence

of surfactants (e.g., oleic acid and oleylamine) to synthesize nanoparticles of various materials. To control the size and morphology of the resulting nanoparticles, the concentrations of precursors and surfactants, the solvent and the experimental parameters like heating rate, heating temperature, and heating time are usually regulated. One of the main advantages of the thermal decomposition methods is that magnetic nanomaterials with high crystallinity, controllable morphology, and narrow size distribution in a high yield can be synthesized. However, the magnetic nanomaterials prepared by this method are usually coated with hydrophobic surfactants to prevent the particles from aggregation and rapid oxidation. This makes them water insoluble and therefore, a further surface modification step is required to render these nanoparticles water-soluble for biomedical applications [8].

Physical methods that combine lithography with a materials deposition technique (e.g., sputtering or thermal evaporation) allow to synthesize nanoparticles with well-determined particles' size, morphology and composition [9]. However, they usually are high cost techniques with high amount of waste and difficult size and shape tunability.

Finally, biological methods use various microorganisms such as bacteria [10], fungi [11], plant extracts [12] and waste materials [13] to synthesize different magnetic nanoparticles. This approach has advantages over other chemical and physical methods as this is greener, energy saving and cost effective [14]. The biological methods lead to the designing of magnetic nanoparticles with interesting morphologies and varied sizes. Additionally, the coating of biological molecules on the surface makes them biocompatible in comparison with the magnetic nanoparticles prepared by chemical methods. As example, magnetotactic bacteria (MTB) are aquatic microorganisms that internally biomineralize chain of magnetic nanoparticles, called magnetosomes, that use as a compass to reorient the whole bacteria along external magnetic field lines. Among all the MTB species, *Magnetospirillum gryphiswaldense* strain MSR-1 is frequently used as a model strain of MTB due to its ease of cultivation in the laboratory [15, 16].

The magnetosome chains synthesized by MSR-1 bacteria present an helical shaped structure and contain a variable number of $\sim$ 40–45 nm sized cuboctahedral magnetite magnetosomes (see Figure 2.2)

FIGURE 2.2: Transmission electron microscopy (TEM) image of *Magnetospirillum gryphiswaldense* showing the chain of magnetosomes inside the bacteria. The magnetosomes have cuboctahedral morphology and size of about 40-45 nm.

2.1.2 Surface modification

The colloidal stability of the MNPs under physiological conditions is an important issue, which needs to be addressed to use MNPs for any biomedical application. As mentioned before, the synthesis of monodisperse and highly crystalline nanoparticles requires non-hydrolytic synthetic routes and the use of hydrophobic surfactants that efficiently cover the particle surface. Therefore, as-synthesized hydrophobic nanoparticles are insoluble in water, and a direct application of these unmodified particles into aqueous solutions would inevitably lead to particle aggregation and precipitation [17].

To convert the hydrophobic magnetic nanoparticles into water stable colloidal, MNPs are coated with amphiphilic polymer, such as, poly(maleic anhydride-*alt*-1-octadecene) (PMAO). This coating provides a surface with uniformly distributed carboxyl groups and causes electrostatic repulsion between MNPs in water, counteracting the magnetic dipolar interactions [18].

However, when PMAO covered MNPs are placed in physiological media the salt ions screen the surface charges provoking instantaneous aggregations. Furthermore, MNPs-PMAO are prone to opsonization, a defense process initiated by the innate immune system, in which certain serum proteins attach to the particle surface and initiate

phagocytosis. One way to achieve an enchantment stability in physiological media and to prevent opsonization is to modify the surface of MNPs with an amphiphilic copolymer that contains long poly(ethylene glycol) (PEG) tails, such as PMAO-grafted PEG copolymers [19, 20].

The addition of targeting ligands into the surface of the magnetic nanoparticles increase selective cellular binding and internalization by receptor mediated endocytosis. These receptors are molecular structures or antigens that are overexpressed at the tumor site. Without the incorporation of targeting ligands, nanoparticles rely on non-specific interactions with cell membranes, which can be low when magnetic nanoparticles are covered only by PEG polymers, decreasing the efficiency of the treatment. Therefore, targeting increases the uptake of nanoparticles and their cargo into the tumor cells. A variety of different molecules have been used for biofunctionalization of nanoparticles by active targeting including antibodies, affibodies, peptides, aptamers and carbohydrates [21].

2.2 Magnetism of magnetic nanoparticles

Magnetic nanoparticles are composed of materials that show ferromagnetic properties in bulk scale. However, at nanometric scale special magnetic properties are originated by the reduced dimensionality of the materials.

In ferromagnetic materials, multiple magnetic domains exist as a result of the balance between the exchange interaction energy that favors the parallel alignment of neighboring atomic moments and the magnetostatic interaction energy that tries to break them into smaller domains, orientated antiparallel to each other.

With decreasing the size of the ferromagnetic material, there is a critical value, D_c, below which the magnetostatic energy no longer allows for the breaking of the system into smaller domains, and so, the system is composed of single domains [22, 23] (see Figure 2.3 (a)).

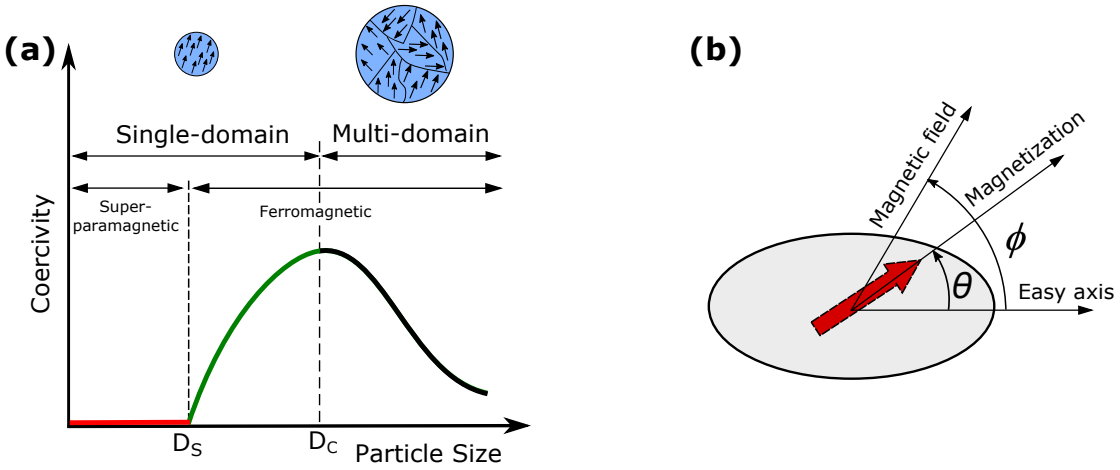

FIGURE 2.3: (a) Relationship between coercive field, H_c, and magnetic particle size. When the size of the particles decreases below a critical value, D_c, the domain wall disappears, and so, the particles are composed of single domains. When the particle size is further decreased, D_s, thermal energy overcomes magnetic anisotropy energy and, as a result, the particle switches from ferromagnetic to superparamagnetic regime. Figure adapted from [24]. (b) Angle distribution showing the direction of magnetization, magnetic field, and easy axis of a single domain MNPs with unixial anisotropy. The red arrow presents the magnetization of the particle, θ the angle between the magnetization and the easy axis and ϕ the angles between magnetic field and the easy axis. Figure adapted from [25].

The magnetic moments of single domain MNPs are parallel to each other. Assuming the coherent rotation of the magnetic moments the particle can be characterized by its total magnetic moment:

$$\mu = M_s V \tag{2.1}$$

where M_s is the saturation magnetization and V the particle volume. In general, μ is pinned along well defined direction, that is, along magnetic anisotropy axis. Magnetic anisotropy of the MNPs depends on several contributions, such as, surface, shape, magnetocrystalline and dipolar interactions [26]. These contributions have neither the same symmetry (cubic versus uniaxial) nor the same direction. The effective magnetic anisotropy results from the superposition of different effects. However, one of these contributions dominates and determines the first order contribution.

Spherical magnetite nanoparticles, that are generally used as magnetic hyperthermia agents, present a cubic magnetocrystalline anisotropy [27]. However, in real cases perfectly spherical particles are hard to synthesize and shape anisotropy should also

be considered. Due to the comparatively small magnetocrystalline anisotropy of magnetite, small deviations from the spherical shape renders an effective magnetic anisotropy of uniaxial or quasi-uniaxial sort rather than cubic anisotropy [28, 29].

When an external magnetic field is applied over ferromagnetic single domain nanoparticles with uniaxial magnetic anisotropy, it tries to align their magnetic moments along its direction. The orientation of the magnetic moment is then governed by the competition among anisotropy energy (uniaxial and non-interacting in the present case) and Zeeman energies, E_A and E_Z , respectively [25, 30]:

$$E = E_A + E_Z = K_{eff} V \sin^2\theta - \mu_0 M_s V H_{max} \cos(\theta - \phi) \tag{2.2}$$

where θ is the angle between easy axis and the magnetization, K_{eff} the effective uniaxial anisotropy, H_{max} the external magnetic field and ϕ the angle between the easy axis and the magnetic field (see Figure 2.3 (b)).

The influence of the external field in the orientation of the magnetization of a ferromagnetic single domain MNP assembly can be described by the Stoner-Wohlfarth model [30] (see Appendix B). By ignoring thermal effects, the problem is solved from minimal energy arguments. This model predicts an open hysteresis loop for ferromagnetic single domain MNP (see Figure 2.4 (a)).

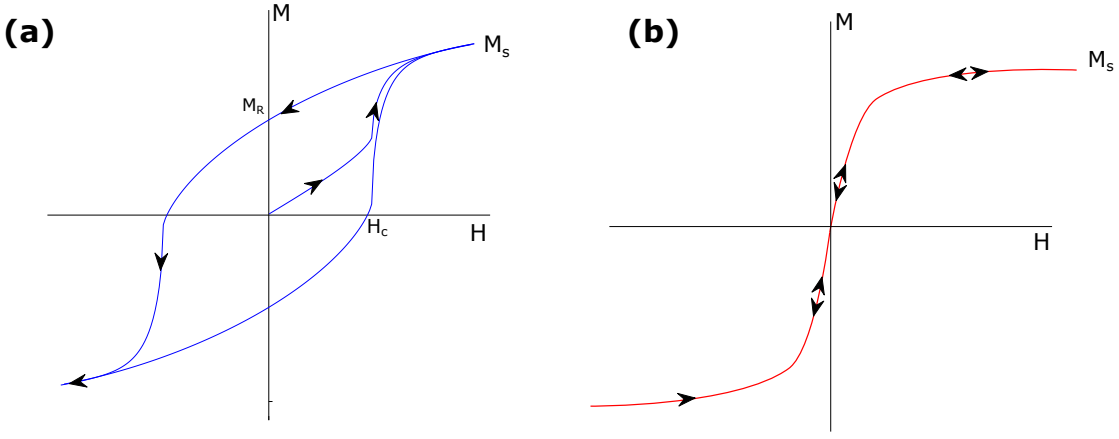

FIGURE 2.4: (a) Hysteresis loop of non-interacting, randomly oriented, uniaxial single domain MNPs and (b) Magnetization curve, *M(H)*, of superparamagnetic MNPs. M_s is the saturation magnetization, H_c is the coercive field and M_R the remanence magnetization.

However, thermal effects play an important role in the magnetic behavior of single domain MNPs. As the size of the particle decreases, there is a critical value, D_s (see Figure 2.3 (a)), below which the thermal energy, k_BT, is much larger than the anisotropy energy, $K_{eff}V$, and so, the magnetic anisotropy plays a negligible influence on the orientation of the magnetic moments of the particles, which fluctuate freely with temperature. This thermal equilibrium regime is called single domain superparamagnetic state. In this state, the orientation of the magnetization corresponds to a probability distribution rather than to a discrete set of values and the averaged magnetization follows approximately the Langevin curve (see Equation 2.3), with null coercive field and zero magnetization in the absence of an external magnetic field (see Figure 2.4 (b))[24].

$$M = M_s \left[\coth\left(\frac{\mu_0 H}{k_B T}\right) - \frac{k_B T}{\mu_0 H} \right] \tag{2.3}$$

The limit between single domain ferromagnetic and superparamagnetic state is determined by the time, called relaxation time, that the magnetization needs to reach the thermal equilibrium. Thermal activation of the magnetization over the anisotropy barrier is given by the Néel relaxation mechanism that is characterized by the Néel relaxation time, τ_N [31]:

$$\tau_N = \tau_0 \exp\left(\frac{K_{eff}V}{k_B T}\right) \tag{2.4}$$

where τ_0 is the attempt time, whose values are in the range 10^{-11} – 10^{-9} s.

However, in stable MNPs colloids there is a second relaxation mechanism called Brown relaxation, which is caused by the rotation of the particle inside the fluid. Brown mechanism is characterized by the Brown relaxation time, τ_B [32]:

$$\tau_B = \frac{3\eta V_H}{k_B T} \tag{2.5}$$

where η is the viscosity coefficient of the medium and V_H the hydrodynamic volume of the MNPs. Because Brownian and Néel processes take place in parallel, the resulting relaxation time τ is given by the Equation 2.6:

$$\tau = \frac{\tau_N + \tau_B}{\tau_N \cdot \tau_B} \tag{2.6}$$

The relaxation time is an important parameter that characterizes the dynamic magnetization of the MNPs. When the measurement time, τ_m, is much larger than the relaxation time of the system, the magnetization will have enough time to follow the applied magnetic field changes and it will be described by the Langevin curve, that is, a null loop with null coercive field. On the contrary, when the measurement time is shorter than the relaxation time, the magnetization will not be able to fully follow the applied magnetic field changes, resulting in an open hysteresis loop.

As mentioned before, for a given temperature, T, there is a particle size, D_s, below which the single domain particle switches from ferromagnetic to superparamagnetic behavior. On the other hand, for a certain particle size, there is a critical temperature, called blocking temperature, T_B, above which nanoparticles have a transition from ferromagnetic to superparamagnetic regime.

2.3 Specific Absorption Rate (*SAR*)

The indispensable initial step for designing a successful hyperthermia therapy is to determine the specific absorption rate (SAR) of the MNPs. This parameter is defined as the absorbed energy per unit of nanoparticle mass under an AMF.

SAR greatly depends on the physicochemical properties of the nanoparticles such as composition, size, shape, crystallinity, saturation magnetization, etc. [33, 34]. Additionally, interparticle magnetic interactions also affect the heating performance of MNPs [35], generally, decreasing the heating efficiency. However, some arrangements formed by dipolar magnetic interactions, like chainlike structures, have shown to possess high heat performance due to their ability to mechanically orient along the field lines [36]. The particles' mechanical alignment with the magnetic field is usually highly suppressed within biological environments, so the MNPs dispersion media also plays an important role in the heating performance. It is essential to count for MNP system with optimal SAR values, but even more fundamental is to gain knowledge about what characteristics of the system are really significant in order to score the optimal values.

There are two different methods to evaluate the SAR: calorimetry and AC magnetometry. Calorimetry method is the most widely used approach to determine the SAR. This technique consists on measuring the increase of temperature of the MNPs

under an AMF [37–39]. The experimental value is then calculated from the thermal model describing the system. If the process is adiabatic and no physical or chemical changes occur in the sample, except heating, then the SAR can be explicitly related to the measured heating by Equation 2.7:

$$SAR = \frac{C_{p,s}}{m_{MNP}} \frac{\Delta T}{\Delta t} \tag{2.7}$$

where T is the measured temperature, t is the time elapsed, $C_{p,s}$ is the heat capacity of the sample (i.e. nanoparticles and suspending medium), and m_{MNP} is the mass of the MNPs.

The adiabatic condition criterion is fundamental to calculate the SAR value using Equation 2.7. However, systems that work in adiabatic conditions are technologically complex and at the present only one adiabatic magneto-thermal set-up is reported in literature [40].

Consequently, almost all reported works on magnetic hyperthermia are performed on non-adiabatic apparatus. The heat losses produced by these set-ups cause the heating trend to downward as temperature increases. Therefore, heat losses have to be considered when calculating SAR from thermal models. However, choosing a thermal model that correctly fits each particular experimental system can be difficult, since it includes many thermal parameters of both, the samples and its environment, which varies with time and space [41, 42]. Thus, calculating SAR accurately using non-adiabatic system can be challenging.

On the other hand, AC magnetometry method is based on the measurement of dynamic magnetization, $M(t)$, of MNPs when they are excited by an AMF, $H(t)$. In this approach, the SAR can be calculated directly from the AC hysteresis loop's area (A), as it can be observed in Equation 2.8:

$$SAR\left(Wg^{-1}\right) = \frac{f}{c}A = \frac{f}{c}\mu_0 \oint M dH \tag{2.8}$$

where f is the frequency of the AMF and c is the sample concentration (MNPs mass per sample volume).

AC magnetometry arises as a robust, reproducible, fast and reliable method. In general, calorimetry and AC magnetometry are highly complementary techniques [43, 44]. Moreover, AC magnetometry provides additional and very valuable magnetic information that is not directly accessible by calorimetry alone. The complete determination of the AC hysteresis loop contains much more information than simply the SAR value.

For instance, collective phenomena of MNPs, related to the type of assembling, disordered or forming well-defined structures, are easily detected from the AC hysteresis loop [36, 37, 45–47]. AC magnetometry also has allowed to correlate the shape of the MNPs and their hyperthermia performance [48], or to clarify why the heating power of MNPs tends to fall in cellular environments [49].

2.4 Magnetometry tools

In order to explore the potential of magnetic nanoparticles the magnetic properties have to be measured at magnetic field intensities and frequencies relevant for their application. In recent years, several home-made AC magnetometers, have been developed in order to measure the magnetic response of magnetic nanoparticles. As it can be observed in Table 2.1, the first reported three AC magnetometers [50–52] works in frequencies lower than 100 kHz (frequency employed in Nanotherm® therapy) which limits the analysis of the heating behavior of the MNPs for a clinical hyperthermia application. In 2012, Gudoshnikov *et al.* [53] reported the first AC magnetometer that works above 100 kHz, however, its working range above this frequency is narrow (100-200 kHz) and the magnetic field intensity is low (20 mT) at these frequencies. In 2013, Bekovic *et al.* [54] developed an AC magnetometer that works in a wide frequency range of 100-600 kHz, but, with a very low magnetic field intensity (18-7 mT). It is also worth highlighting the set-up that Garaio *et al.* developed at the University of the Basque Country (UPV/EHU) in 2015 [43]. This device was the first AC magnetometer in the world that works in a wide magnetic hyperthermia frequency range of 149–1030 kHz with magnetic field intensities: up to 46 mT at lower frequency limit and up to 28 mT at upper frequency limit. Recently, in 2018, Lenox *et al.* built a AC magnetometer that works at high magnetic field intensities (160 mT), however, the working frequency is

fixed at 45 kHz, that makes it more appropriated to characterized MNPs for MPI than for MH.

Device	**Magnetic filed**	
Ref	Frequency (kHz)	Intensity (mT)
Veverka *et al.* [50]	50	35
Kobayashi *et al.* [51]	50	30
Mehdaoui *et al.* [52]	56	23
Gudoshnikov *et al.* [53]	[10-200]	[60-20]
Bekovic *et al.* [54]	[100-600]	[18-7]
Gudoshnikov *et al.* [55]	80	40
Veverka *et al.* [56]	100	18
Connord *et al.* [57]	[7-95]	[80-46]
Garaio *et al.* [43]	[149-1000]	[46-28]
Cabrera *et al.* [49]	[25-100]	[37-30]
Avugadda *et al.* [58]	[30-200]	30
Lenox *et al.* [59]	45	160

TABLE 2.1: AC magnetometers developed until 2020 with their maximum attainable magnetic field intensity for each working frequency.

2.4.1 AC magnetometers architecture

Despite differing approaches toward dynamic magnetization measurements, most AC magnetometers' hardware architecture designs and implementations are remarkably similar. As it is shown in Figure 2.5, an AC magnetometer consists on an *AMF generator* that produces a sinusoidal time-varying homogeneous and intense magnetic field and a *dynamic magnetization detector system* to record the magnetic response of the MNPs when they are exposed to the AMF.

2.4.1.1 Alternating magnetic field generator

Different strategies can be followed to create a homogeneous and intense AMF. The most widely used way to generate an AMF over a limited volume is to produce an AC current across a solenoid air coil.

A simple air coil can be electrically modeled with an inductance, L, in series with a resistor, R_L, and in parallel with a capacitor, C_L. The resistor arises from the resistive

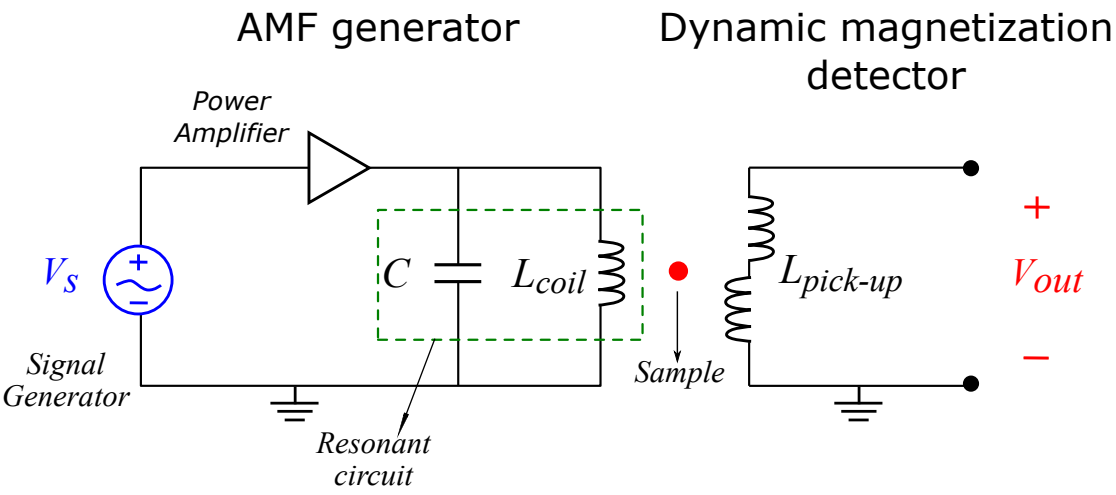

FIGURE 2.5: Electrical scheme of a conventional AC magnetometer. The device consists on an AMF generator and a dynamic magnetization measurements system. The AMF is created using a main coil that is part of a resonant circuit and the dynamic magnetization is measured with an oppositely wounded pick-up coil system. The AC current to excite the main coil is produced by a signal generator and amplified by a power amplifier (PA).

losses of the inductance and the capacitor from the electrical coupling between the windings of the coil (see Figure 2.6). The self-resonance frequency, f_r, of the main coil is given in the Equation 2.9:

$$f_r = \frac{1}{2\pi\sqrt{C_L L}} \tag{2.9}$$

If the working frequency of the magnetic field, f, is below the self-resonance frequency of the air coil the capacitance C_L can be neglected.

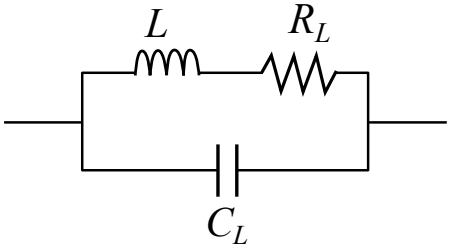

FIGURE 2.6: Equivalent electrical circuit of an air coil. The resistor, R_L, arise from the resistive losses of the coil and the capacitor, C_L, caused by the electrical coupling between the windings of the coil.

When using AC currents, the resistance R_L becomes critically enhanced at high frequencies by a pair of very well-known electromagnetic phenomena: the skin and proximity effects.

In literature, coils of different material and geometries can be found. Currently, most of the AC magnetometers use Litz-wires as coils' conductor to reduce the skin and proximity effects [49, 57, 59]. However, Litz-wires have limitations in both, current intensity and frequency. Thus, the most suitable coils' conductors to produce AMF in magnetic hyperthermia frequencies are the copper pipes [43].

To generate the necessary high AC current to create high AMFs, the main coil has to be fed by a power amplifier (PA). To match the main coil to the power amplifier different approaches are used. Matching capacitors that form a resonant circuit with the main coil, is the most widely employed method. For this purpose, different resonant circuit configurations, like LC-C parallel or LCR series networks, can be designed [49, 59]. The capacitors' values have to be chosen in such a way that the resonant frequency of the circuit is close to the desired frequency of operation.

Multifrequency AC magnetometers enable to study the behavior of magnetic nanoparticles versus frequency, that is crucial for designing suitable magnetic nanoparticles for treatment. Multifrequency AC magnetometers are implemented using resonant circuits with variable capacitors [43].

2.4.1.2 Dynamic magnetization detector system

The dynamic magnetization of the sample, $M(t)$, is measured with pick-up coils systems, where $M(t)$ is induced as a voltage signal according to Faraday's law of induction (see Equation 2.10).

$$V_{pick-up} = -N\frac{\partial \Phi_B}{\partial t} = -N\frac{\mathbf{S}\cdot\partial\mathbf{B}}{\partial t} = -N\mu_0\frac{\mathbf{S}\cdot\partial(\mathbf{H}+\mathbf{M}))}{\partial t} \tag{2.10}$$

where N is the number of turns, S the section of the pick-up coil and Φ_B the magnetic field flux.

The voltage coming from a single pick-up coil that surrounds the sample includes both the time-varying particle magnetization signal and the simultaneous, but undesirable, time-varying excitation magnetic field signal. Unfortunately, it is not possible to subtract the MNPs magnetization signal from the excitation magnetic field signal

because they share the same fundamental frequency. Moreover, the signal at the fundamental frequency of the excitation magnetic field is several orders of magnitude larger than the one coming from MNPs signal (see Figure 2.7).

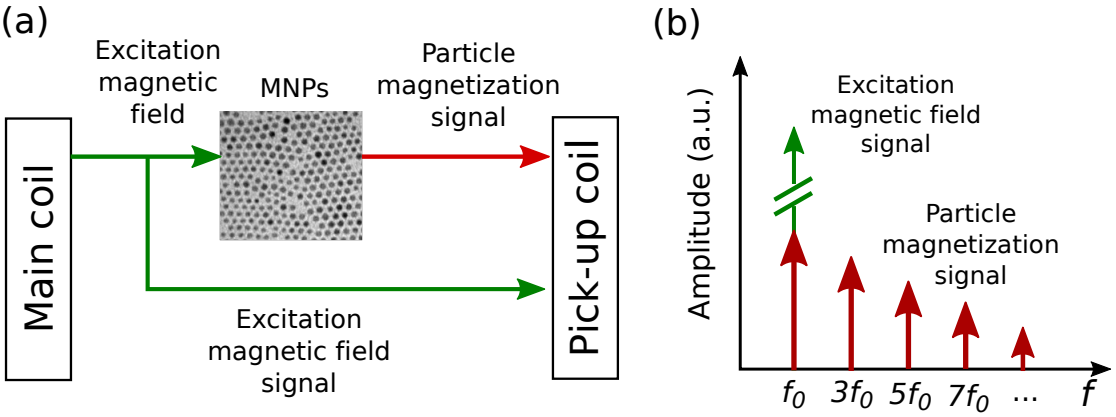

FIGURE 2.7: (a) Simplified block diagram of the AC magnetometer where excitation of the main coil and reception in the pick-up coils occur simultaneously. (b) Frequency spectrum of the signal detected in the pick-up coils. The signal of the magnetic field and particles magnetization share the first harmonic of the pick-up coil frequency spectrum.

In order to remove the excitation magnetic field signal, some authors proposed the use of two coils wound oppositely in such a way that one of the pick-up coil's surrounds the sample and measure its signal and the other (compensation coil) removes the excitation signal [43, 52, 53, 55–57]. With this configuration, ideally, there is no excitation magnetic field signal when a homogeneous magnetic field is applied, allowing the subtraction of the MNPs sample signal. However, that cancellation of the excitation signal cannot be perfect due to magnetic field inhomogeneities and small geometrical differences between pick-up coils. The remaining signal, called feedthrough, can be minimized with a very careful vertical positioning of the pick-up coil system inside the main coil. Additionally, a third coil can be used in order to remove the excitation signal in a finer way [59, 60].However, this last configuration is usually employed in AC magnetometers working in frequencies below 100 kHz.

2.5 Motivation and goals of the thesis: structure of the following chapters

As mentioned before, AC magnetometry is a reliable tool to analyze and understand the parameters that affect the heating performance of magnetic nanoparticles. For designing

MNPs with optimal heating properties for MH, it is vital to provide a comprehensive characterization of the *SAR*. However, the characterization of the heating performance is limited by the experimental working conditions of the current devices. The aim of this Thesis is to develop a powerful AC magnetometer to improve the current characterization technique. To accomplish this goal the Thesis is organized as follows:

The *first* and *second chapters* provide a general introduction of the magnetic hyperthermia treatment. The *third chapter* illustrates three different works to highlight the relevancy of AC magnetometry and to show the limitations arising from the use of current AC magnetometers. All the AC magnetometry measurements of this third chapter are carried out using the AC magnetometer developed in Garaio *et al.* [43]. This device has been modified by new developments: improved pick-up coil system, replaceable main coil and dedicated new LabVIEW program. Based on the needs observed in the works presented in the third chapter (and many others), a new versatile and reliable AC magnetometer for the characterization of the heating performance of MNPs has been designed, built and optimized. The *fourth chapter* is devoted to the development and characterization of the new AC magnetometer. Finally, the *fifth chapter* is dedicated to illustrate the potential of the built AC magnetometer. For that, a series of measurements performed at different magnetic field intensities and frequencies and dispersion media are shown. The results will be discussed in the framework of Stoner-Wohlfarth models for magnetic single domains MNPs.

Bibliography

[1] M. Bañobre-López, A. Teijeiro, and J. Rivas, "Magnetic nanoparticle-based hyperthermia for cancer treatment," *Reports of Practical Oncology & Radiotherapy*, vol. 18, no. 6, pp. 397–400, 2013.

[2] N. I. Hulkoti and T. C. Taranath, "Biosynthesis of nanoparticles using microbes—A review," *Colloids and Surfaces B: Biointerfaces*, vol. 121, pp. 474–483, 2014.

[3] A. Akbarzadeh, M. Samiei, and S. Davaran, "Magnetic nanoparticles: preparation, physical properties, and applications in biomedicine," *Nanoscale Research Letters*, vol. 7, no. 1, p. 144, 2012.

[4] X. Lasheras, M. Insausti, J. M. d. l. Fuente, I. G. d. Muro, I. Castellanos-Rubio, L. Marcano, M. Luisa Fernández-Gubieda, A. Serrano, R. Martín-Rodríguez, E. Garaio, J. Angel García, and L. Lezama, "Mn-Doping level dependence on the magnetic response of Mn x Fe 3x O 4 ferrite nanoparticles," *Dalton Transactions*, vol. 48, no. 30, pp. 11480–11491, 2019.

[5] Z. E. Gahrouei, S. Labbaf, and A. Kermanpur, "Cobalt doped magnetite nanoparticles: Synthesis, characterization, optimization and suitability evaluations for magnetic hyperthermia applications," *Physica E: Low-dimensional Systems and Nanostructures*, vol. 116, p. 113759, 2020.

[6] A.-H. Lu, E. L. Salabas, and F. Schüth, "Magnetic Nanoparticles: Synthesis, Protection, Functionalization, and Application," *Angewandte Chemie International Edition*, vol. 46, no. 8, pp. 1222–1244, 2007.

[7] G. Huang, C.-H. Lu, and H.-H. Yang, "Chapter 3 - Magnetic Nanomaterials for Magnetic Bioanalysis," in *Novel Nanomaterials for Biomedical, Environmental and Energy Applications* (X. Wang and X. Chen, eds.), Micro and Nano Technologies, pp. 89–109, Elsevier, 2019.

[8] R. Hao, R. Xing, Z. Xu, Y. Hou, S. Gao, and S. Sun, "Synthesis, Functionalization, and Biomedical Applications of Multifunctional Magnetic Nanoparticles," *Advanced Materials*, vol. 22, no. 25, pp. 2729–2742, 2010.

[9] M. Goiriena-Goikoetxea, A. García-Arribas, M. Rouco, A. V. Svalov, and J. M. Barandiaran, "High-yield fabrication of 60 nm Permalloy nanodiscs in well-defined magnetic vortex state for biomedical applications," *Nanotechnology*, vol. 27, no. 17, p. 175302, 2016.

[10] S. Shivaji, S. Madhu, and S. Singh, "Extracellular synthesis of antibacterial silver nanoparticles using psychrophilic bacteria," *Process Biochemistry*, vol. 46, no. 9, pp. 1800–1807, 2011.

[11] Y. S. Chan and M. Mat Don, "Biosynthesis and structural characterization of Ag nanoparticles from white rot fungi," *Materials Science and Engineering: C*, vol. 33, no. 1, pp. 282–288, 2013.

[12] M. S. Akhtar, J. Panwar, and Y.-S. Yun, "Biogenic Synthesis of Metallic Nanoparticles by Plant Extracts," *ACS Sustainable Chemistry & Engineering*, vol. 1, no. 6, pp. 591–602, 2013.

[13] S. Kanchi, G. Kumar, A.-Y. Lo, C.-M. Tseng, S.-K. Chen, C.-Y. Lin, and T.-S. Chin, "Exploitation of de-oiled jatropha waste for gold nanoparticles synthesis: A green approach," *Arabian Journal of Chemistry*, vol. 11, no. 2, pp. 247–255, 2018.

[14] D. Sharma, S. Kanchi, and K. Bisetty, "Biogenic synthesis of nanoparticles: A review," *Arabian Journal of Chemistry*, vol. 12, no. 8, pp. 3576–3600, 2019.

[15] I. Orue, L. Marcano, P. Bender, A. García-Prieto, S. Valencia, M. A. Mawass, D. Gil-Cartón, D. A. Venero, D. Honecker, A. García-Arribas, L. F. Barquín, A. Muela, and M. L. Fdez-Gubieda, "Configuration of the magnetosome chain: a natural magnetic nanoarchitecture," *Nanoscale*, vol. 10, no. 16, pp. 7407–7419, 2018.

[16] A. Muela, D. Muñoz, R. Martín-Rodríguez, I. Orue, E. Garaio, A. Abad Díaz de Cerio, J. Alonso, J. García, and M. L. Fdez-Gubieda, "Optimal Parameters for Hyperthermia Treatment Using Biomineralized Magnetite Nanoparticles: Theoretical and Experimental Approach," *The Journal of Physical Chemistry C*, vol. 120, no. 42, pp. 24437–24448, 2016.

[17] T. D. Schladt, K. Schneider, H. Schild, and W. Tremel, "Synthesis and bio-functionalization of magnetic nanoparticles for medical diagnosis and treatment," *Dalton Transactions*, vol. 40, no. 24, pp. 6315–6343, 2011.

[18] C.-A. J. Lin, R. A. Sperling, J. K. Li, T.-Y. Yang, P.-Y. Li, M. Zanella, W. H. Chang, and W. J. Parak, "Design of an Amphiphilic Polymer for Nanoparticle Coating and Functionalization," *Small*, vol. 4, no. 3, pp. 334–341, 2008.

[19] I. Castellanos-Rubio, I. Rodrigo, A. Olazagoitia-Garmendia, O. Arriortua, I. Gil de Muro, J. S. Garitaonandia, J. R. Bilbao, M. L. Fdez-Gubieda, F. Plazaola, I. Orue, A. Castellanos-Rubio, and M. Insausti, "Highly Reproducible Hyperthermia Response in Water, Agar, and Cellular Environment by Discretely PEGylated Magnetite Nanoparticles," *ACS Applied Materials & Interfaces*, vol. 12, no. 25, pp. 27917–27929, 2020.

[20] S. Richard, M. Boucher, A. Saric, A. Herbet, Y. Lalatonne, P. X. Petit, S. Mériaux, D. Boquet, and L. Motte, "Optimization of pegylated iron oxide nanoplatforms for antibody coupling and bio-targeting," *Journal of Materials Chemistry B*, vol. 5, no. 16, pp. 2896–2907, 2017.

[21] M. Wang and M. Thanou, "Targeting nanoparticles to cancer," *Pharmacological Research*, vol. 62, no. 2, pp. 90–99, 2010.

[22] B. Cullity and C. Graham, "Domains and the Magnetization Process," in *Introduction to Magnetic Materials*, pp. 275–333, John Wiley & Sons, Ltd, 2008.

[23] D. Serantes and D. Baldomir, "Superparamagnetism and Monte Carlo Simulations," *The Open Surface Science Journal*, vol. 4, no. 1, 2012.

[24] B. D. Cullity and C. Graham, "Fine Particles and Thin Films," in *Introduction to Magnetic Materials*, pp. 359–408, John Wiley & Sons, Ltd, 2008.

[25] J. Carrey, B. Mehdaoui, and M. Respaud, "Simple models for dynamic hysteresis loop calculations of magnetic single-domain nanoparticles: Application to magnetic hyperthermia optimization," *Journal of Applied Physics*, vol. 109, no. 8, p. 083921, 2011.

[26] B. D. Cullity and C. Graham, "Magnetic Anisotropy," in *Introduction to Magnetic Materials*, pp. 197–239, John Wiley & Sons, Ltd, 2008.

[27] S. Chikazumi and S. Charap, *Physics of Magnetism*. John Wiley & Sons, Incorporated, 1964.

[28] D. Gandia, L. Gandarias, L. Marcano, I. Orue, D. Gil-Cartón, J. Alonso, A. García-Arribas, A. Muela, and M. L. Fdez-Gubieda, "Elucidating the role of shape anisotropy in faceted magnetic nanoparticles using biogenic magnetosomes as a model," *Nanoscale*, vol. 12, no. 30, pp. 16081–16090, 2020.

[29] N. A. Usov and J. M. Barandiarán, "Magnetic nanoparticles with combined anisotropy," *Journal of Applied Physics*, vol. 112, no. 5, p. 053915, 2012.

[30] E. C. Stoner and E. P. Wohlfarth, "A mechanism of magnetic hysteresis in heterogeneous alloys," *Philosophical Transactions of the Royal Society of London. Series A, Mathematical and Physical Sciences*, vol. 240, no. 826, pp. 599–642, 1948.

[31] W. F. Brown, "Thermal Fluctuations of a Single-Domain Particle," *Physical Review*, vol. 130, no. 5, pp. 1677–1686, 1963.

[32] R. Rosensweig, "Heating magnetic fluid with alternating magnetic field," *Journal of Magnetism and Magnetic Materials*, vol. 252, pp. 370–374, 2002.

[33] E. Lima, T. E. Torres, L. M. Rossi, H. R. Rechenberg, T. S. Berquo, A. Ibarra, C. Marquina, M. R. Ibarra, and G. F. Goya, "Size dependence of the magnetic relaxation and specific power absorption in iron oxide nanoparticles," *Journal of Nanoparticle Research*, vol. 15, no. 5, p. 1654, 2013.

[34] M. Ma, Y. Wu, J. Zhou, Y. Sun, Y. Zhang, and N. Gu, "Size dependence of specific power absorption of Fe3O4 particles in AC magnetic field," *Journal of Magnetism and Magnetic Materials*, vol. 268, no. 1, pp. 33–39, 2004.

[35] L. C. Branquinho, M. S. Carrião, A. S. Costa, N. Zufelato, M. H. Sousa, R. Miotto, R. Ivkov, and A. F. Bakuzis, "Effect of magnetic dipolar interactions on nanoparticle heating efficiency: Implications for cancer hyperthermia," *Scientific Reports*, vol. 3, no. 1, p. 2887, 2013.

[36] Z. Nemati, J. Alonso, I. Rodrigo, R. Das, E. Garaio, J. García, I. Orue, M.-H. Phan, and H. Srikanth, "Improving the Heating Efficiency of Iron Oxide Nanoparticles by Tuning Their Shape and Size," *The Journal of Physical Chemistry C*, vol. 122, no. 4, pp. 2367–2381, 2018.

[37] J.-P. Fortin, C. Wilhelm, J. Servais, C. Ménager, J.-C. Bacri, and F. Gazeau, "Size-Sorted Anionic Iron Oxide Nanomagnets as Colloidal Mediators for Magnetic Hyperthermia," *Journal of the American Chemical Society*, vol. 129, no. 9, pp. 2628–2635, 2007.

[38] M. Bekovic and A. Hamler, "Determination of the Heating Effect of Magnetic Fluid in Alternating Magnetic Field," *IEEE Transactions on Magnetics*, vol. 46, no. 2, pp. 552–555, 2010.

[39] C. L. Dennis, K. L. Krycka, J. A. Borchers, R. D. Desautels, J. v. Lierop, N. F. Huls, A. J. Jackson, C. Gruettner, and R. Ivkov, "Internal Magnetic Structure of Nanoparticles Dominates Time-Dependent Relaxation Processes in a Magnetic Field," *Advanced Functional Materials*, vol. 25, no. 27, pp. 4300–4311, 2015.

[40] E. Natividad, M. Castro, and A. Mediano, "Accurate measurement of the specific absorption rate using a suitable adiabatic magnetothermal setup," *Applied Physics Letters*, vol. 92, no. 9, p. 093116, 2008.

[41] S.-Y. Wang, S. Huang, and D.-A. Borca-Tasciuc, "Potential Sources of Errors in Measuring and Evaluating the Specific Loss Power of Magnetic Nanoparticles in an Alternating Magnetic Field," *IEEE Transactions on Magnetics*, vol. 49, no. 1, pp. 255–262, 2013.

[42] F. Soetaert, S. K. Kandala, A. Bakuzis, and R. Ivkov, "Experimental estimation and analysis of variance of the measured loss power of magnetic nanoparticles," *Scientific Reports*, vol. 7, no. 1, p. 6661, 2017.

[43] E. Garaio, J. M. Collantes, F. Plazaola, J. A. Garcia, and I. Castellanos-Rubio, "A multifrequency eletromagnetic applicator with an integrated AC magnetometer for magnetic hyperthermia experiments," *Measurement Science and Technology*, vol. 25, no. 11, p. 115702, 2014.

[44] I. Andreu and E. Natividad, "Accuracy of available methods for quantifying the heat power generation of nanoparticles for magnetic hyperthermia," *International Journal of Hyperthermia*, vol. 29, no. 8, pp. 739–751, 2013.

[45] I. Morales, R. Costo, N. Mille, G. B. Da Silva, J. Carrey, A. Hernando, and P. De la Presa, "High Frequency Hysteresis Losses on -Fe2O3 and Fe3O4: Susceptibility as a Magnetic Stamp for Chain Formation," *Nanomaterials*, vol. 8, no. 12, p. 970, 2018.

[46] B. Mehdaoui, R. P. Tan, A. Meffre, J. Carrey, S. Lachaize, B. Chaudret, and M. Respaud, "Increase of magnetic hyperthermia efficiency due to dipolar interactions in low-anisotropy magnetic nanoparticles: Theoretical and experimental results," *Physical Review B*, vol. 87, no. 17, p. 174419, 2013.

[47] J. M. Asensio, J. Marbaix, N. Mille, L.-M. Lacroix, K. Soulantica, P.-F. Fazzini, J. Carrey, and B. Chaudret, "To heat or not to heat: a study of the performances of iron carbide nanoparticles in magnetic heating," *Nanoscale*, vol. 11, no. 12, pp. 5402–5411, 2019.

[48] I. Castellanos-Rubio, I. Rodrigo, R. Munshi, O. Arriortua, J. S. Garitaonandia, A. Martinez-Amesti, F. Plazaola, I. Orue, A. Pralle, and M. Insausti, "Outstanding heat loss *via* nano-octahedra above 20 nm in size: from wustite-rich nanoparticles to magnetite single-crystals," *Nanoscale*, vol. 11, no. 35, pp. 16635–16649, 2019.

[49] D. Cabrera, A. Coene, J. Leliaert, E. J. Artés-Ibáñez, L. Dupré, N. D. Telling, and F. J. Teran, "Dynamical Magnetic Response of Iron Oxide Nanoparticles Inside Live Cells," *ACS Nano*, vol. 12, no. 3, pp. 2741–2752, 2018.

[50] M. Veverka, P. Veverka, O. Kaman, A. Lančok, K. Závěta, E. Pollert, K. Knížek, J. Boháček, M. Beneš, P. Kašpar, E. Duguet, and S. Vasseur, "Magnetic heating by cobalt ferrite nanoparticles," *Nanotechnology*, vol. 18, no. 34, p. 345704, 2007.

[51] H. Kobayashi, K. Ueda, A. Tomitaka, T. Yamada, and Y. Takemura, "Self-Heating Property of Magnetite Nanoparticles Dispersed in Solution," *IEEE Transactions on Magnetics*, vol. 47, no. 10, pp. 4151–4154, 2011.

[52] B. Mehdaoui, J. Carrey, M. Stadler, A. Cornejo, C. Nayral, F. Delpech, B. Chaudret, and M. Respaud, "Influence of a transverse static magnetic field on the magnetic hyperthermia properties and high-frequency hysteresis loops of ferromagnetic FeCo nanoparticles," *Applied Physics Letters*, vol. 100, no. 5, p. 052403, 2012.

[53] S. A. Gudoshnikov, B. Y. Liubimov, and N. A. Usov, "Hysteresis losses in a dense superparamagnetic nanoparticle assembly," *AIP Advances*, vol. 2, no. 1, p. 012143, 2012.

[54] M. Beković, M. Trlep, M. Jesenik, V. Goričan, and A. Hamler, "An experimental study of magnetic-field and temperature dependence on magnetic fluid's heating power," *Journal of Magnetism and Magnetic Materials*, vol. 331, pp. 264–268, 2013.

[55] S. A. Gudoshnikov, B. Y. Liubimov, Y. S. Sitnov, V. S. Skomarovsky, and N. A. Usov, "AC Magnetic Technique to Measure Specific Absorption Rate of Magnetic Nanoparticles," *Journal of Superconductivity and Novel Magnetism*, vol. 26, no. 4, pp. 857–860, 2013.

[56] M. Veverka, K. Závěta, O. Kaman, P. Veverka, K. Knížek, E. Pollert, M. Burian, and P. Kašpar, "Magnetic heating by silica-coated Co–Zn ferrite particles," *Journal of Physics D: Applied Physics*, vol. 47, no. 6, p. 065503, 2014.

[57] V. Connord, B. Mehdaoui, R. P. Tan, J. Carrey, and M. Respaud, "An air-cooled Litz wire coil for measuring the high frequency hysteresis loops of magnetic samples—A useful setup for magnetic hyperthermia applications," *Review of Scientific Instruments*, vol. 85, no. 9, p. 093904, 2014.

[58] S. K. Avugadda, M. E. Materia, R. Nigmatullin, D. Cabrera, R. Marotta, T. F. Cabada, E. Marcello, S. Nitti, E. J. Artés-Ibañez, P. Basnett, C. Wilhelm, F. J. Teran, I. Roy, and T. Pellegrino, "Esterase-Cleavable 2D Assemblies of Magnetic Iron Oxide Nanocubes: Exploiting Enzymatic Polymer Disassembling To Improve Magnetic Hyperthermia Heat Losses," *Chemistry of Materials*, vol. 31, no. 15, pp. 5450–5463, 2019.

[59] P. Lenox, L. K. Plummer, P. Paul, J. E. Hutchison, A. Jander, and P. Dhagat, "High-Frequency and High-Field Hysteresis Loop Tracer for Magnetic Nanoparticle Characterization," *IEEE Magnetics Letters*, vol. 9, pp. 1–5, 2018.

[60] N. Garraud, R. Dhavalikar, L. Maldonado-Camargo, D. P. Arnold, and C. Rinaldi, "Design and validation of magnetic particle spectrometer for characterization of magnetic nanoparticle relaxation dynamics," *AIP Advances*, vol. 7, no. 5, p. 056730, 2017.

Chapter 3

Analyzing MNP parameters via AC magnetometry to improve their SAR

In order to achieve an efficient magnetic hyperthermia treatment, magnetic nanoparticles should display the best heating properties and generate as much heat as possible, for the clinically acceptable $H \cdot f$ limit, at the lowest particle content. This is especially important in cases where direct injection of the particles into the tumor site is not possible and the MNPs have to be delivered by intravenous injection, as it is the case with deep or spread tumors.

Understanding the parameters that increase the SAR is vital to design MNPs with optimal heating performance. As explained in Chapter 2, SAR highly depends on physicochemical properties of the nanoparticles such as composition, size, shape, and crystallinity [1–3]. In addition, arrangements formed by dipolar interactions also affect the heating performance of MNPs. In general, dipolar interactions have been shown to hinder SAR [2]. However, some works in literature have reported that specific arrangement formed by dipolar interaction, like chain-like structures, increase the heating efficacy due to their ability to mechanically orient along the field lines [2, 4, 5].

On the other hand, the MNPs dispersion media also plays an important role in the heating performance. Media with high viscosity, such as biological environment,

leads to substantial decrease of *SAR* due to the enhancement of MNPs clustering or the suppression of the rotation of the MNPs, either inside cells or within the extracellular environment [6–8].

As mentioned before, AC magnetometry is a very valuable characterization technique due to the influence of MNPs' properties on the shape of the AC hysteresis loops. Aiming to explore the potential of AC magnetometry in the development of new strategies to improve the *SAR*, several studies carried out by different research groups in collaboration with the author of this PhD thesis, are shown in the present chapter.

The first section aims to explain the reason behind the high heating power generated by magnetotactic bacteria (MTB)[9]. The work presented in this section has been performed in collaboration with the group of Magnetism and Magnetic Materials of the Department of Electricity and Electronics at the University of the Basque Country (EHU/UPV).

The second section studies the effect of the morphology of octahedral shape MNPs in their *SAR* [10]. Finally, the last section explores the influence of the coatings of MNPs in their magnetic response and develops a new strategy to obtain MNPs with high reproducible hyperthermia response in different dispersion media [11]. These last works have been developed in collaboration with the Department of Inorganic Chemistry of the University of the Basque Country (EHU/UPV).

It has to be pointed out that the objective of this chapter is not to present a deep analysis of each work and to explain all the characterization procedures and results, but to emphasize the importance of the AC magnetometry. That is why, only the most relevant measurements for understanding the AC magnetometry results are exposed.

3.1 Magnetotactic bacteria as magnetic hyperthermia agent

Magnetospirillum gryphiswaldense MSR-1 is a magnetotactic bacteria (MTB) strain that synthesizes magnetosomes chains with helical shaped structure. The high potential of MSR-1 as magnetic hyperthermia agent has been revealed by calorimetry experiments. However, this technique doesn't provide any information about the reason behind their high heating performance. In order to understand the heating mechanism of the MSR-1

an AC magnetometry study is performed. The analysis is conducted under different AC magnetic field and frequency conditions as well as diverse dispersion media and alignments of the bacteria.

Figure 3.1 (a) shows the AC hysteresis loops of MSR-1 bacteria randomly suspended in water with a magnetite concentration of 0.15 mg ml^{-1}. As it can be observed, the AC hysteresis loops below 15 mT are narrow, with low squareness and low maximum magnetization. However, above 25 mT, the loops broaden to a square shape.

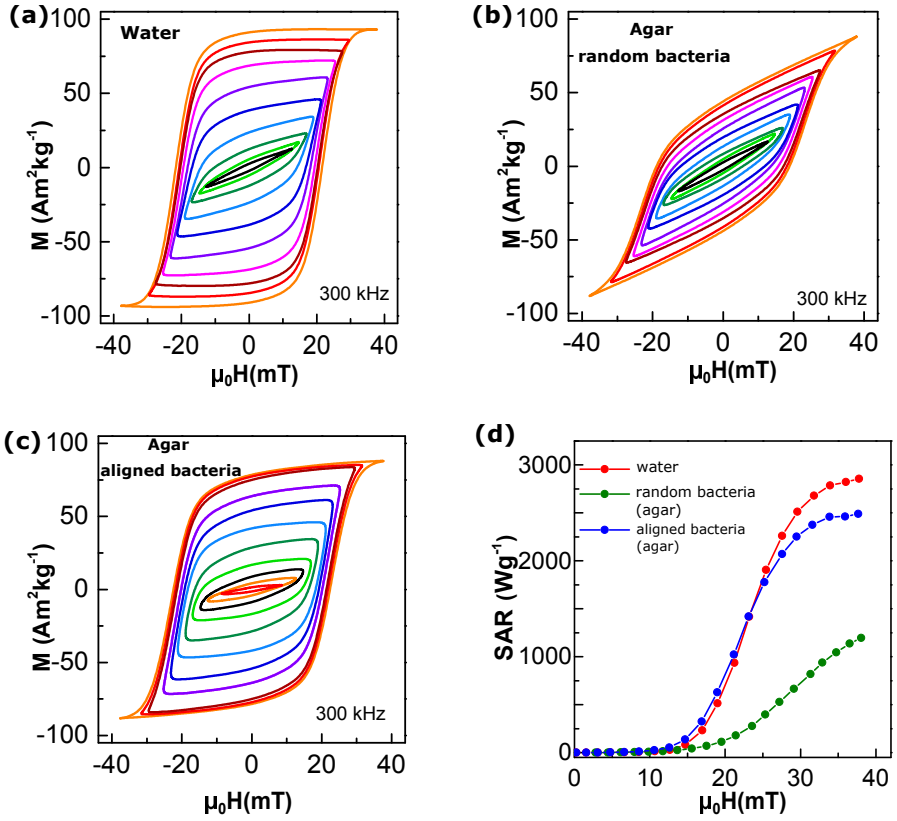

FIGURE 3.1: AC hysteresis loops of MSR-1 dispersed in (a) water, (b) randomly in agar and (c) aligned in agar. The measurements are carried out at magnetic field intensities up to 40 mT and frequency of 300 kHz. Hysteresis loops of sample (a) and (c) are highly squared while sample (b) shows titled and not saturated loops. (d) *SAR* versus magnetic field intensity curve of the three samples, obtained from the AC hysteresis loops.

As explained in Chapter 2, the *SAR* is calculated directly from the area of the AC hysteresis loops. Therefore, the optimum shape of the AC hysteresis loops in order to maximize the area and *SAR* is a square shape with high coercivity and remanence, just like the one obtained with the water dispersed bacteria.

Simulations carried out by different groups suggest that aligned chain-like structures of magnetic nanoparticles, exhibiting a well-defined anisotropy axis, could give rise to

AC loops that resemble this square shape [12–14]. Consequently, the obtained results suggest that the bacteria aligns itself with the direction of the magnetic field.

In order to better understand the role of the alignment of the bacteria, AC magnetometry measurements are carried out in agar medium using bacteria randomly dispersed and aligned parallel to the AC field (Figure 3.2 shows the protocol followed to prepare each sample). The agar restricts the mechanical rotation of the particles and also fixes the bacteria in the set orientation, which allows us to study the effect of the alignment on their heating efficiency. As it can be seen in Figure 3.1 (b) when bacteria are randomly oriented in agar the AC hysteresis loops show different shape: titled and not saturated.

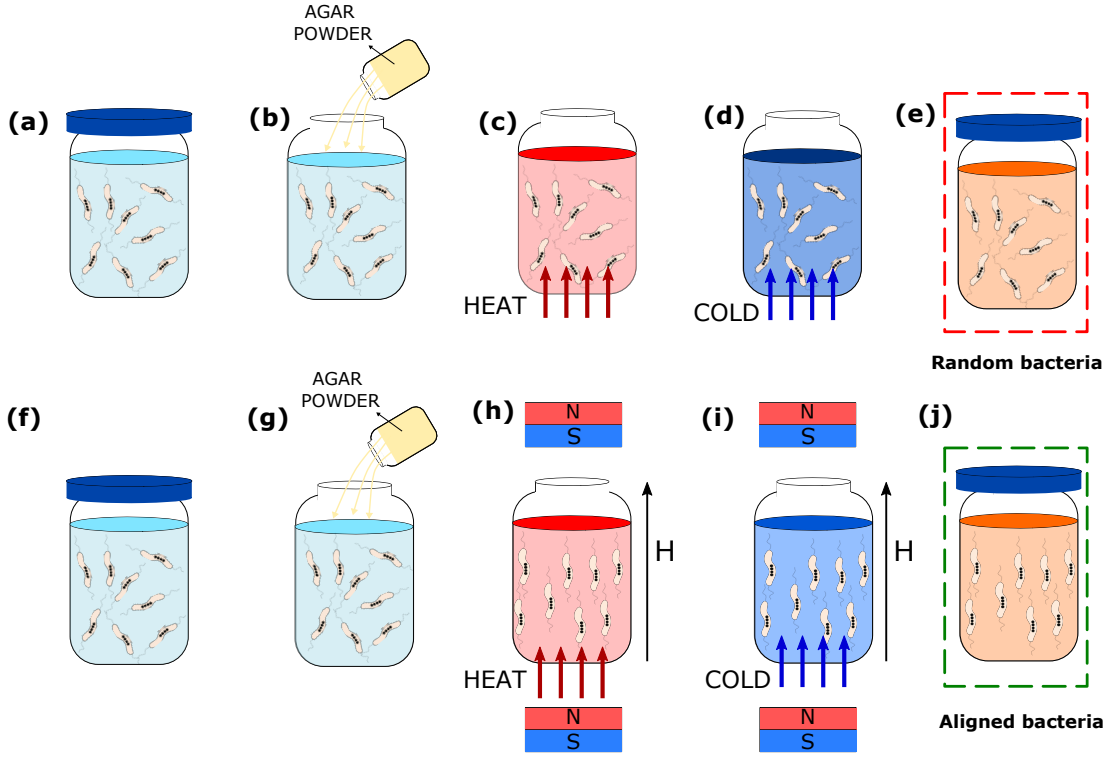

FIGURE 3.2: The following steps are performed to prepare the two samples dispersed in agar. First row: Randomly dispersed bacteria in agar. (a) MSR-1 bacteria are dispersed into water, (b) agar powder is added into water sample containing bacteria,(c) the sample is heated using a laboratory heating plate (d) the sample is cooled using liquid nitrogen and (e) the agar gel is generated with randomly dispersed bacteria. Second row: bacteria aligned parallel to the AC field in agar. (f) MSR-1 bacteria are dispersed into water, (g) agar powder is added into water sample containing bacteria,(h) the sample is heated while a high DC magnetic field is applied using a magnet (i) the sample is cooled while the magnetic field is kept working and (j) the agar gel is generated with aligned bacteria. The figure is a mere description of the methods followed by Gandía et al in [9], for the orientation and gelling of MSR-1 bacteria.

Additionally, AC hysteresis loops of magnetotactic bacteria aligned parallel to the AC magnetic field are practically identical to the one of bacteria dispersed in water

(see Figure 3.1 (c)). This verifies that the AC magnetic field at magnetic hyperthermia frequencies orients efficiently magnetotactic bacteria. The magnetization reversal in water is driven by intrinsic dynamical processes, just like in fixed bacteria. Consequently, mechanical rotation of the chain of magnetosomes (Brownian relaxation) plays a minor role in the heating performance of magnetotactic bacteria. This makes sense, because the velocity response to external fields is much lower than the one needed to follow the applied magnetic field at magnetic hyperthermia frequencies.

In order to verify the potential of MTB as hyperthermia agent the SAR of MTB is compared with the SAR of extracted magnetosomes (magnetosomes without bacteria). This last data is taken from Muela *et al.* [15].

As it can be seen in Figure 3.3 the SAR/f values for the extracted magnetosomes dispersed in water are clearly lower than those obtained for MTB. As explained before, this is caused by the alignment of the bacteria with the applied AMF, giving rise to a square shape hysteresis loops (see the inset of the Figure 3.3).

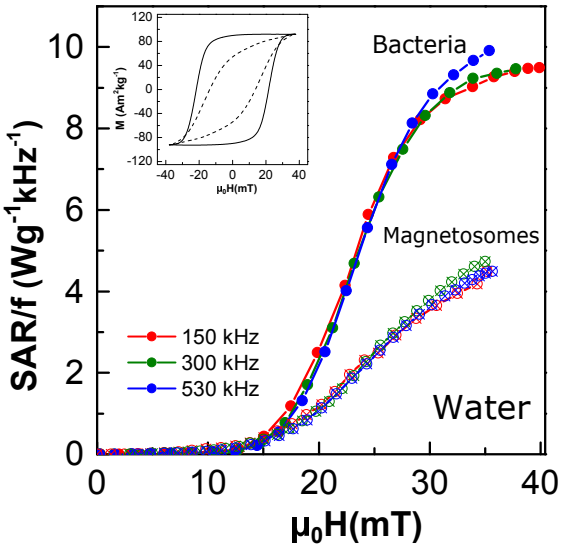

FIGURE 3.3: SAR/f vs magnetic field intensity curves (at intensities up to 40 mT and frequencies of 150, 300 and 530 kHz) for MTB bacteria and extracted magnetosomes (magnetosomes data is taken from Gandía *et al.* [9] work). In the inset, AC hysteresis loops are presented corresponding to the bacteria (solid line) and extracted magnetosomes (dashed line).

On the other hand, the tendency of SAR/f vs magnetic field of both, the bacteria and the extracted magnetosomes is very similar. At fields up to 15 mT the energy absorbance is very limited, whereas above this limit SAR/f shows a steeply increase tending to saturate at high fields. Finally, SAR/f of magnetosomes and MTB increase

linearly with frequency, since the SAR/f curves measured at 150, 300 and 530 kHz collapse in a single curve. This type of behavior fits well within the Stoner–Wohlfarth models for single domain nanoparticles.

In conclusion, AC magnetometry enables to understand that the high SAR values (see Figure 3.3) arise from the alignment of the bacteria with the applied magnetic field. It is also shown that the mechanical rotation (Brownian relaxation) of the chain of magnetosomes is not playing an important role in the obtained high SAR values. Thus, magnetotactic bacteria will still be able to provide high heating in biological environment.

Although AC magnetometry becomes a very useful technique in this work, it is important to remark, that the AC magnetometer maximum working field, avoids carrying out a more detailed analysis of the heating mechanism of MSR-1 bacteria. As it can be observed in Figure 3.1 (d), SAR vs magnetic field curves have a clear tendency towards saturation, however, the whole saturated curve can not be obtained which limits the theoretical study of the MTB.

3.2 Correlation between the shape of the MNPs and their hyperthermia performance

Analyzing the influence of different parameter, such as, size and shape, in magnetic anisotropy is crucial for enhancing the heating efficiency of MNPs. Concerning the size, typically superparamagnetic nanoparticles (SP-MNPs) are used in magnetic hyperthermia due to the absence of remanent magnetization and high heating power at low magnetic fields. However, magnetic nanoparticles with fixed magnetic moments (F-MNPs) offer a much larger magnetic response than SP-MNPs and high heating power at large enough magnetic fields. Nevertheless, F-MNPs tend to agglomerate due to the strong magnetic interactions which drastically decrease the efficiency.

Thus, a significant improvement would be attainable by the production of iron oxide F-MNPs that do not present substantial agglomeration. Consequently, the search for the best F-MNPs involves optimizing intrinsic properties, such as shape and crystallinity, as well as extrinsic ones, which are driven by the strong polar interactions.

However, synthesizing F-MNPS (larger than 25 nm) with, low size and shape dispersity, preventing the formation of secondary phases, is still challenging. This makes difficult to rise a clear conclusion about the link between shape and magnetic properties and thus there is some controversy about this issue in literature [16–19]. In an effort to explore the role of the shape F-MNPs in magnetic hyperthermia, novel magnetite MNPs with an octahedral morphology and narrow shape/size distributions are synthesized (see Figure 3.4) and their heating properties are studied by AC magnetometry under different AC magnetic fields and dispersion media. To enhance colloidal stability in physiological media and to avoid cluster formation generated by dipolar interactions, the F-MNPs are coated with an amphiphilic copolymer (PMAO- grafted-PEG).

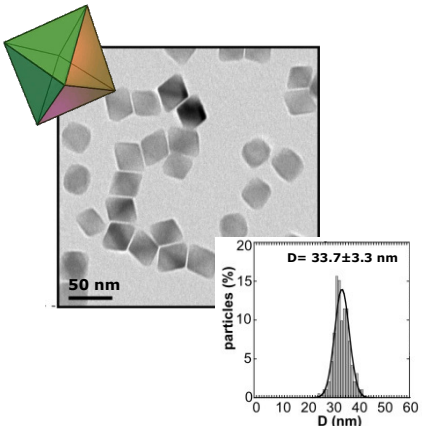

FIGURE 3.4: Transmission electron microscopy (TEM) image of the synthesized F-MNPS with their corresponding size distribution histogram.mThe F-MNP shows an octahedral morphology and a narrow size distribution.

Figure 3.5 (a) shows the AC hysteresis loops and SAR curves at different magnetic field intensities (up to 40 mT) and frequency of 300 kHz for F-MNPs dispersed in water. As it can be observed, AC hysteresis loops present almost a square shape with a coercive field of 18 mT and reduced remanence of approximately 0.6. In consequence, high SAR values of 1200 Wg^{-1} are achieved at maximum magnetic field (see red curve of Figure 3.5 (d)). It is worth mentioning that the coercivity and SAR values obtained for our octahedral F-MNPs are appreciably higher than those reported in the literature for magnetite systems of similar sizes [2].

Square AC hysteresis loops can be observed in chain like formations with anisotropy axis orientated in the direction of the magnetic field, such as those studies in the previous section with magnetotactic bacteria; but also, in some particles with specific shape anisotropy [20].

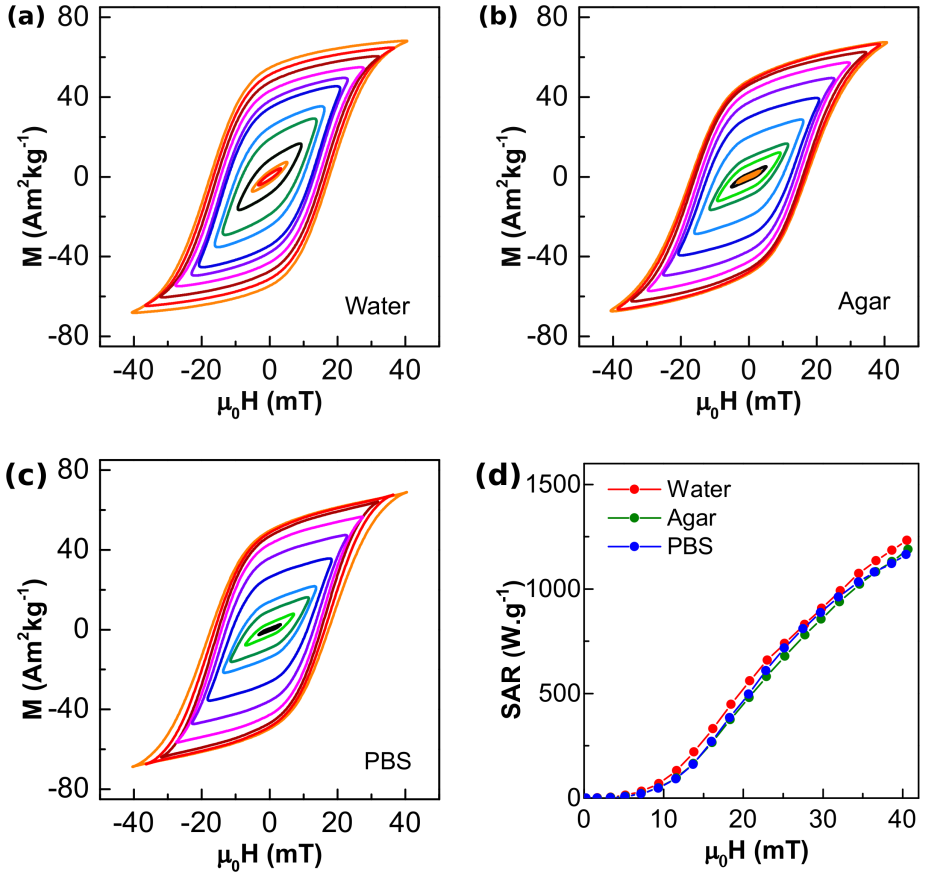

FIGURE 3.5: AC hysteresis loops of the F-MNPs sample dispersed in (a) water, (b) agar and (c) PBS. The measurements are carried out at magnetic field intensities up to 40 mT and frequency of 300 kHz. (d) The corresponding *SAR* vs magnetic field curves. As it can be observed the heating efficiency of the F-MNPs remains invariable in the three dispersion media.

In order to get a better understanding of the origin of the shape of the AC hysteresis loops AC magnetometry measurements are carried out in physiological media ((phosphate-buffered saline) (PBS)) and agar (see Figure 3.5 (b) and (c)). As it is done with MTB (see Section 3.1), agar is used to eliminate a hypothetical Brownian contribution to the *SAR* and to avoid mechanical rotation of aggregates and/or small chains towards the AC magnetic field direction. In this way, the influence of a possible MNP arrangement in the heating behavior can be analyzed.

As Figure 3.5 (d) shows, AC hysteresis loops and *SAR* versus magnetic field curve of F-MNPs dispersed in water, physiological media and agar are almost identical. Relevant information can be obtained from this data: First, the mechanical rotation of particles is

not playing a significant role in the hyperthermia performance. Second, magnetic properties are mostly correlated to particles' shape and not to their aggregation state. Third, the squaring of the loops (with reduced remanence higher than 0.5) should be related to the particular morphology of these octahedral particles and not to the orientation of any chain formation, as it happened with the MTB. And fourth, the magnetic response of the octahedral shape F-MNPs maintains invariable in different dispersion media.

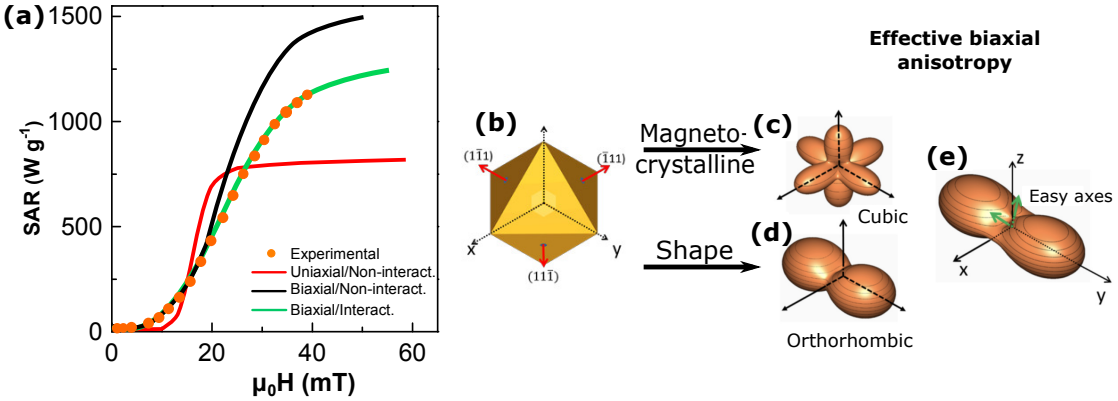

FIGURE 3.6: (e) Experimental (orange dots) and simulated *SAR* vs magnetic field curves. Simulations are carried out by solving dynamical Laudau–Liftshitz–Gilbert equation considering: non-interacting particles with uniaxial anisotropy (red solid line), non-interacting particles with biaxial anisotropy (black solid line) and interacting particles with biaxial anisotropy (green solid line).(b) Morphology of the sample employed in this work approaches an ideal octahedron. (c) Energy surface of magnetocrystalline anisotropy of magnetite. (d) Energy surface of the proposed shape anisotropy of octahedra with an orthorhombic symmetry. (e) Energy surface of the resulting anisotropy energy of octahedral magnetite particles: biaxial anisotropy.

Finally, in order to analyze how octahedral shape influences the magnetic anisotropy, dynamic hysteresis loops and *SAR* curves are simulated using a model based on the Laudau–Liftshitz–Gilbert equation [21]. As it can be easily deduced from the Figure 3.6 (a), a model considering non-interacting MNPs system with uniaxial anisotropy (red solid line) is very far from the experimental results (orange dots). Thus, for the successive simulation the effects of both monocrystalline and shape anisotropies are considered. As it can be observed in transmission electron microscopy (TEM) images, the octahedral shape is not completely perfect, so, an orthorhombic shape anisotropy is proposed. In this way the resulting anisotropy is biaxial (see Figure 3.6 (b)-(e)), with a remanent magnetization larger than the expected one in uniaxial systems.

However, simulations carried out with non-interacting MNPs with biaxial anisotropy (black solid line) show certain discrepancy with the experimental *SAR* curve. Note that it is not very realistic to consider completely non interacting F-MNPs. Thus, for fitting

SAR curve the influence of dipolar interactions needs to be taken into account. With these implementations the calculations are very consistent with experimental data as it is observed in Figure 3.6 (a) (green solid line).

It can be concluded that AC magnetometry allows to uncover the origin of square shape AC hysteresis loops and high *SAR* values of the octahedral shape MNPs employed in this work. In this case, the squaring of the loops is mostly associated with the MNPs morphology and not from MNPs arrangements (as it happened with magnetotactic bacteria), consequently their behavior in cell environments is not diminished, which make them ideal candidate for magnetic hyperthermia treatment.

However, it should be mentioned that *SAR(H)* curves are not saturated. Thus, although the AC magnetometer employed in this work leads to very useful information to study the magnetic anisotropy of the octahedral shape F-MNPs, the provided anisotropy values are less accurate than those that would be obtained from saturated curves.

3.3 Development of new strategies to keep constant the heating performance of MNPs in media with different viscosities

F-MNPs present intense magnetic dipolar interactions and tend to form large agglomerations that provoke a significant reduction of *SAR*. To minimize chaotic dipolar interactions of F-MNPs, prevent the formation of large clusters and keep constant their heating performance in biological environments a novel polymeric (PMAO-PEG) coating protocol is developed. The new protocol is carried out analyzing the effect of different parameters of the coating procedure (amount of monomers that are added per nm^2 of MNP surface, concentration, solvent used in the initial F-MNPs colloids and PMAO-PEG solutions, and so forth) on the aggregation degree of the MNPs through AC magnetometry.

The PMAO-PEG coating effect on Fe_3O_4 MNPs of different sizes (23 $\pm$ 2 nm (sample A) and 29 $\pm$ 3 nm (sample B)) is analyzed. But firstly, and for simplicity, the coating protocol is refined using the smallest F-MNPs (23 nm, sample A). Table 3.1

summarizes the most representative preparations, in which one coating parameter at a time is modified.

Preparation name	**Monomers/nm^2**	**[PMAO-PEG] (mg$_{PMAO}$/ml)**	**Solvent of the PMAO-PEG stock**	**Mixing strategy (F-MNPs + PMAO-PEG)**	***SAR*** **(Wg^{-1})**
1	100	0.5	$CHCl_3$	pouring	280
2	50	0.5	$CHCl_3$	pouring	490
3	50	0.5	$CHCl_3$:EtOH	pouring	405
4	50	0.5	$CHCl_3$:Hexane	pouring	365
5	50	0.5	$CHCl_3$	dropwise	570
6	50	5	$CHCl_3$	dropwise	670

TABLE 3.1: Summary of the parameters used in the coating procedure of some representative preparations: PMAO monomers added per nm^2 of MNP surface, concentration of the PMAO-PEG copolymer, solvent of the PMAO-PEG stock solution, strategy used to mix the F-MNPs with the PMAO-PEG and the corresponding *SAR* value obtained in the final sample A.

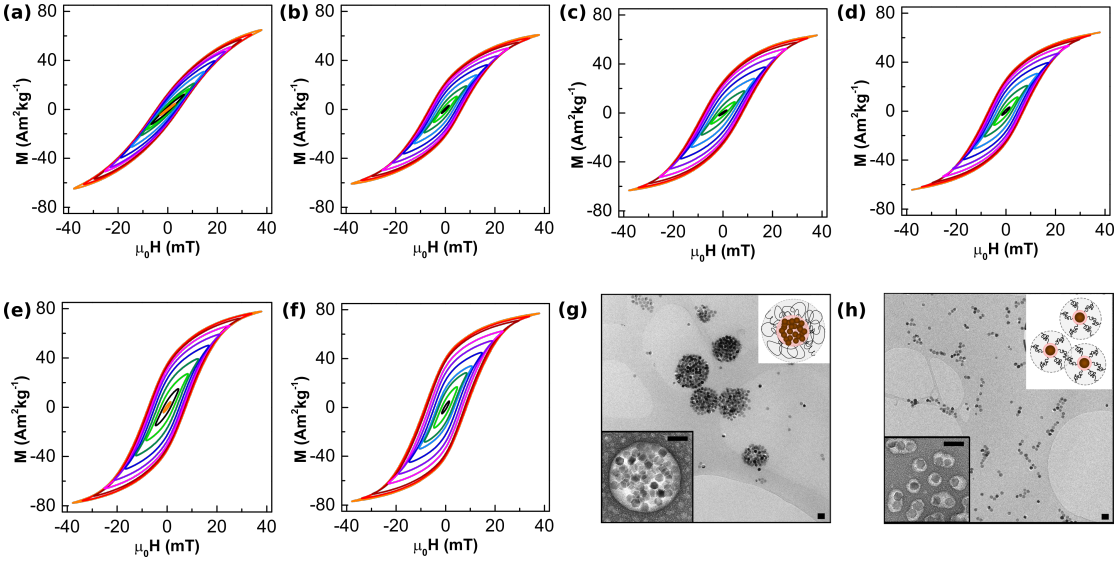

FIGURE 3.7: (a)-(f) AC hysteresis loops of preparation 1-6 shown in Table 3.1. TEM micrography of (g) preparation 1 and (h) preparation 6. Inset: negative staining micrographs.

The agglomeration degree of the F-MNPs in these preparations can be deduced from the dynamic hysteresis loops shape (see Figure 3.7 (a)-(f)) and the corresponding *SAR* value (see Table 3.1). From a qualitative point of view, when clustering and interactions are playing an important role the AC hysteresis loops are narrow and tilted, whereas they became wider and less tilted when particles do not form significant clusters (with the exception of chain like formations analyzed in the previous sections). Thus, it can be deduced, that preparation 1 (see Figure 3.7 (a)) which shows narrow and tilted AC

hysteresis loops forms big cluster, while, preparation 6 (see Figure 3.7 (f)) with wider and more square hysteresis loops present individual coatings. The different coating structures deduced from AC hysteresis loops can be clearly observed in the negative staining TEM micrography (see Figure 3.7 (g)-(h)): collective coating in preparation 1 and quasi individually coating in preparation 6.

From the monitorization of the AC hysteresis loops of all the preparations, it is deduced that the coating parameters employed in the preparation 6 are the optimum ones for obtaining individual coatings. It is found that the mixing strategy of the MNPs with PMAO-PEG copolymer is critical to avoid large clusters. MNPs added dropwise to the PMAO-PEG polymer solution result in an individual or quasi-individual coating showing wider AC hysteresis loops.

Thereby, thanks to AC magnetometry technique an optimization of the coating protocol is achieved, attaining individually or quasi-individually coated F-MNP formulations.

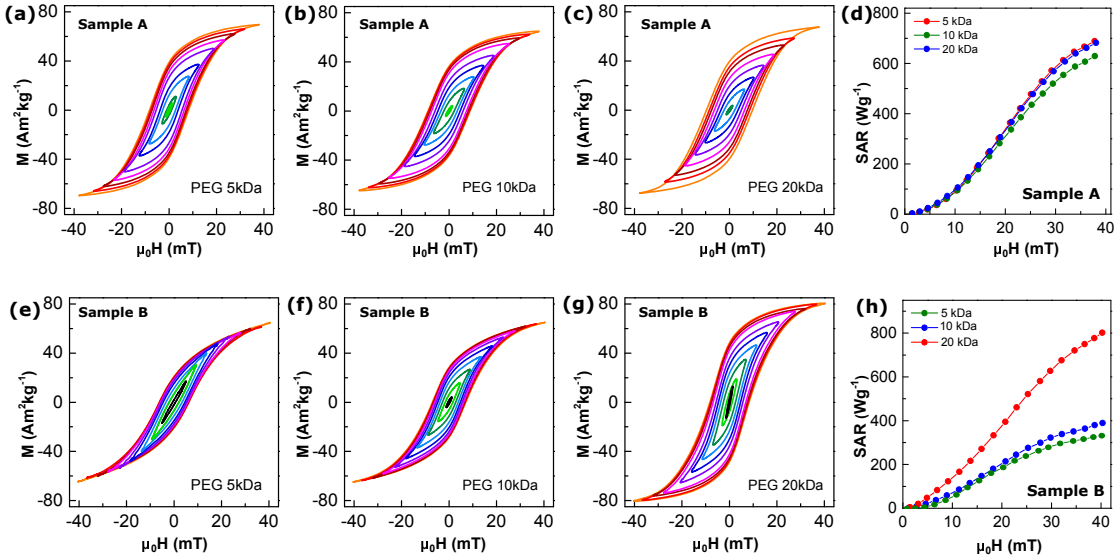

FIGURE 3.8: AC hysteresis loops of sample A (a) PEG 5kDa (b) PEG 10kDa (c) PEG20kDa and sample B (e) PEG 5kDa (f) PEG 10kDa (g) PEG 510Da. *SAR* versus magnetic field curve of (d) sample A corresponding to (a)-(c) and (h) sample B corresponding to (e)-(f).

On the other hand, in order to understand how the molecular weight of the PEG copolymer affects the heating performance of the systems, AC hysteresis loops and the corresponding *SAR* versus magnetic field curve of sample A and sample B coated with three copolymers of different molecular weights (5, 10 and 20 kDa) are obtained following the optimazed protocol (see Figure 3.8). From the displayed data it can be deduced that

AC hysteresis loops and *SAR* versus magnetic field curves of sample A don't reveal a significant difference among the three PEGs (see Figure 3.8 (a)-(c)). However, sample B does not turn out equally successful with PEG of different molecular weights (see Figure 3.8 (e)-(g)). The tilting of the AC hysteresis loops clearly reflects the influence of increasing interparticle interactions when the coating intensity is reduced. This behavior can also be observed in *SAR* vs magnetic field curve: 20 kDa PEG shows *SAR* values of 800 Wg^{-1} at maximum field which diminishes to 350 Wg^{-1} and 300 Wg^{-1} with 10 kDa and 5 kDa PEG, respectively. Thus, when the size of the F-MNPs increases, PEG with higher molecular weight are necessary to keep magnetic cores far enough and prevent particle agglomerations.

In summary, AC magnetometry enables to develop a new quasi-individual coating protocol, adjusted to different MNP sizes, which avoids MNP agglomerations. It is shown that larger MNPs require longer PEG molecules (20 kDa) to keep the magnetic particles far enough to each other.

Although, *SAR* vs magnetic field curve has a tendency of saturation at maximum available magnetic field, the saturation regime is outside the working span of the AC magnetometer employed in the measurements. This behavior is also observed in the works analyzed in the previous sections. As mentioned before, an unsaturated *SAR(H)* curves provides less accurate effective anisotropy value from simulations, among others.

3.4 Conclusions

As it has been demonstrated, *SAR* measurements over a wide AMF amplitude and frequency range provides critical information to design MNPs with high *SAR* values. One important limitation of the current AC magnetometers is the maximum available AC magnetic field intensity. Very often, these magnetic fields are in fact unable to approach magnetic saturation in most samples, particularly, when magnetic anisotropy turns to be significant (as it is common for the most beneficial MNPs), and dipolar interactions play an important role [22, 23]. This issue can be easily detected in the works presented in this chapter: Although most of the *SAR(H)* curves showed a tendency to saturation at the highest magnetic field, the saturation region is outside the experimental limits.

Minor hysteresis loops measurements limited to magnetic fields far below saturation always provide incomplete information about the magnetization dynamical properties. In consequence, the powerful set of theoretical models developed in recent years cannot be properly checked, so reducing our understanding of the factors that improve or degrade the heating performance of MNPs. Additionally, obtaining major hysteresis loops is the only way of calibrating the magnetic moment with some level of confidence. Thus, the goal of Chapter 4 is to develop a high field intensity AC magnetometer that works in a wide magnetic hyperthermia frequency range.

In recent years, an increasing number of works have been published analyzing the MNPs properties that really influence their heating performance. However, the possible physical effects caused by magnetic fields, such as chain formation or mechanical rotation of MNPs are in many cases overlooked. Consequently, it is unclear if some high SAR values reported in the literature [24, 25] rely entirely on MNP properties (as the composition, size or shape) or maybe on the way in which these particles are assembled together in a liquid. As it has been seen in the previous works, arrangements' effect can be easily detected from dynamic hysteresis loops. So far, this behavior is analyzed by comparing the AC hysteresis loops of liquid and agar MNPs solutions. However, an easier way to eliminate these mechanical effects is to perform measurements of the sample above and below the freezing point of the dispersion medium, without the need of additional sample handling. With this purpose, the second objective of the following chapter is the incorporation of a temperature control system to the high field AC magnetometer that allows obtaining AC hysteresis loops in a wide range between 220 K to 380 K in a continuous way.

The reproducibility is a very important premise for obtaining accurate measurements in any experimental technique. In literature, no details are provided with respect to the reproducibility of the AC magnetometers. Moreover, the measurements presented by some authors show results with high standard deviation when using high magnetic fields [26]. The magnetic thermal effects originated by the self-heating of samples and pick-up coils during the hysteresis loop measurements are the main reason of the decrease of accuracy. One solution can be to extract the background signal for each field measurements in really short time intervals. However, in current devices the sample is introduced manually, so it is impossible to improve the accuracy using the approach mentioned before. With this goal, the third objective of the following chapter is the

automatization of the positioning of the sample in a short time lag using an automatic positioner system. Additionally, the temperature system mentioned in the second objective is going to be the key element to maintain the isothermal conditions during the measurements for decreasing magnetic thermal effects and consequently increasing the accuracy.

On the other hand, the improvement of the feedthrough is another important challenge to address in AC magnetometers [27, 28]. The minimization of the feedthrough signal is limited by the minimum achievable movement of the pick-up coil inside the main coil. To approach this challenge, the fourth objective of the following chapter is the study of different shift mechanisms to fine-tune the position of the pick-up coil.

Bibliography

[1] R. P. Tan, J. Carrey, and M. Respaud, "Magnetic hyperthermia properties of nanoparticles inside lysosomes using kinetic Monte Carlo simulations: Influence of key parameters and dipolar interactions, and evidence for strong spatial variation of heating power," *Physical Review B*, vol. 90, no. 21, p. 214421, 2014.

[2] Z. Nemati, J. Alonso, I. Rodrigo, R. Das, E. Garaio, J. García, I. Orue, M.-H. Phan, and H. Srikanth, "Improving the Heating Efficiency of Iron Oxide Nanoparticles by Tuning Their Shape and Size," *The Journal of Physical Chemistry C*, vol. 122, no. 4, pp. 2367–2381, 2018.

[3] E. Lima, T. E. Torres, L. M. Rossi, H. R. Rechenberg, T. S. Berquo, A. Ibarra, C. Marquina, M. R. Ibarra, and G. F. Goya, "Size dependence of the magnetic relaxation and specific power absorption in iron oxide nanoparticles," *Journal of Nanoparticle Research*, vol. 15, no. 5, p. 1654, 2013.

[4] I. Morales, R. Costo, N. Mille, G. B. Da Silva, J. Carrey, A. Hernando, and P. De la Presa, "High Frequency Hysteresis Losses on -Fe2O3 and Fe3O4: Susceptibility as a Magnetic Stamp for Chain Formation," *Nanomaterials*, vol. 8, no. 12, p. 970, 2018.

[5] J. M. Asensio, J. Marbaix, N. Mille, L.-M. Lacroix, K. Soulantica, P.-F. Fazzini, J. Carrey, and B. Chaudret, "To heat or not to heat: a study of the performances of iron carbide nanoparticles in magnetic heating," *Nanoscale*, vol. 11, no. 12, pp. 5402–5411, 2019.

[6] D. Cabrera, A. Coene, J. Leliaert, E. J. Artés-Ibáñez, L. Dupré, N. D. Telling, and F. J. Teran, "Dynamical Magnetic Response of Iron Oxide Nanoparticles Inside Live Cells," *ACS Nano*, vol. 12, no. 3, pp. 2741–2752, 2018.

[7] B. Sanz, M. P. Calatayud, E. De Biasi, E. Lima, M. V. Mansilla, R. D. Zysler, M. R. Ibarra, and G. F. Goya, "In Silico before In Vivo: how to Predict the Heating Efficiency of Magnetic Nanoparticles within the Intracellular Space," *Scientific Reports*, vol. 6, no. 1, p. 38733, 2016.

[8] R. Di Corato, A. Espinosa, L. Lartigue, M. Tharaud, S. Chat, T. Pellegrino, C. Ménager, F. Gazeau, and C. Wilhelm, "Magnetic hyperthermia efficiency in

the cellular environment for different nanoparticle designs," *Biomaterials*, vol. 35, no. 24, pp. 6400–6411, 2014.

[9] D. Gandia, L. Gandarias, I. Rodrigo, J. Robles-García, R. Das, E. Garaio, J. García, M.-H. Phan, H. Srikanth, I. Orue, J. Alonso, A. Muela, and M. L. Fdez-Gubieda, "Unlocking the Potential of Magnetotactic Bacteria as Magnetic Hyperthermia Agents," *Small*, vol. 15, no. 41, p. 1902626, 2019.

[10] I. Castellanos-Rubio, I. Rodrigo, R. Munshi, O. Arriortua, J. S. Garitaonandia, A. Martinez-Amesti, F. Plazaola, I. Orue, A. Pralle, and M. Insausti, "Outstanding heat loss *via* nano-octahedra above 20 nm in size: from wustite-rich nanoparticles to magnetite single-crystals," *Nanoscale*, vol. 11, no. 35, pp. 16635–16649, 2019.

[11] I. Castellanos-Rubio, I. Rodrigo, A. Olazagoitia-Garmendia, O. Arriortua, I. Gil de Muro, J. S. Garitaonandia, J. R. Bilbao, M. L. Fdez-Gubieda, F. Plazaola, I. Orue, A. Castellanos-Rubio, and M. Insausti, "Highly Reproducible Hyperthermia Response in Water, Agar, and Cellular Environment by Discretely PEGylated Magnetite Nanoparticles," *ACS Applied Materials & Interfaces*, vol. 12, no. 25, pp. 27917–27929, 2020.

[12] C. Martinez-Boubeta, K. Simeonidis, A. Makridis, M. Angelakeris, O. Iglesias, P. Guardia, A. Cabot, L. Yedra, S. Estradé, F. Peiró, Z. Saghi, P. A. Midgley, I. Conde-Leborán, D. Serantes, and D. Baldomir, "Learning from Nature to Improve the Heat Generation of Iron-Oxide Nanoparticles for Magnetic Hyperthermia Applications," *Scientific Reports*, vol. 3, no. 1, p. 1652, 2013.

[13] K. Simeonidis, M. P. Morales, M. Marciello, M. Angelakeris, P. de la Presa, A. Lazaro-Carrillo, A. Tabero, A. Villanueva, O. Chubykalo-Fesenko, and D. Serantes, "In-situ particles reorientation during magnetic hyperthermia application: Shape matters twice," *Scientific Reports*, vol. 6, no. 1, p. 38382, 2016.

[14] D. Serantes, K. Simeonidis, M. Angelakeris, O. Chubykalo-Fesenko, M. Marciello, M. d. P. Morales, D. Baldomir, and C. Martinez-Boubeta, "Multiplying Magnetic Hyperthermia Response by Nanoparticle Assembling," *The Journal of Physical Chemistry C*, vol. 118, no. 11, pp. 5927–5934, 2014.

[15] A. Muela, D. Muñoz, R. Martín-Rodríguez, I. Orue, E. Garaio, A. Abad Díaz de Cerio, J. Alonso, J. García, and M. L. Fdez-Gubieda, "Optimal Parameters for

Hyperthermia Treatment Using Biomineralized Magnetite Nanoparticles: Theoretical and Experimental Approach," *The Journal of Physical Chemistry C*, vol. 120, no. 42, pp. 24437–24448, 2016.

[16] G. F. Goya, E. Lima, A. D. Arelaro, T. Torres, H. R. Rechenberg, L. Rossi, C. Marquina, and M. R. Ibarra, "Magnetic Hyperthermia With Fe_3O_4 Nanoparticles: The Influence of Particle Size on Energy Absorption," *IEEE Transactions on Magnetics*, vol. 44, no. 11, pp. 4444–4447, 2008.

[17] K. D. Bakoglidis, K. Simeonidis, D. Sakellari, G. Stefanou, and M. Angelakeris, "Size-Dependent Mechanisms in AC Magnetic Hyperthermia Response of Iron-Oxide Nanoparticles," *IEEE Transactions on Magnetics*, vol. 48, no. 4, pp. 1320–1323, 2012.

[18] B. Mehdaoui, A. Meffre, J. Carrey, S. Lachaize, L.-M. Lacroix, M. Gougeon, B. Chaudret, and M. Respaud, "Optimal Size of Nanoparticles for Magnetic Hyperthermia: A Combined Theoretical and Experimental Study," *Advanced Functional Materials*, vol. 21, no. 23, pp. 4573–4581, 2011.

[19] Y. Lv, Y. Yang, J. Fang, H. Zhang, E. Peng, X. Liu, W. Xiao, and J. Ding, "Size dependent magnetic hyperthermia of octahedral Fe3O4 nanoparticles," *RSC Advances*, vol. 5, no. 94, pp. 76764–76771, 2015.

[20] N. A. Usov and S. E. Peschany, "Theoretical hysteresis loops for single-domain particles with cubic anisotropy," *Journal of Magnetism and Magnetic Materials*, vol. 174, no. 3, pp. 247–260, 1997.

[21] A. Aharoni, *Introduction to the Theory of Ferromagnetism*. Clarendon Press, 2000.

[22] H. Kobayashi, K. Ueda, A. Tomitaka, T. Yamada, and Y. Takemura, "Self-Heating Property of Magnetite Nanoparticles Dispersed in Solution," *IEEE Transactions on Magnetics*, vol. 47, no. 10, pp. 4151–4154, 2011.

[23] M. Veverka, P. Veverka, O. Kaman, A. Lančok, K. Závěta, E. Pollert, K. Knížek, J. Boháček, M. Beneš, P. Kašpar, E. Duguet, and S. Vasseur, "Magnetic heating by cobalt ferrite nanoparticles," *Nanotechnology*, vol. 18, no. 34, p. 345704, 2007.

[24] J.-H. Lee, J.-t. Jang, J.-s. Choi, S. H. Moon, S.-h. Noh, J.-w. Kim, J.-G. Kim, I.-S. Kim, K. I. Park, and J. Cheon, "Exchange-coupled magnetic nanoparticles for efficient heat induction," *Nature Nanotechnology*, vol. 6, no. 7, pp. 418–422, 2011.

[25] J.-P. Fortin, C. Wilhelm, J. Servais, C. Ménager, J.-C. Bacri, and F. Gazeau, "Size-Sorted Anionic Iron Oxide Nanomagnets as Colloidal Mediators for Magnetic Hyperthermia," *Journal of the American Chemical Society*, vol. 129, no. 9, pp. 2628–2635, 2007.

[26] P. Lenox, L. K. Plummer, P. Paul, J. E. Hutchison, A. Jander, and P. Dhagat, "High-Frequency and High-Field Hysteresis Loop Tracer for Magnetic Nanoparticle Characterization," *IEEE Magnetics Letters*, vol. 9, pp. 1–5, 2018.

[27] N. Garraud, R. Dhavalikar, L. Maldonado-Camargo, D. P. Arnold, and C. Rinaldi, "Design and validation of magnetic particle spectrometer for characterization of magnetic nanoparticle relaxation dynamics," *AIP Advances*, vol. 7, no. 5, p. 056730, 2017.

[28] Z. W. Tay, P. W. Goodwill, D. W. Hensley, L. A. Taylor, B. Zheng, and S. M. Conolly, "A High-Throughput, Arbitrary-Waveform, MPI Spectrometer and Relaxometer for Comprehensive Magnetic Particle Optimization and Characterization," *Scientific Reports*, vol. 6, no. 1, p. 34180, 2016.

Chapter 4

Design and implementation of a high field, high frequency and temperature adjustable AC magnetometer

Taking into account the limitations of the current AC magnetometers, we have developed a versatile AC magnetometer able to work in a large range of frequencies (50 kHz - 1MHz) that are relevant for magnetic hyperthermia and capable of applying remarkably higher field intensities that those existing so far. Additionally, the instrument incorporates a variable temperature device to measure AC hysteresis loops in a continuous temperature range between 220 K and 380 K [1].

In this chapter we present a complete theoretical and experimental description of the developed device. Before getting in the design process of each component a brief overview of the system is presented (see Figures 4.1 and 4.2). The AC magnetometer consists on a solenoid coil (*main coil*) that generates a homogeneous AMF within a volume inside the coil in which the sample is placed [2, 3]. The main coil is part of a variable parallel *LCC resonant circuit* that generates magnetic fields at thirteen different frequencies in the range 50 kHz - 1 MHz with large field intensity: up to 90 mT in the low frequency side and up to 35 mT in the high frequency side. The AC sinusoidal signal to excite the LCC resonant circuit is produced by a *signal generator-oscilloscope*

(KEYSIGHT DSOX3024T) and amplified by a linear *power amplifier* (Model Electronics and Innovation 1140LA) of 1 kW maximum power. The excitation magnetic field generated by the main coil is measured with an electrically separated coil, called the *control coil*. The dynamic magnetization detector system, which is integrated inside the main coil consists in two oppositely wound *pick-up* coils. The position of the pick-up coils inside the main coil is adjusted using a *motorized xyz translation stage* to minimize the feedthrough signal. A complementary *motorized z axis stage* translates the sample inside each pick-up coil. For measuring the MNP magnetic response, a small polycarbonate cylinder container of 100 μl of capacity, 11 mm long and 4.9 mm wide is used as *sample holder*. The induced signal of the control coil and pick-up coils are recorded simultaneously by an *oscilloscope* (KEYSIGHT DSOX3024T). Additionally, the instrument incorporates a variable *temperature system* to control the temperature of the sample container during the measurements in a continuous range between 220 K and 380 K. Finally, all the measurement procedure, from the control of the instruments to the data processing, is automated using a home-made program under *Labview software* from National Instruments.

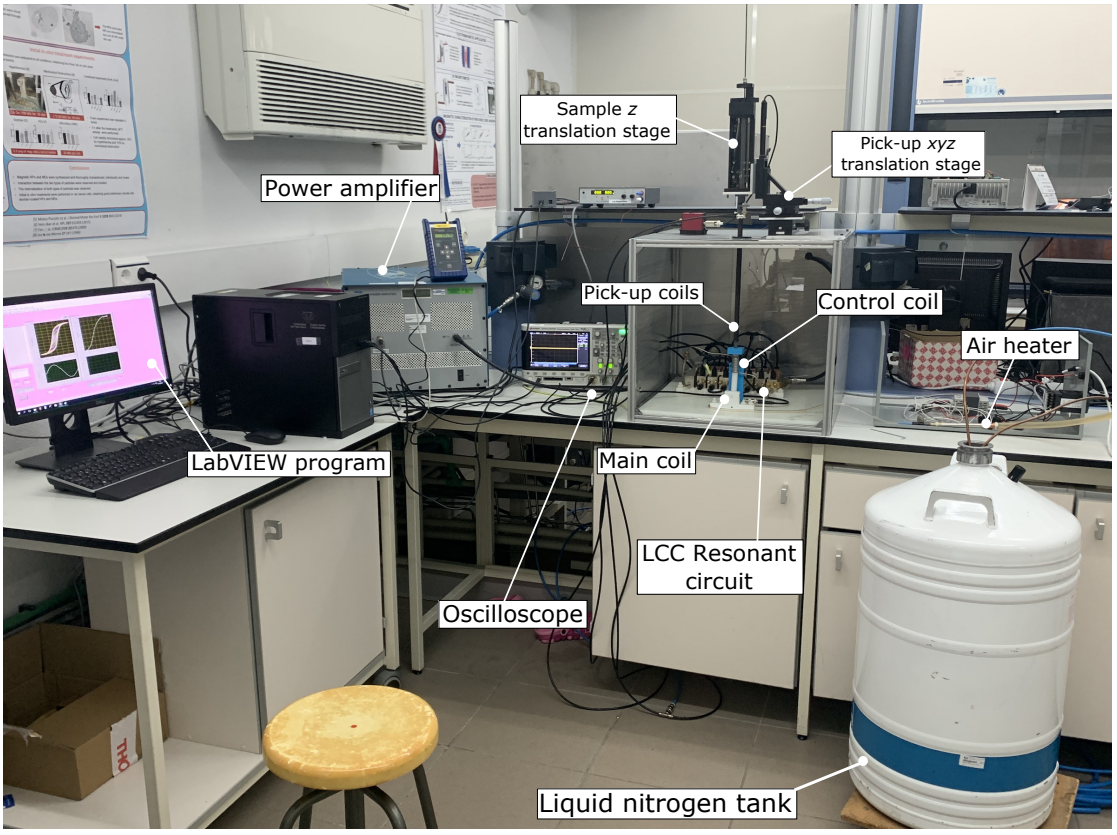

FIGURE 4.1: Picture of the whole AC magnetometer system developed in this thesis. Each instrument used in the AC magnetometer is explained in the text.

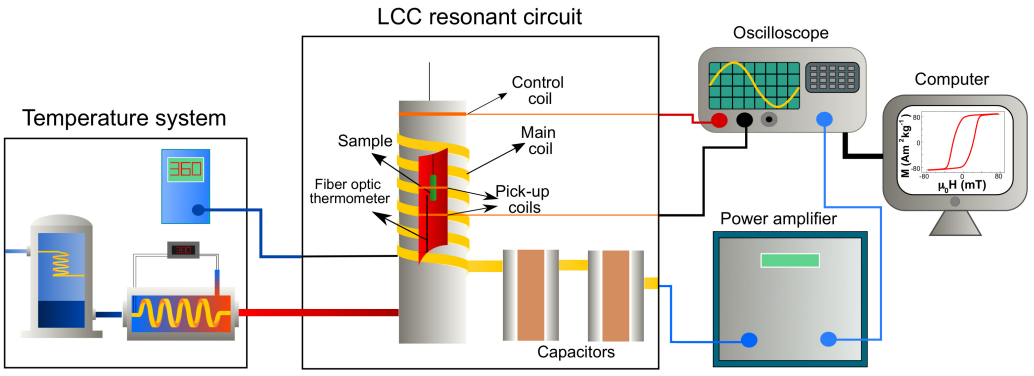

FIGURE 4.2: Detailed scheme of the AC magnetometer system. This picture is a guide to follow the descriptions presented in sections 4.1, 4.2 and 4.3.

4.1 Alternating magnetic field generator

4.1.1 Main coil

The main coil to generate the magnetic field consists of a copper pipe formed around a thermoplastic cylinder. Water is circulated through the copper pipe with a chiller that keeps the conductor temperature constant.

It is obvious that the same amount of input power can generate larger magnetic fields in smaller volumes. Therefore, the first step for designing a high field main coil is to reduce all its dimensions up to a fair use volume limit. This volume is constrained by several factors: (1) The sample holder size used in the experiments, (2) the sensitivity of the pick-up coil that should be located within the working area, (3) the dimensions of the conductor material which is used to fabricate the wounding coil, (4) the space between the sample holder and pick-up coils for allowing the flowing air to control the temperature of the sample and (5) the homogeneity requirements over the pick-up coil's length (less than 3.5%). For this reason, a good design of the inductor coil needs to maximize its efficiency at the frequencies employed in the hyperthermia experiments.

If the coil has not ferromagnetic components, the magnetic field generated by the coil is proportional to the AC electrical current:

$$H_{app}(\vec{r}) = \Pi(\vec{r}) I_{AC} \tag{4.1}$$

where $\Pi(\vec{r})$ is a position dependent geometrical factor, I_{AC} is the current that flows along the coil and $H_{app}(\vec{r})$ the magnetic field. On the other hand, the power dissipated by the coil is given by:

$$P = \frac{1}{2} R I_{AC}^2 = \frac{1}{2} R \frac{H_{app}^2}{\Pi(\vec{r})^2} \tag{4.2}$$

where P is the available power and R the equivalent series resistance of the coil (see Figure 2.6).

The maximum applicable magnetic field for a certain P becomes:

$$H_{max} = \sqrt{\frac{2\Pi^2}{R}} \sqrt{P} \tag{4.3}$$

Therefore, in order to build energetically efficient electromagnetic applicators, the ratio given by $\sqrt{2\Pi^2/R}$ should be maximized. Thus, we define a parameter, what we call efficiency, E_f, which depends on coil's geometry.

$$E_f = \sqrt{\frac{2\Pi^2}{R}} \tag{4.4}$$

Since the sample is placed at the position where the magnetic field is maximum, the proportional constant $\Pi(\vec{r})$ should be calculated at this point. Note that $\Pi(\vec{r})$ and the resistance R are not actually independent variables: coil diameter and number of turns affect the total resistance of the coil. However, for a given geometrical factor, R becomes critically enhanced at high frequencies due to the skin and proximity effects.

The skin effect is the tendency of an AC electric current to flow mainly near the surface of the conductor, thus reducing the effective cross section of the conductor and causing the effective resistance to increase. The so-called skin depth marks the level under the outer surface below which the electrical current is pushed out, which is given by Equation 4.5:

$$\delta = \sqrt{\frac{1}{f \pi \mu \sigma}} \tag{4.5}$$

where f is the frequency of electromagnetic waves and σ and μ are the conductivity and permeability of the material, respectively. The electromagnetic interaction between nearby conductors prompts one additional constraint to the current flowing through them that is usually called proximity effect. This phenomenon can be particularly significant within closely wound wires, such as those of the inductor coil used in this case.

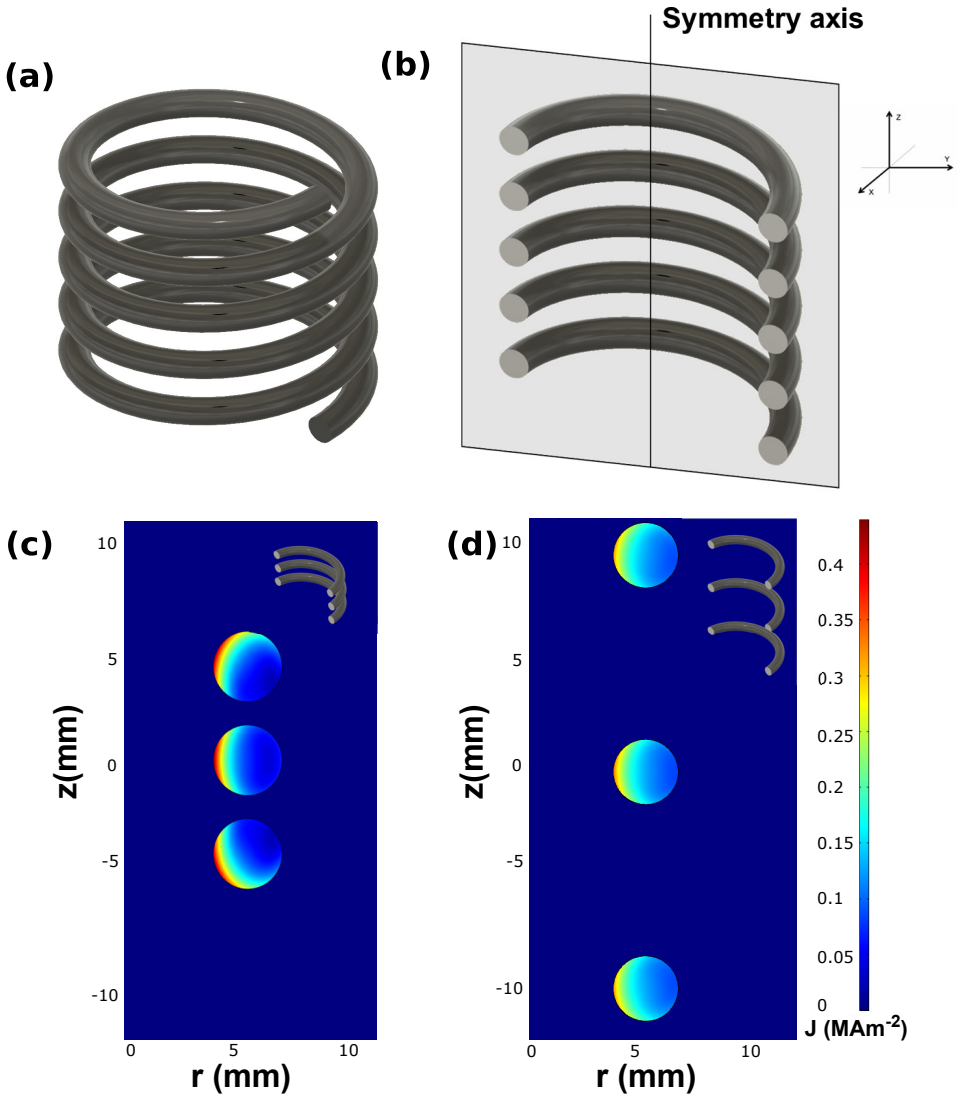

FIGURE 4.3: (a) Solenoid coil (b) Sliced plane of the solenoid coil. Spatial distribution of the current density in the cross section of three-turn solenoid with: (c) 5 mm turn pitch and (d) 10 mm turn pitch calculated by Finite Element Method (FEM), when 1A intensity and 10 kHz frequency circulates across the coil.

Figure 4.3 illustrates the proximity effect by comparing two identical three-turn coils with 5 mm and 10 mm turn pitch. As can be seen in the Figure 4.3 (c) and (d) the

current density is highly constrained to smaller regions when turns of the coil are closer to each other.

It should be noted that the main limitation of using solid copper pipes lies in the effective resistance of the coil: increasing the frequency above certain limits decreases quite fast the efficiency and therefore the maximum achievable AC field amplitude.

In our design a 3 mm copper pipe, wound to form a 12 mm diameter and 41 mm length coil has been fixed to fulfil the previously explained minimum fair volume limitations. The number of turns and the number of winding layers have been chosen to maximize the efficiency E_f. For it, Finite Element Method (FEM) simulations have been carried out using COMSOL Multiphysics software.

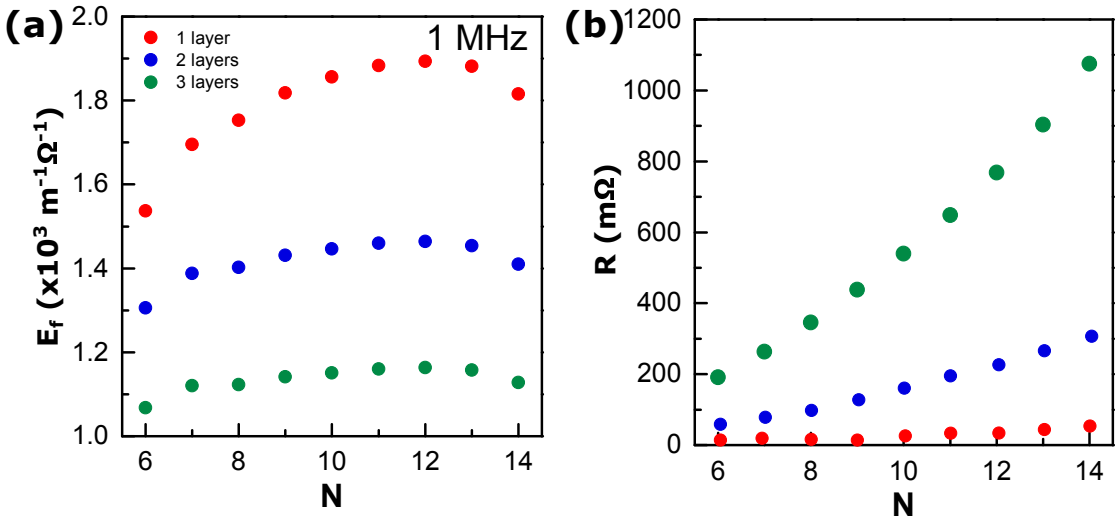

FIGURE 4.4: (a) Energy efficiency as a function of the number of turns, N, calculated by FEM for 1, 2 and 3 winding layers coils. The simulations are performed supplying the coil with a 1 kW power amplifier and an AC current at 1 MHz frequency. (b) Equivalent resistance of the coil as function of the number of turns for 1, 2, and 3 winding layers.

Figure 4.4 (a) shows the energy efficiency of the coil versus the number of turns for the above mentioned coil's geometry, calculated by FEM. In the case of the coil of one winding layer, the curve shows a maximum at N=12 at 1 MHz.

In coils with multiple winding layers, the proximity effects (this time occurring also between conductors of consecutive layers) degrade further the efficiency. As shown in Figure 4.4 (a) the most efficient coil is the one with a single winding layer. The reason for this is that when stacking more windings, the equivalent series resistance increases faster than $\Pi(\vec{r})$ (see Equation 4.4) and thus the efficiency decreases.

The energy efficiency maximum is frequency dependent due to the skin and proximity effects. Figure 4.5 (a) shows the energy efficiency versus the number of turns for different frequencies for a coil with a diameter and length of 12 mm and 41 mm respectively and one winding layer. In the working frequency range of our AC magnetometer (50 kHz-1 MHz) the maximum is located at 12 turns. Note that in the limit of very small frequencies, the skin and proximity effects become negligible and the maximum efficiency shifts to the maximum number of turns that fits in the given length of the coil. Figure 4.5 (b) shows the energy efficiency versus number of turns at DC fields for coils with different winding layers. As it can be observed the most efficient coil is the one with the maximum number of winding layers, due to the absence of proximity and skin effects. So, increasing the number of turns per length and/or to build additional winding layers can be successful at lower frequencies but become inefficient at the hyperthermia frequencies.

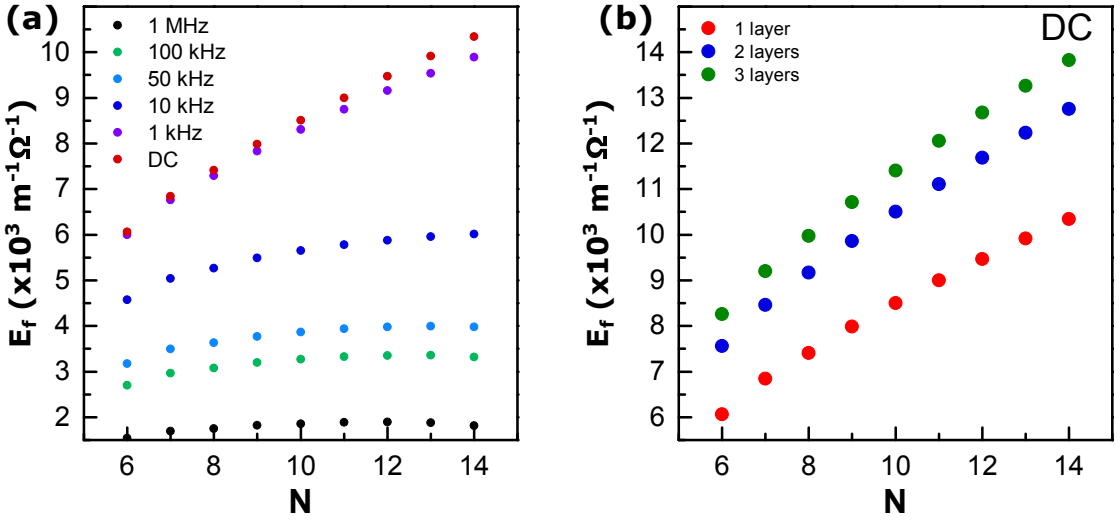

FIGURE 4.5: (a) Energy efficiency as a function of the number of turns for a coil with a diameter and length of 12 mm and 41 mm respectively, and one winding layer at different frequencies (b) Energy efficiency as a function of the number of turns for coils with one, two and three winding layers, for a DC current case.

As a result, the main coil that maximizes the energy efficiency in the whole working frequency range should have only one layer and 12 turns in a 41 mm length and 12 mm diameter coil. The main coil holder is mechanized using *delrin* material and the copper pipe is wound around it.

The electrical characterization of the main coil is performed using a network analyzer (Agilent E5071C). Figure 4.6(a) shows the real and imaginary parts of the impedance of the coil; as it can be observed the self-resonance frequency, f_r, is located at 20 MHz.

As the maximum working frequency of the system is 1 MHz, the main coil is reduced to an inductance L in series with a resistance R. Figure 4.6 (b) shows the resistance and reactance of the main coil at the magnetic hyperthermia working frequencies. Both resistance and reactance increase linearly with frequency. Thus, inductance, L, can be directly obtained from the data and its value is 1.25 μH.

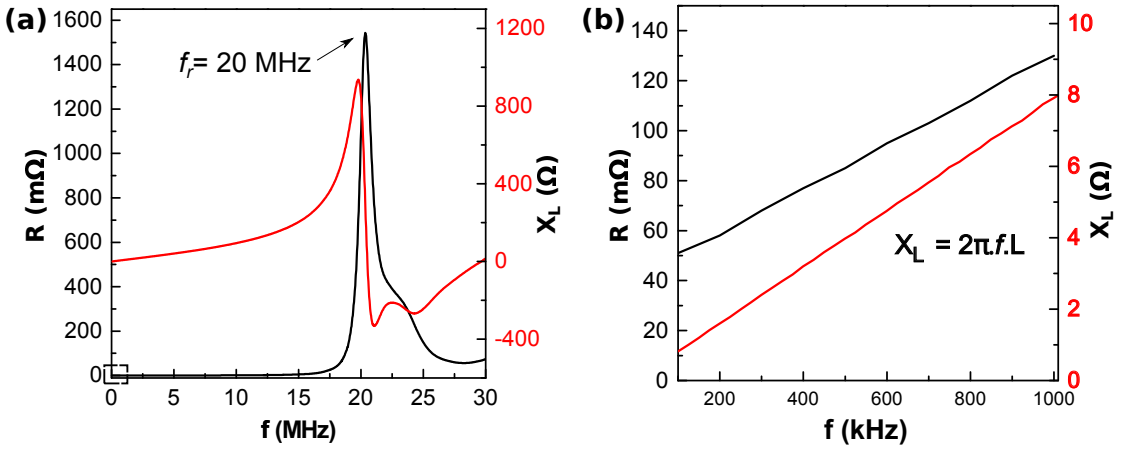

FIGURE 4.6: Measurements of the resistive (black lines) and reactive part (red curve) of the main coil at (a) frequencies between 10 kHz and 30 MHz and (b) working frequencies of the AC magnetometer. As the working frequency range of the system (50 kHz - 1MHz) is below the resonant frequency of the main coil (20 MHz), the equivalent electrical system is reduced to an inductance L in series with a resistence R. As shown in (b), the inductance can be calculate directly from the reactance of the main coil.

4.1.2 Resonant circuit

The signal generator (KEYSIGHT DSOX3024T) itself cannot provide the current and voltage needed to produce the required magnetic field for the AC hysteresis loops characterization. For this reason, the signal generator is connected in series with a power amplifier (Model Electronics and Innovation 1140LA with a real output impedance, R_s, of 50 Ω) that amplifies the voltage reference signal, and supplies the needed current to the main coil.

To match the main coil to the power amplifier, a variable capacitor matching is added in LC_1C_2 configuration (see Figure 4.7). For calculating the appropriate C_1 and C_2 values to work within the magnetic hyperthermia frequency range using the designed main coil, frequency-domain circuit simulations are carried out using Advanced Design System (ADS) software. The values of the inductance and resistance of the main coil used in the simulations are those measured before.

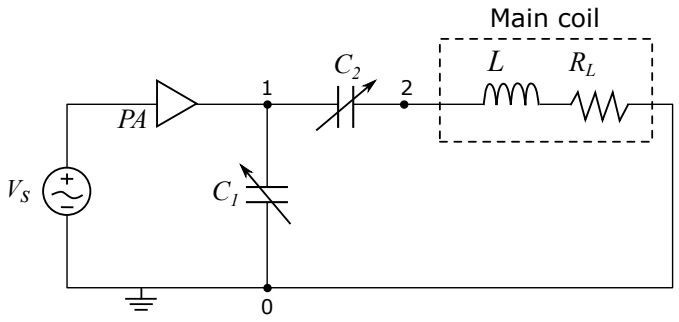

FIGURE 4.7: Equivalent electrical circuit of the AC magnetometer. V_S is the generator's voltage signal, PA the power amplifier, C_1 and C_2 are the variable capacitors and L and R_L the main coil's inductance and resistance.

The calculated values of C_1 and C_2 can be fixed by connecting different capacitors in different series or parallel configurations using mechanical switches. This connection technique permits to vary the working frequency rapidly and easily without any additional assemble. In our case, seven power capacitors of 170 nF (Models CPS 150/400 from Celem Power Capacitors) are used to implement the multifrequency AC Magnetometer. As an example, the configuration for setting 272 kHz is shown in Figure 4.8.

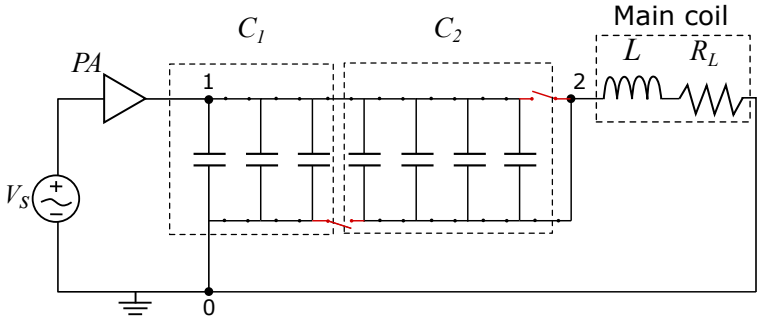

FIGURE 4.8: The switching configuration of the resonant circuit elements for setting 272 kHz working frequency. The values of C_1 and C_2 calculated from ADS simulations (510 nF and 680 nF, respectively) are obtained connecting the seven capacitors in the configuration shown.

Among all the possible pair of capacitor values (C_1, C_2), the ones that approximately fulfill the maximum power transfer condition ($P_{LC_1C_2}/P_s \sim 1$) between the power delivered to the resonant circuit, $P_{LC_1C_2}$, and the power that can be delivered by the amplifier, P_s, are selected using a network analyzer (Agilent E5071C) (see Appendix A). Each pair of capacitors value corresponds to a single frequency, that are the working frequencies of the system. Ten frequencies in the range 100 kHz-1 MHz are selected.

Alternatively, the resonant circuit can also work in three frequencies between 50 kHz and 100 kHz by replacing manually three capacitors of 170 nF by three of 2200 nF. However, the resonant circuit needs to be improved to work in these last frequencies under maximum power transfer conditions.

4.1.3 Magnetic field calibration

To measure accurately the AC hysteresis loops of the MNPs and the *SAR* it is crucial to have a well-known field amplitude at sample's position. Most commercial fluxmeters measuring AC magnetic fields at frequencies higher than 5 kHz are expensive and their dimensions do not fit in our designed prototype. Therefore, in order to characterize the magnetic field intensity generated by the main coil a home-made AC probe is built and calibrated. The AC probe consists of a two-turn circular coil with 8 mm diameter. The normal vector to the section of the AC probe is perpendicular to the *xy* plane of the main coil allowing us to determine the magnetic field along the *z* axis (see the reference system in Figure 4.3). All the parts of the AC probe are 3D printed (Form 3, FormLab) to avoid any distortion of the magnetic field.

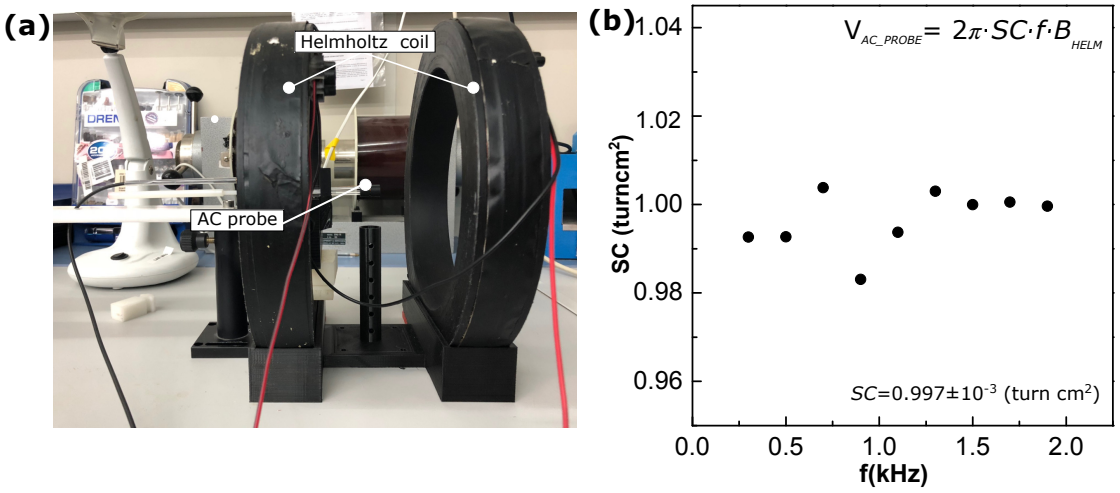

FIGURE 4.9: (a) The system employed for the calibration of the home-made AC probe, used to measure the magnetic field generated by the main coil. For the calibration, the voltage of the AC probe (placed in the geometrical center of a commercial Helmholtz coil) is recorded while an AC magnetic field is generated with the Helmholtz coil. From the resulting data and applying Faraday's law of induction the section constant, *SC*, is calculated. (b) The section constant as function of frequency.

For characterizing the magnetic field, the voltage induced in the AC probe, $V_{AC\ Probe}$, is measured and the Faraday's law of induction is applied:

$$V_{AC\ Probe} = 2\pi SCfB_{main\ coil} \tag{4.6}$$

where SC is the section constant of the AC probe, f the magnetic field frequency and $B_{main\ coil}$ the magnetic field generated by the main coil. In order to measure the magnetic field accurately SC of the AC probe is calibrated using a commercial Helmholtz coil that generates 2.371 mTA^{-1}. For the calibration experiments, the AC probe is placed in the geometrical center of the Helmholtz coil as it can be observed in Figure 4.9 (a) [4]. The calibration consists in generating an AC magnetic field in the Helmholtz coil, while the voltage induced in the AC probe is recorded for different frequencies. From the resulting data, the section constant, SC, of the AC probe is calculated (see Figure 4.9 (b)).

For the characterization of the magnetic field, the AC probe is moved along z axis of the main coil and measurements are taken in steps of about 3 mm. In each measurement, the voltage induced in the AC probe is monitored with an oscilloscope (KEYSIGHT DSOX3024T) and the magnetic field is calculated.

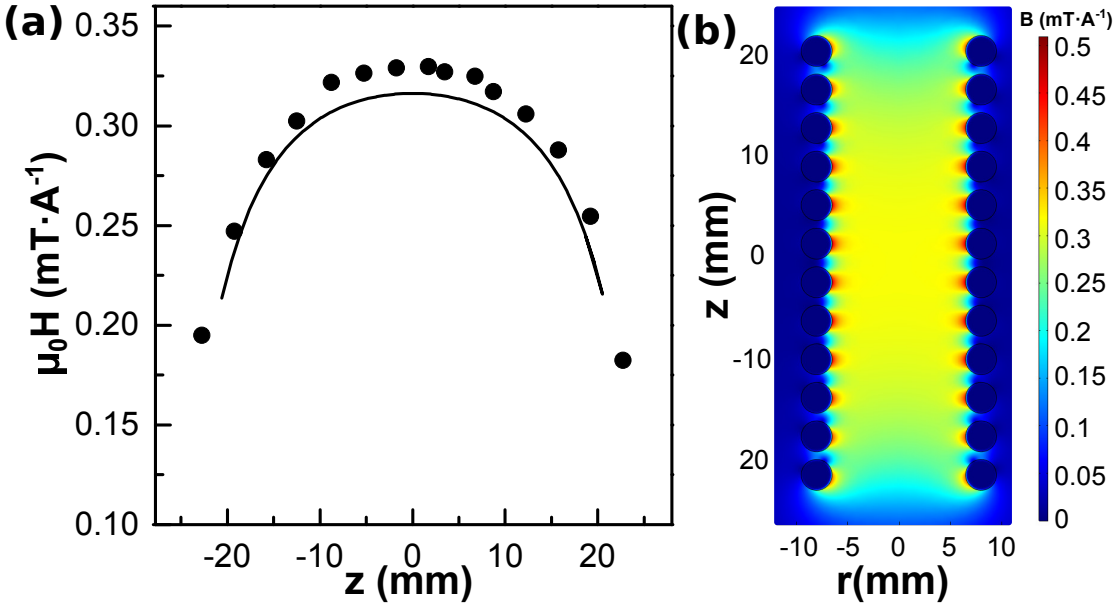

FIGURE 4.10: (a) The ratio of magnetic field intensity to current intensity in the z axis of the main coil measured experimentally (dots) and simulated by FEM (solid line) at 515 kHz. (b) Spatial distribution of the magnetic field simulated by FEM at 515 kHz and 1A.

The variation of the magnetic field intensity along the z axis of the working area (10 mm above and below the center of the coil) is less than 3.5 % as it can be observed in Figure 4.10 (a). The magnetic field in the z axis is simulated by FEM and compared with the experimental data. The measured value of the AMF intensity is 4 % bigger than the one predicted from simulations, which is an acceptable error. Figure 4.10 (b) shows the spatial distribution of the magnetic field simulated by FEM. In working volume, the field variation is less than 3.5%, what is a good value for magnetic hyperthermia experiments.

As important as the characterization of the magnetic field inside the main coil for an accurate measurement of the SAR and AC hysteresis loops it is the control of the magnetic field during the experiments. Our device incorporates an external coil, called control coil, that is electromagnetically coupled with the main coil. The control coil and the previously described AC probe, are placed outside and in the center of the main coil, respectively. Then, the relation between signals for both coils is measured using an oscilloscope (KEYSIGHT DSOX3024T) (see Figure 4.11). From this data the intensity of the magnetic field can be controlled during the measurement only by the external control coil.

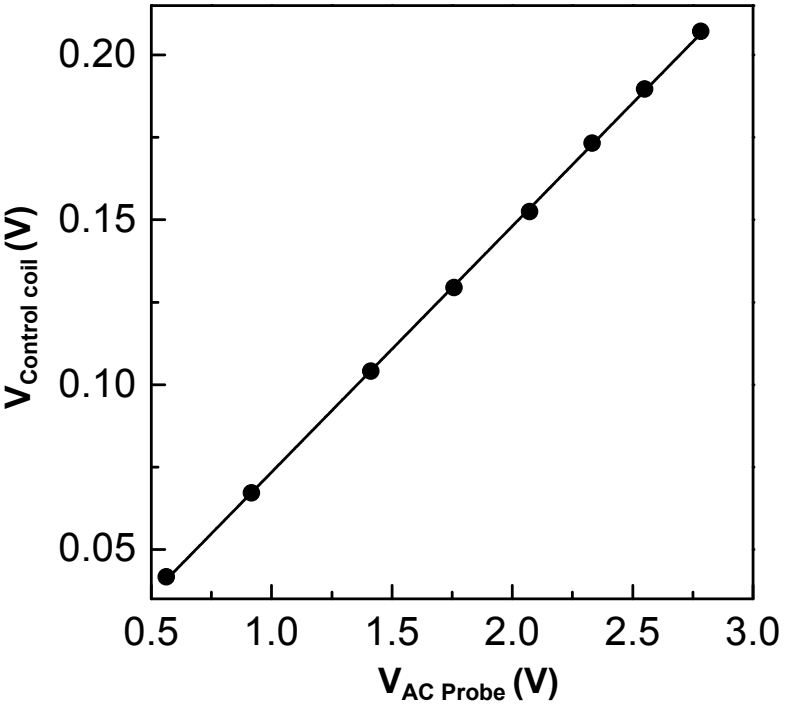

FIGURE 4.11: Control coil signal versus the signal induced in the AC probe. These measurements are obtained placing the control coil and the AC probe outside and in the center of the main coil, respectively. From this data, the magnetic field can be calculated during the AC hysteresis loop measurements by using only the control coil.

Finally, the maximum achievable magnetic field at each working frequency is measured using the control coil. As it can be observed in Figure 4.12, the maximum achievable magnetic field at 50 kHz is 90 mT and it decreases with frequency due to the increment of the equivalent electrical resistance with increasing frequency.

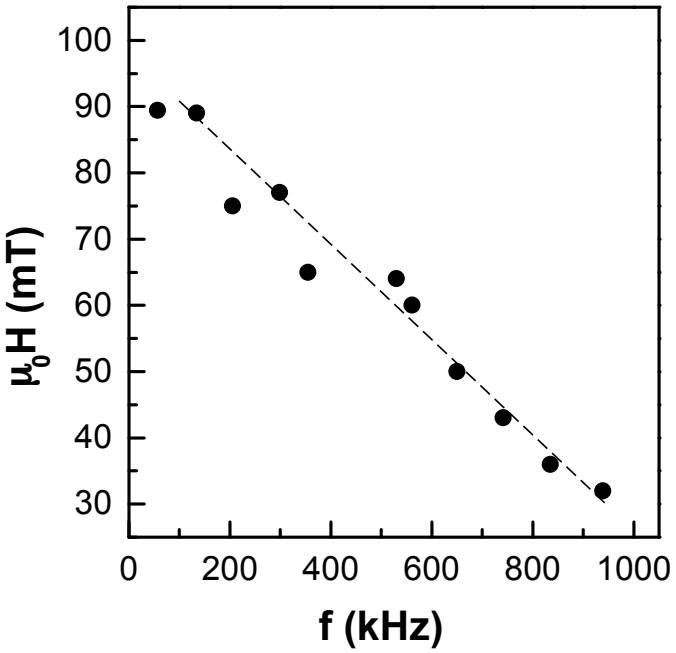

FIGURE 4.12: Maximum achievable magnetic field at each working frequency. The maximum magnetic field value decrease with frequency due to the increase of the resistance of the main coil with frequency (see Figure 4.6(b))

.

4.2 Temperature system

To change the temperature of the sample during the measurement, a cooling-heating circuit is added to the setup. Figure 4.13 shows the scheme of the temperature system.

An air flow stream is introduced inside the *delrin* cylinder located within the main coil. The temperature of the sample is measured with a non-resistible fiber optic thermometer (Model OTG MPK5 from OpSens), placed near the sample and inside the *delrin* cylinder in contact with the airflow. The incoming air flow can be heated up to the desired temperature with an air heater resistance to change the temperature of the sample (Air heater Model 8607198 from RS Pro). When low temperatures are required, the pre-heating temperature of the system can be lowered by the incoming air flow through a winding copper coil immersed in liquid nitrogen before reaching the

heater. The temperature of the out coming air flow close to the heater output is under a feedback Proportional Integral Derivative Controller (PID) temperature control (Model 3216 from Eurotherm) with a k type thermocouple sensor (Model K-M-1-3-25-1/4NPT-GS-1 from Omega). But in order to further keep the sample temperature as stable as possible a second feedback loop acts over the controller set point in response to changes of the fiber optic sensor located very close to the sample. Note that the sample always heats up during the AC application, so, isothermal conditions means in this case that the temperature of the air flow at the sample location must be kept constant during the experiment and being high enough to remove the extra heat induced by the AC field in the sample.

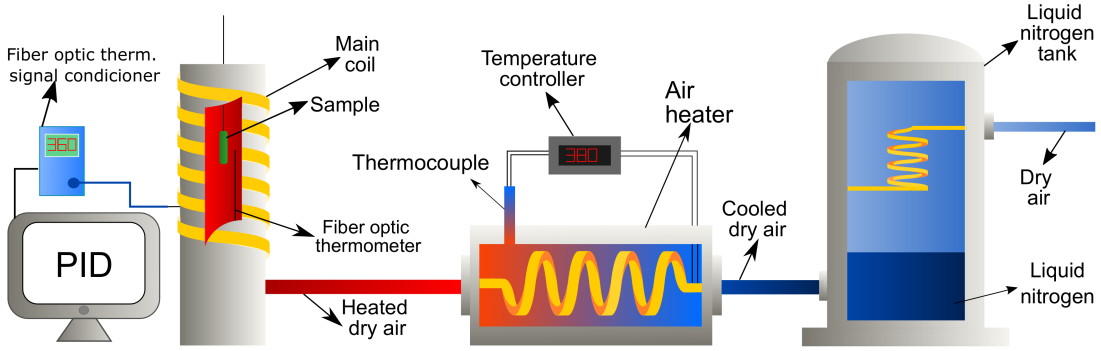

FIGURE 4.13: Scheme of the temperature system of the AC magnetometer. The role of each instrument is analyzed in Section 4.2.

4.3 Dynamic magnetization detector system

The dynamic magnetization detector system is composed of two identical oppositely wound pick-up coils connected in series. Each pick-up coils consists of 5 turns and they are separated by 10 mm. The pick-up coils are made of 36 AWG phosphor bronze wire and they are wound around a photopolymer resin cylinder in 8 mm of diameter manufactured with a 3D printer (Form 3, FormLab). The pick-up coil holder fits inside the main coil cylinder and it is hollowed to allow the flow of the air of the temperature system.

As it is explained in the Chapter 2 the two oppositely wound pick-up coils connected in series is a technique used to remove the undesirable excitation magnetic field induced signal in the pick-up coil surrounding the sample [5–8]. However, the cancellation of

the excitation signal cannot be perfect because of the small phase shift and geometry difference existing between pick-up coils and also due to field inhomogeneities inside the main coil.

4.3.1 Feedthrough

To reduce the remaining signal, called feedthrough, a pick-up coil shift mechanism is used. As it will be shown in set of figures 4.17, 4.18 and 4.19 the pick-up coil and its holder are stuck to a platform which is installed on a *xyz* translation stage (Thorlabs, PT3/M series). This stage is fitted with a micrometer that is able to shift the pick-up coils system in steps of 10 μm in 3-axis inside the main coil. This method permits a simultaneous feedback of the pick-up coils performance during the adjustment to choose the optimal position to minimize feedthrough. The use of the translation stage is key because the pick-up coils can be moved externally. The attenuation of the feedthrough of each pick-up coil set is calculated applying the Equation 4.7.

$$attenuation(dB) = 20\log\left(\frac{V_2}{V_1}\right) \tag{4.7}$$

where V_1 is the signal measured in the case of having an individual pick-up coil and V_2 by a set of two oppositely wound pick-up coils. As the two wound pick-up coils cannot be separated to measure each V_1, FEM simulations are carried out to obtain the V_1 value of each one of them. On the one hand, the V_2 signal in x, y and z axes is obtained following the steps explained below:

(**A**) The pick-up coil holder is placed in the geometrical center of the main coil using the *xyz* manual translator stage.

(**B**) The pick-up coil holder is moved in z axis in steps of 10 μm while V_2 signal is recorded in each position.

(**C**) The feedthrough attenuation in z axis is calculated applying Equation 4.7.

(**D**) The position of the minimum attenuation is obtained and the pick-up coil holder is fixed.

(**E**) Finally, the V_2 signal is measured in x and y axes in steps of 50 μm and the attenuation is calculated.

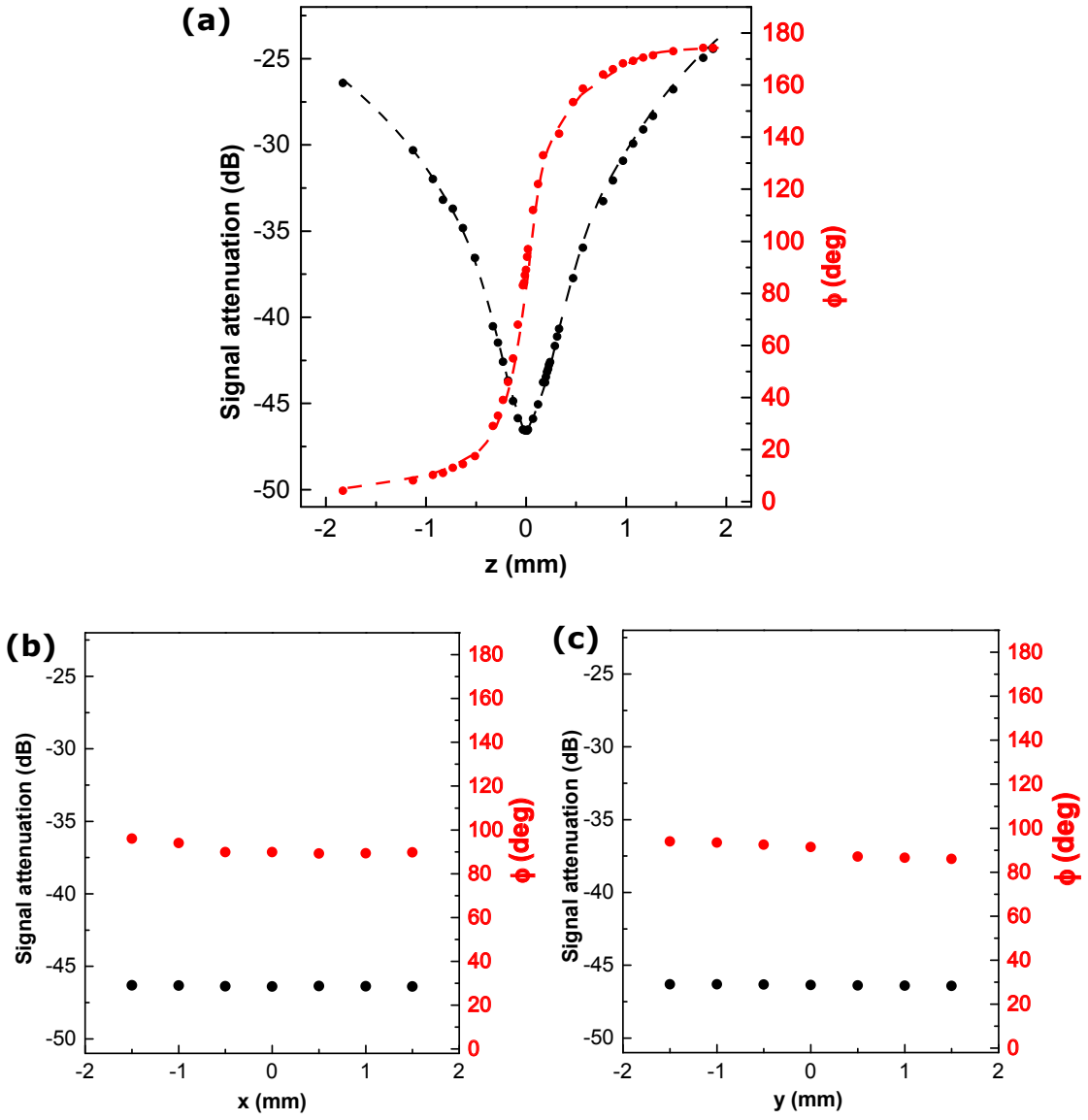

FIGURE 4.14: The black curve represents the feedthrough attenuation of the pick-up coils calculated by applying Equation 4.7, as function of the position in the axes (a) z, (b) x, and (c) y. The red curve shows the phase between the pick-up coil, V_2, and the control coil, $V_{control\ coil}$. As it can be observed at minimum feedthrough position the two signals are in quadrature.

Figure 4.14 shows the attenuation of the pick-up coils in x, y and z axes. As it can be seen in Figure 4.14 (a) the minimum attenuation value at 134 kHz is around -46 dB. It is worth mentioning that whereas the variation of the attenuation is 50 % when pick-up coil system is moved 2 mm along the z axis, it almost remains constant in the same position variation in x and y axes. Figure 4.14 also represents the phase

between V_2 and $V_{control\ coil}$. Note that at minimum attenuation position both signals are in quadrature.

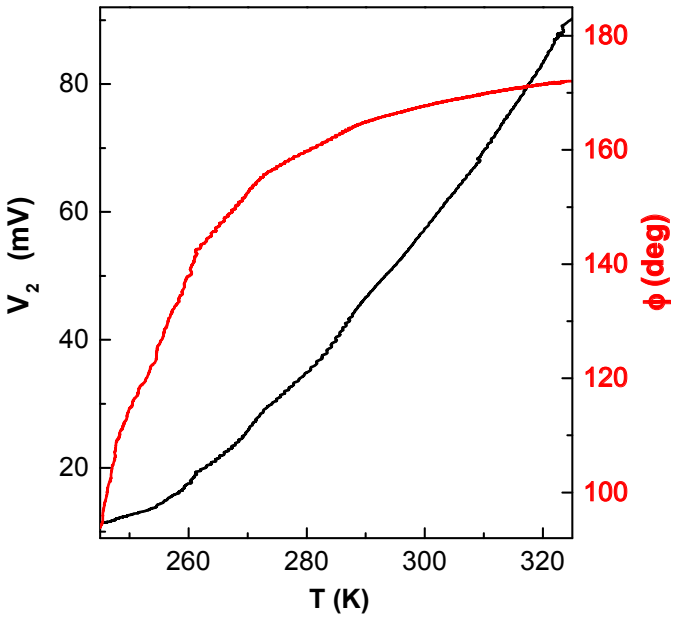

FIGURE 4.15: Voltage induced in the pick-up coil, V_2 (red line) and phase between V_2 and $V_{control\ coil}$ as function of temperature. The variation of V_2 with temperature influence the feedthrough, so for each temperature the minimum feedthourgh position needs to be fixed.

When varying the temperature of the air flow thermal effects emerging in the pick-up coils highly influence the value of the feedthrough (see Figure 4.15). Consequently, for measuring the dynamic signal of MNPs correctly the feedthrough has to be minimized at each temperature. To solve this issue, the micrometer of z axis of the *xyz* manual translation stage is replaced with a motorized actuator (Thorlabs, Z825B actuator control by KDC101 controller) that shifts the pick-up coil set in steps of 50 nm. This enables to find the minimum feedthrough accurately and automatically at each temperature.

Although the positioning of the pick-up coil inside the system using the *xyz* translation stage minimizes the feedthrough it is impossible to remove completely this undesired signal. In order to eliminate the remaining feedthrough signal, the following procedure is performed:

(**A**) The induced signal is measured in the lower pick-up coil ($V_{sample}^{lower\ pick-up}(t)$)

(**B**) The induced signal is measured in the upper pick-up coil ($V_{sample}^{upper\ pick-up}(t)$)

(**C**) The sample signal is extracted by averaging the vector subtraction of the sample signal measured with both pick-up coils:

$$V^{sample}(t) = (V_{sample}^{upper\ pick-up}(t) - V_{sample}^{lower\ pick-up}(t))\ /2$$

However, for removing the feedthrough, it is important to measure the signal induced in each pick-up coil for small time lags. With this aim, the sample is positioned in each pick-up coil using an additional motorized z axis stage controlled with an Arduino Uno SMD microcontroller (see Figure set 4.17, 4.19 and 4.18).

Finally, as previously done with the main coil, the pick-up coil system is electrically characterized using a network analyzer (Agilent E5071C). Figure 4.16 shows the real and imaginary parts of the impedance of the pick-up coils with a self-resonance frequency of 32.7 MHz.

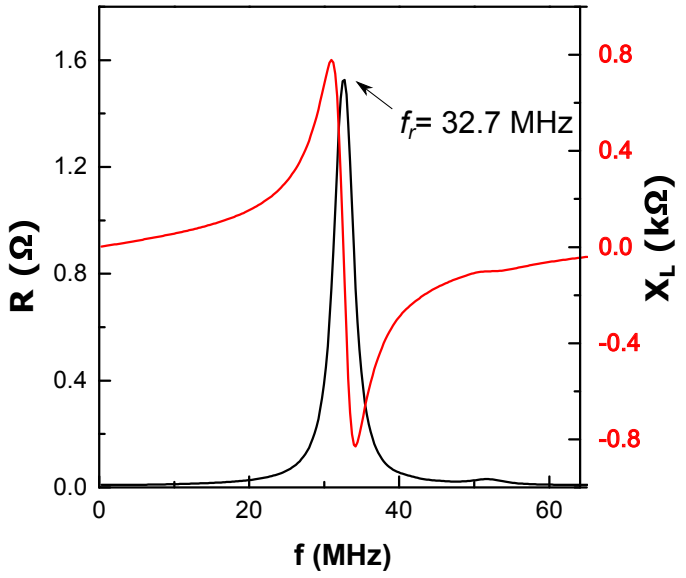

FIGURE 4.16: Measurements of the resistive (black curve) and reactive part (red curve) of the pick-up coil system in frequencies between 10 kHz and 70 MHz

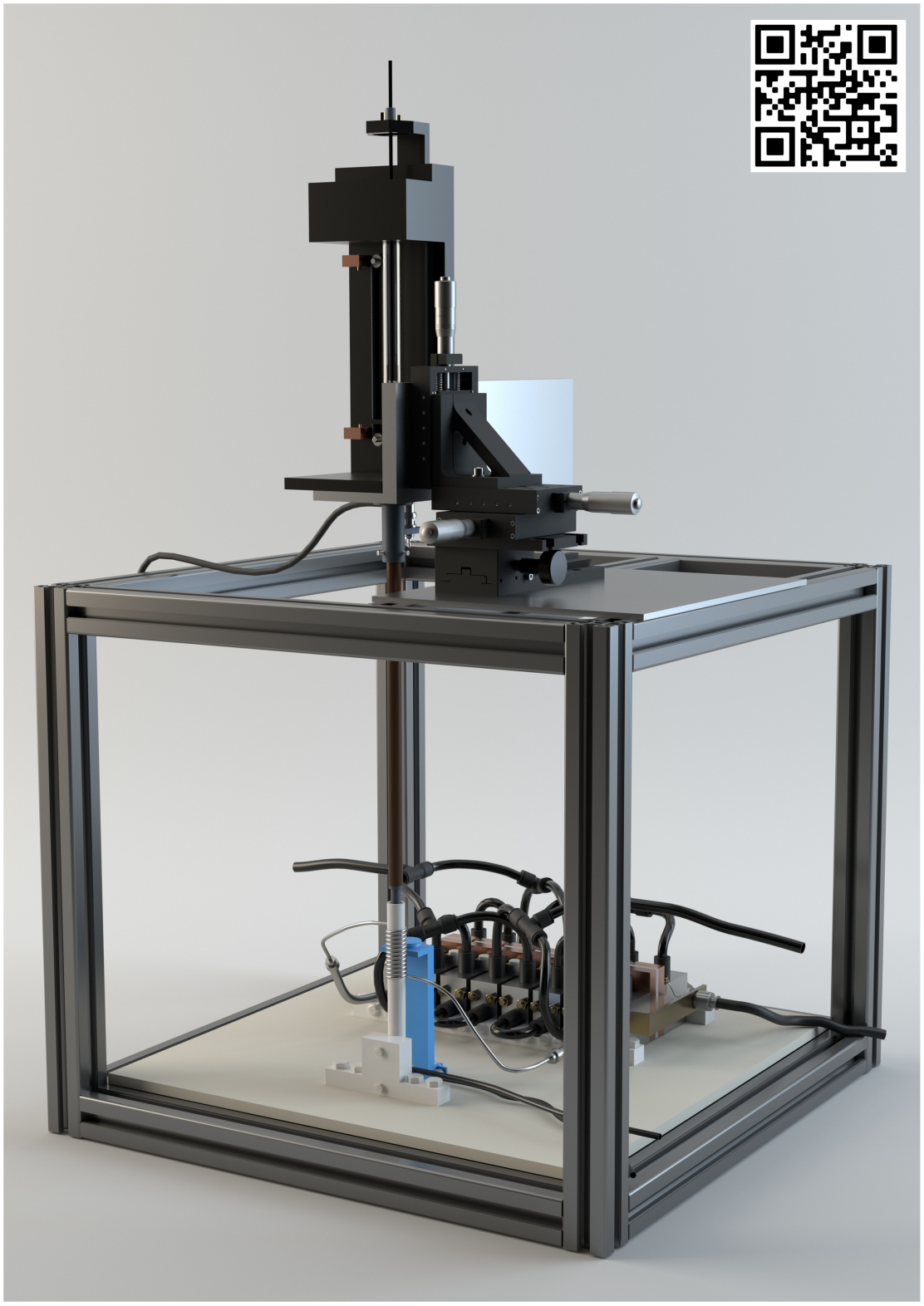

FIGURE 4.17: 3D model of the AC magnetometer designed using Autodesk Maya software. By scanning the QR code inside the picture a video animation of the AC magnetometer will be shown.

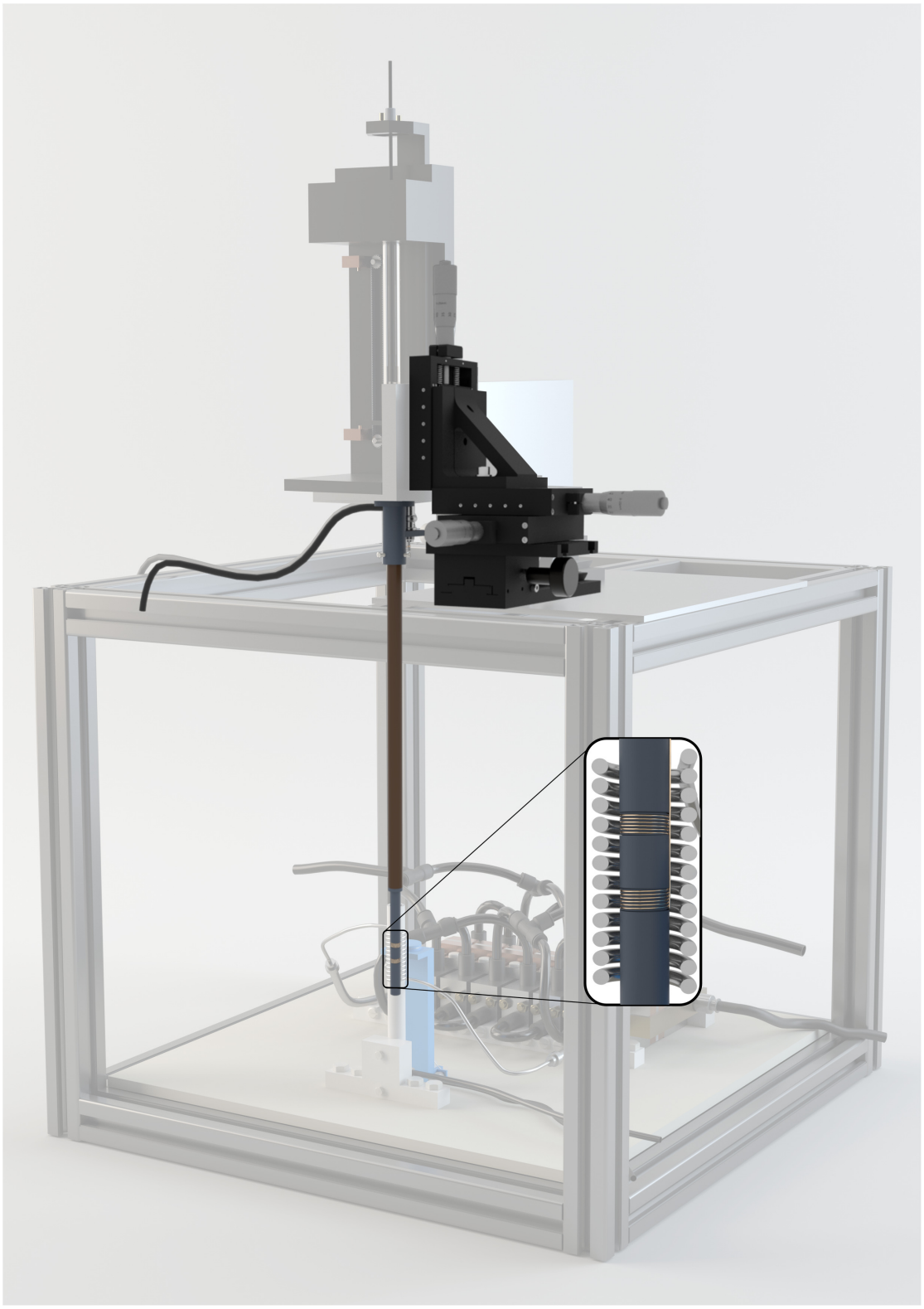

FIGURE 4.18: Pick-up coil set, pick-up coil holder and *xyz* translation stage used to shift pick-up coils inside the main coil in order to find the minimum feedthrough position. The pick-up coil holder is composed by a 3D printed part (gray tube) that is attached to a carbon fiber tube (brown tube).

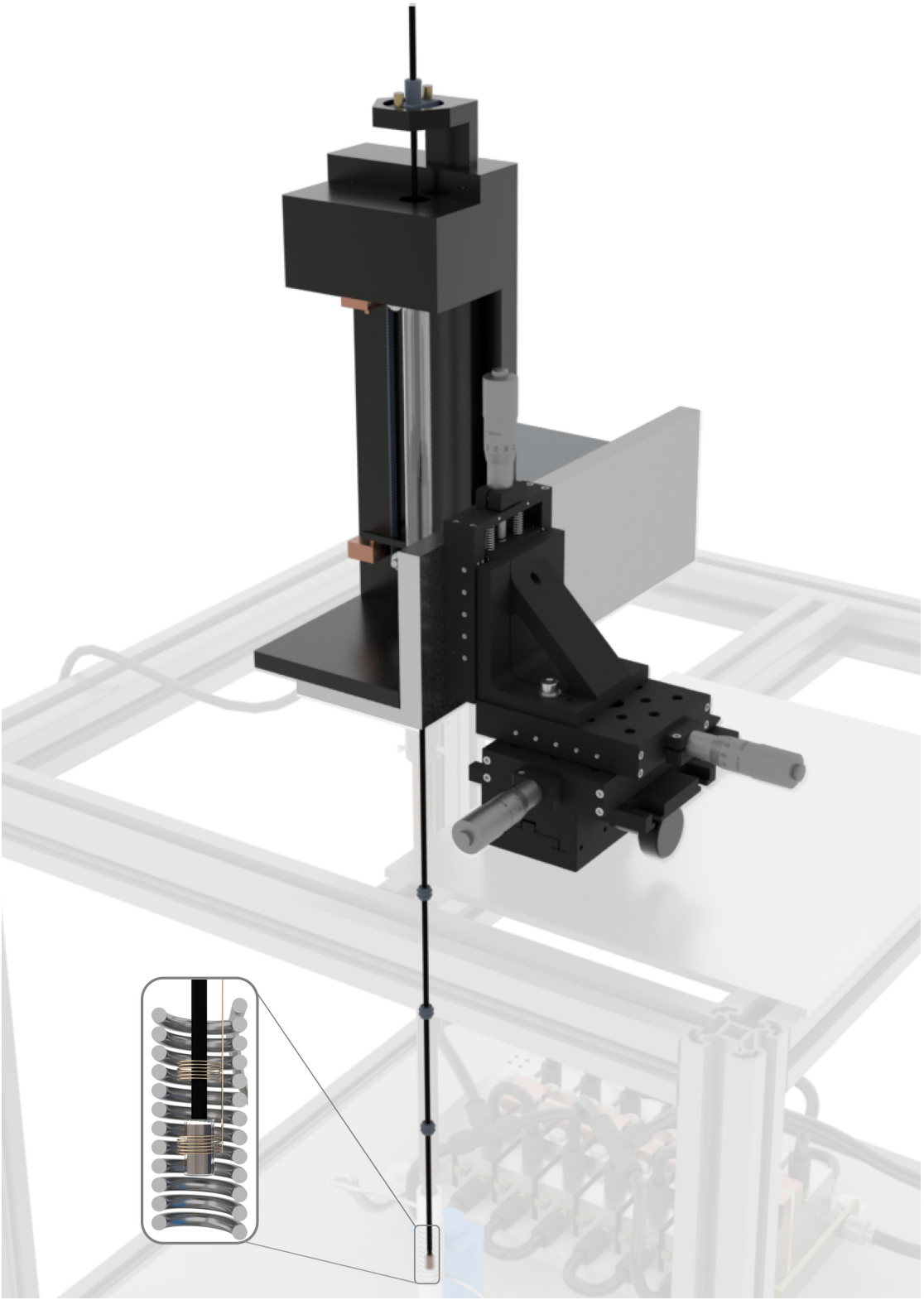

FIGURE 4.19: Sample holder and motorized translation stage used to locate the sample in the upper and lower pick-up coils. The sample holder is attached to a carbon fibre rod.

4.3.2 Magnetization calibration

The calibration of the magnetization in AC magnetometers is an import issue that is not deeply analyzed in literature. Some authors, as Garaio *at al.* [9], calibrated the magnetization by solving the Faraday's law of induction using FEM simulations. However, the analytical expression used in the simulations does not consider any depletion that may occur in the pick-up coils due to different phenomena such as deformation over time.

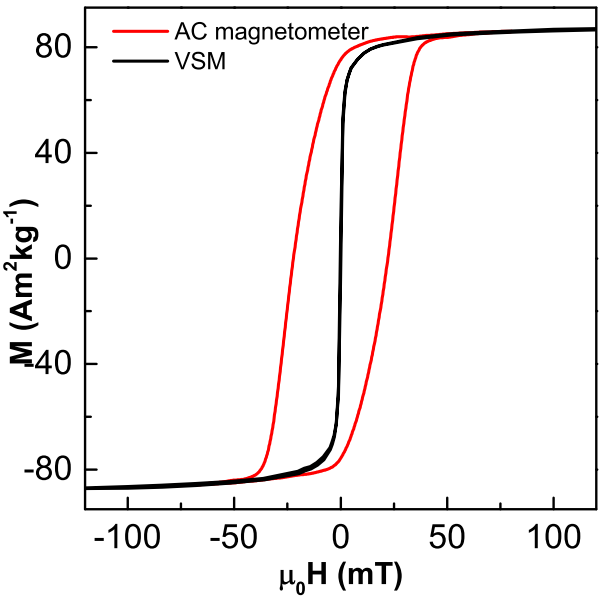

FIGURE 4.20: DC and AC hysteresis loops of the pattern sample used to calibrate the magnetization of the AC magnetometer.

Commonly, Vibrating Sample Magnetometers (VSM) are calibrated by using pattern samples. In this approach, the saturation magnetic moment of the pattern sample is known and the voltage induced in the detector coils is measured. From the obtained data, the calibration constant of the pick-up coils for a given sample holder dimension can be calculated.

For applying this calibration methodology in AC magnetometers they need to generate magnetic fields high enough to saturate the magnetic nanoparticles. Thus, the high field AC magnetometer developed in this Thesis becomes an important instrument for calibrating the magnetic moment with some level of confidence.

The magnetization of the AC magnetometer is calibrated using iron oxide magnetic nanoparticles dispersed in water. The DC hysteresis loop of the sample is recorded

in a well calibrated VSM saturating the magnetic nanoparticles. Then, the major AC hysteresis loop of the sample is measured in the built AC magnetometer applying a magnetic field of 90 mT and 134 kHz. Finally, the amplitude of the dynamic magnetization is scaled up to match the calibrated saturation magnetization measured with the VSM. From this data, the conversion factor to switch from the integrated pick-up voltage to magnetization units is calculated experimentally (see Figure 4.20).

4.4 Measurement protocol

A LabVIEW project is developed to automatize the AC hysteresis loop measurements. The built program controls the instruments used in the AC magnetometer (Oscilloscope, fiber optic thermometer, temperature controller, motorized actuator and Arduino Uno microcontroller) by RS 232, GPIBa and USB communication protocols and also processes all the data. Although the lower programming subroutines of the project can be complex, the final interface is user-friendly, which allows any researcher with some basic training to use it.

4.4.1 AC hysteresis loop measurements and SAR calculation

The followed step to measure AC hysteresis loops and calculate SAR values are outlined below:

1. Introduction of working parameters: The working parameters are inserted in the LabVIEW program: Maximum magnetic field intensity and frequency, number of measurements, temperature range, etc. and the desired working frequency is fixed by setting the suitable capacitor configuration (see Section 4.1.2).

2. Magnetic field generation: The magnetic field generated by the main coil is established using a closed-loop control system. First, the reference voltage, V_{ref}, is determined converting the introduced initial magnetic field into a voltage signal using the calibration constant calculated in Section 4.1.3. Then, a PID controller sets an output voltage, V_{gen}, to the signal generator that excites the main coil via the power amplifier. The control coil detects the magnetic field and outputs it as

a voltage signal $V_{control}$ that is recorded by means of an oscilloscope. This voltage is fed into the PID controller closing the loop. Finally, the measured control signal and reference signal are compared and the procedure is repeated increasing V_{gen} value until both signals converge. The value of V_{gen} for obtaining the desired maximum magnetic field is stored. To measure AC hysteresis loops at different magnetic fields an array of V_{gen} values is created taking into account the number of measurements set by the user at the first step. Finally, the magnetic field is switched off in order to avoid heating of the pick-up coils. The block diagram of the close-loop control system is shown in Figure 4.21.

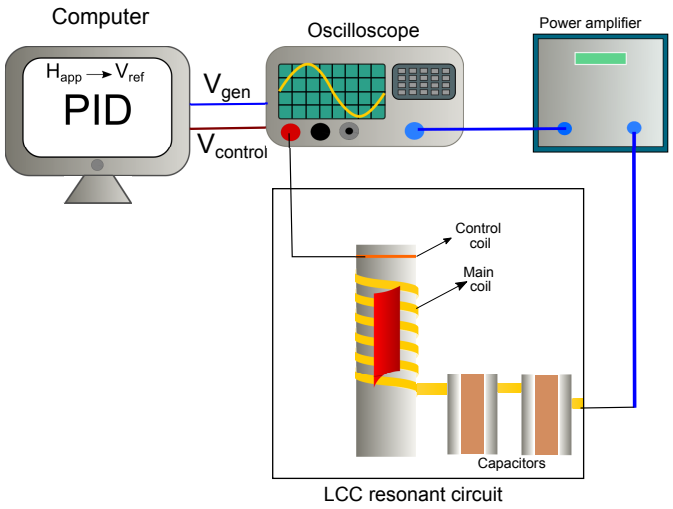

FIGURE 4.21: Close-loop control system used to generate the set magnetic field.

3. Temperature stabilization: An air-flow is introduced inside the main coil and its temperature is varied until the desired temperature in the sample is obtained. This procedure is done using the temperature system and the PID described in the Section 4.2.

4. Minimum feedthrough position establishment: The minimum feedthrough position is determined using an additional software PID designed in the LabVIEW program. In this case, the signal of the control coil, $V_{control-coil}(t)$, and the pick-up coil in the absence of sample, $V^{empty}_{pick-up}(t)$, are recorded simultaneously along the z axis of the main coil by moving the pick-up coil with the motorized xyz translation stage in steps of 50 nm. As it is shown in Figure 4.14, the control coil and pick-up coils' signal are in quadrature at minimum feedthrough position. Taking this condition as reference, the phase difference between the control coil and pick-up coil signal is recorded. The measured phase difference and reference

condition (quadrature) are compared and the position of the pick-up coil is increased until both conditions converge. Finally, the magnetic field is switched off and the position of the pick-up coils is recorded.

5. AC hysteresis loop measurements: Once the temperature is stabilized and the pick-up coil position with minimum feedthrough is fixed, AC hysteresis loop measurements are carried out. The signals of the control coil and the pick-up coil in the presence of the sample are recorded simultaneously following the procedure explained in Section 4.3.1. After, the fast Fourier transform (FFT) is applied to the resulting time varying signals, $V^{sample}(t)$ and $V_{control}(t)$, generating frequency-domain spectra. With the aim of filtering both signals, the fundamental harmonic of the control coil signal and the fundamental and odd harmonics of the sample voltage signal are considered. The time domain voltage is then reconstructed using the inverse Fourier transformation and integrating the harmonics. After, using the calibration constants calculated in Section 4.1.3 and Section 4.3.2 the magnetic field and dynamical magnetization are obtained. Finally, the AC hysteresis loops are acquired by plotting the dynamic magnetization, $M(t)$, as a function of the magnetic field, $\mu_0 H(t)$ (see Figure 4.22). In order to measure the AC hysteresis loops at different magnetic fields this procedure is repeated for all the element of the V_{gen} array calculated in the second step.

6. *SAR* calculation:The specific absorption is extracted by computing the area, A, enclosed by the hysteresis loops, multiplied by the number of loops per second (frequency) and normalized by the sample concentration (mass per unit volume of the colloidal sample) [10]:

$$SAR\left(Wg^{-1}\right) = \frac{f}{c}A = \frac{f}{c}\mu_0 \oint MdH \tag{4.8}$$

The minimum feedthrough position establishment, AC hysteresis loop measurements and SAR calculation are repeated for all the sample temperatures set by the user in step one.

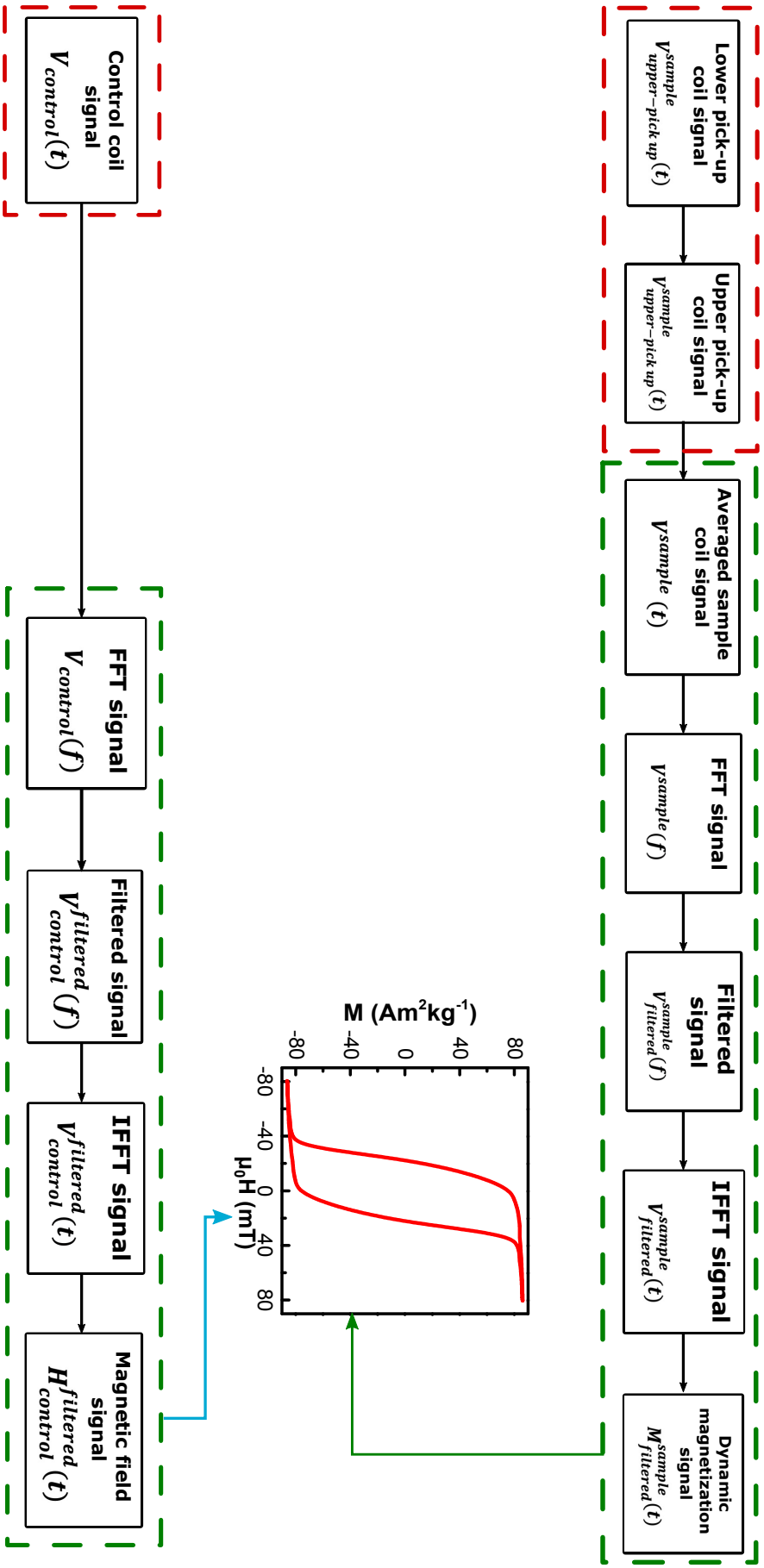

FIGURE 4.22: Procedure followed to measure AC hysteresis loops. Red rectangles indicate steps involved in the measurement of signals and the green rectangles data processing.

4.5 AC magnetometer sensitivity and *SAR* error

General view of the programmed software for the control and acquisition of the measurement.

Figure 4.23 shows the AC hysteresis loop measured in water following the protocol explained before at 90 mT and 134 kHz. This measurement corresponds to the background arising from the feedthrough signal. The sensibility of the AC magnetometer can be extracted from the displayed data considering that the amplitude of the magnetization is 1.24 Am^2kg^{-1} and the volume of the sample is 100 μl. This results in a sensitivity of 1.24 10^{-3} emu.

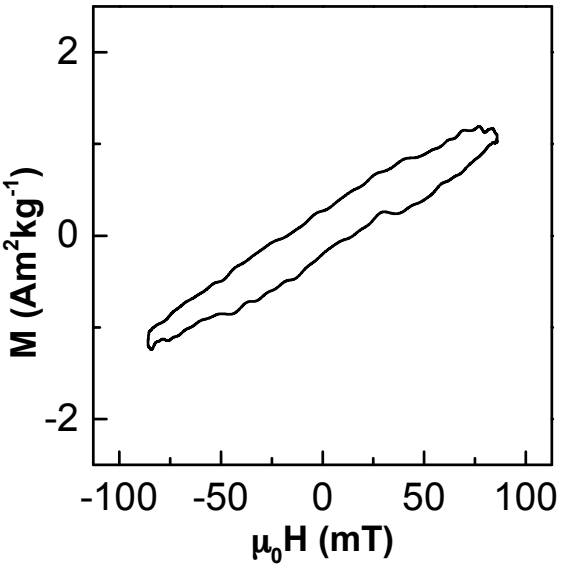

FIGURE 4.23: AC hysteresis loop of water sample measured at a magnetic field of 90 mT and 134 kHz.

On the other hand, to estimate the error of the *SAR* measured with the developed AC magnetometer the same measurement is performed 15 times using the sample of Section 4.3.2. From the obtained data the relative error of the area is calculated: $\frac{\Delta A}{A} = 0.011 = 1.10$ %. However, the concentration also introduces an error in the *SAR* that it has to be taken into account. [1]

[1]This error is related with the instruments that are used when estimating the value of the concentration and it is previously set in the laboratory at $\frac{\Delta c}{c} = 0.050 = 5$ %. Note, that the error of the area comes from the AC magnetometer, whereas the error of the concentration arises from additional techniques; however, both of them influence the *SAR* value's error. Thus, applying the error propagation rule the *SAR* relative error is obtained: $\frac{\Delta c}{c}$=0.051. This result indicates that the main error in obtaining *SAR* values with the present setup relies on colloidal concentration measurement error.

4.6 Conclusions

A versatile AC magnetometer able to work in a large range of frequencies (50 kHz-1 MHz) that are relevant for magnetic hyperthermia experiments, and capable of applying remarkably higher field intensities than those existing so far is developed. With a power amplifier limited to 1 kW, the geometry of the coil is carefully designed to reach 90 mT at 50 kHz and 30 mT at the maximum frequency of 950 kHz. The homogeneity in the working area (pick-up coil included) of 20 mm is 3.5 %. It has been demonstrated than skin and proximity effects strongly constrain the optimal number of turns as well as the use of more winding layers. The best geometry for a coil of 12 mm in diameter and 41 mm in length corresponds to a single layer coil with 12 turns. Additionally, our device incorporates a variable temperature system for continuous measurements between 220 and 380 K. The dynamic magnetization measurement system that consist of two oppositely wound pick-up coils is implemented. The position of the pick-up coils inside the main coil is adjusted using a motorized *xyz* translation stage to minimize the feedthrough signal in each working temperature. An additional motorized z axis stage translates the sample inside each pick-up coil for every measurement to obtain the magnetization more accurately. The magnetic field generated by the main coil and the magnetization are calibrated. Finally, a homemade LabVIEW program is designed to control the measurements and process the data. In the next chapter the potential of the built AC magnetometer will be analyzed. With this aim, SAR measurements of several MNPs are performed with the built device.

Bibliography

[1] I. Rodrigo, I. Castellanos-Rubio, E. Garaio, O. K. Arriortua, M. Insausti, I. Orue, J. García, and F. Plazaola, "Exploring the potential of the dynamic hysteresis loops via high field, high frequency and temperature adjustable AC magnetometer for magnetic hyperthermia characterization," *International Journal of Hyperthermia*, vol. 37, no. 1, pp. 976–991, 2020.

[2] P. R. Stauffer, P. K. Sneed, H. Hashemi, and T. L. Phillips, "Practical induction heating coil designs for clinical hyperthermia with ferromagnetic implants," *IEEE Transactions on Biomedical Engineering*, vol. 41, no. 1, pp. 17–28, 1994.

[3] D. E. Bordelon, R. C. Goldstein, V. S. Nemkov, A. Kumar, J. K. Jackowski, T. L. DeWeese, and R. Ivkov, "Modified Solenoid Coil That Efficiently Produces High Amplitude AC Magnetic Fields With Enhanced Uniformity for Biomedical Applications," *IEEE Transactions on Magnetics*, vol. 48, no. 1, pp. 47–52, 2012.

[4] J. Alonso-Valdesueiro, B. Sisniega, I. Rodrigo, J. Pérez-Muñoz, J.-M. Collantes, and F. Plazaola, "Design, Construction, and Characterization of a Magic Angle Field Spinning RF Magnet," *IEEE Transactions on Instrumentation and Measurement*, vol. 68, no. 10, pp. 4094–4103, 2019.

[5] B. Mehdaoui, J. Carrey, M. Stadler, A. Cornejo, C. Nayral, F. Delpech, B. Chaudret, and M. Respaud, "Influence of a transverse static magnetic field on the magnetic hyperthermia properties and high-frequency hysteresis loops of ferromagnetic FeCo nanoparticles," *Applied Physics Letters*, vol. 100, no. 5, p. 052403, 2012.

[6] S. A. Gudoshnikov, B. Y. Liubimov, and N. A. Usov, "Hysteresis losses in a dense superparamagnetic nanoparticle assembly," *AIP Advances*, vol. 2, no. 1, p. 012143, 2012.

[7] S. A. Gudoshnikov, B. Y. Liubimov, Y. S. Sitnov, V. S. Skomarovsky, and N. A. Usov, "AC Magnetic Technique to Measure Specific Absorption Rate of Magnetic Nanoparticles," *Journal of Superconductivity and Novel Magnetism*, vol. 26, no. 4, pp. 857–860, 2013.

[8] M. Veverka, K. Závěta, O. Kaman, P. Veverka, K. Knížek, E. Pollert, M. Burian, and P. Kašpar, "Magnetic heating by silica-coated Co–Zn ferrite particles," *Journal of Physics D: Applied Physics*, vol. 47, no. 6, p. 065503, 2014.

[9] E. Garaio, J. M. Collantes, F. Plazaola, J. A. Garcia, and I. Castellanos-Rubio, "A multifrequency eletromagnetic applicator with an integrated AC magnetometer for magnetic hyperthermia experiments," *Measurement Science and Technology*, vol. 25, no. 11, p. 115702, 2014.

[10] G. Bertotti, "Chapter 2 - Types of Hysteresis," in *Hysteresis in Magnetism* (G. Bertotti, ed.), Electromagnetism, pp. 31–70, San Diego: Academic Press, 1998.

Chapter 5

Experimental AC magnetometry measurements via high field, high frequency and temperature adjustable AC magnetometer

So far, the magnetic saturation was an unexplored region by AC magnetometry. Non saturated hysteresis loops, i.e. minor loops, provide incomplete information about the magnetization dynamical properties. With the aim of investigating the saturation region of MNPs, the high field, high frequency and temperature adjustable AC magnetometer is used.

In this chapter, the potential of the AC magnetometer is explored by analyzing the obtained experimental data that has not been available until now. These analyses will enable us to shed light in some of the issues that rise in magnetic hyperthermia experiments: First, the relation between the magnetically saturated AC hysteresis loops and the saturation of the SAR. Second, the influence of the excitation intensity, frequency and particle size on the area of the hysteresis loops. Third, the contribution of mechanical rotation of particles and particle assemblies to experimental SAR in viscous media. Finally, the optimal magnetic field excitation parameters (intensity and frequency) for maximizing SAR within the human safety limit for hyperthermia experiments is also addressed. Aiming to address some of the previous issues, the major hysteresis loops

of the studied MNPs are discussed in the framework of Stoner–Wohlfarth model based theories (SWMBTs) of uniaxial single magnetic domains [1].

5.1 Inorganic iron oxide MNPs

The samples presented in this chapter have been prepared by the Department of Inorganic Chemistry at the University of the Basque Country (EHU/UPV). Four different samples of magnetite (Fe_3O_4) nanoparticles with sizes ranging from 16 nm to 29 nm are synthetized following the method developed in Castellanos *et al.* [2]. The samples are coated with poly(maleic anhydride- alt-1-octadecene) (PMAO) to enhance colloidal stability in water. This range of particle size (16-29 nm) is usually considered as a good choice to maximize the SAR value. The samples are labelled as sample A (16 ± 2 nm), sample B (19 ± 1 nm), sample C (21 ± 2 nm) and sample D (29 ± 3nm) (see Table 5.1).

5.2 Characterization of samples

5.2.1 Structural and magnetic characterization

TEM images are taken to determine shape and size distribution of the particles. The MNPs present a cuboctahedral shape and a narrow size distribution of roughly Gaussian shape. As it can observed in Figure 5.1, clustering effects are not severe in the studied samples. However, the largest particles (sample D) shows a clear chaining tendency (Figure 5.1 (d)).

Sample	**Crystalline size [nm]**	**TEM size [nm]**
A	15(1)	16(2)
B	18(1)	19(1)
C	23(1)	21(2)
D	29(2)	29(3)

TABLE 5.1: Parameters obtained from the deconvolution of (311) XRD peak corresponding to magnetite and crystalline size obtained using Scherrer equation. The last sizes are compared with the sizes measured by TEM microscopy.

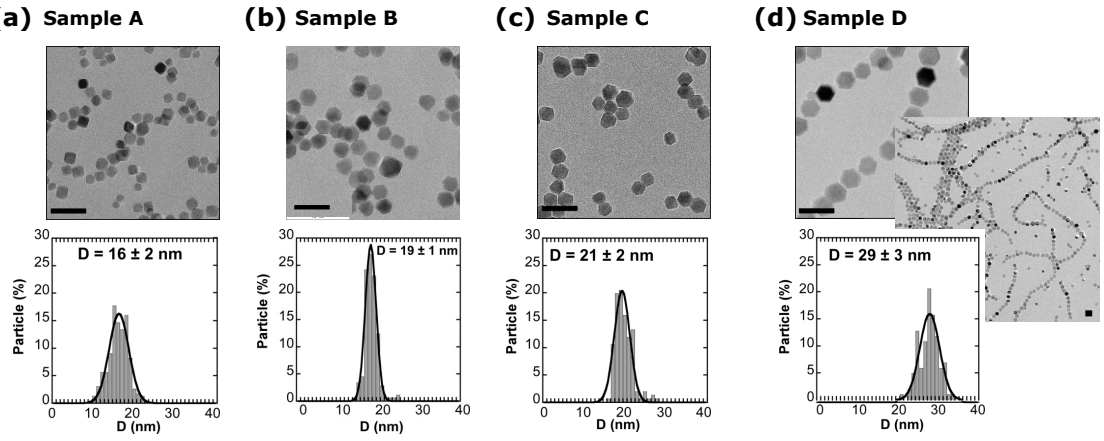

FIGURE 5.1: TEM images of samples (a) A, (b) B, (c) C and (d) D together with their corresponding size distributions. Scale bar 50 nm. Sample D shows a tendency to form chains.

The crystallite sizes of samples A–D are obtained by X-ray diffraction (XRD) on powder samples from the deconvolution of the main diffraction peak of magnetite (311) using the Scherrer's equation [3].

As it can be observed in Table 5.1, the sizes of the crystalline domains are very similar to the ones measured by TEM microscopy. Therefore, it can be concluded that the studied nanoparticles are single crystals.

DC magnetization measurements as a function of the magnetic field, *M(H)* and temperature *M(T)* are carried out using a SQUID magnetometer (MPMS3, Quantum design). The measurements of samples A-D are performed in diluted samples, prepared by depositing a drop of the colloidal dispersion on a laboratory blotting paper to prevent fast diffusion and agglomeration of colloidal particles.

Figure 5.2 shows the thermal dependence of magnetization, *M(T)*, obtained upon zero field cooling and field cooling (ZFC and FC) conditions, between room temperature and 5 K, at a constant field of 1 mT. The derivative of the ZFC curves (red solid line) presents a sudden maximum when crossing 80-100 K temperature range. In magnetite, this maximum corresponds to the *Verwey transition* and it is located at 110 K. Shifting of the *Verwey transition* to lower temperatures corresponds to non-stoichiometric magnetite particles [2, 4].

Figure 5.3 (a)-(d) shows DC *M(H)* hysteresis loops at 5 K (red solid line) and 300 K (black solid line) for samples A-D. The low temperature hysteresis loops shown in Figure 5.3 (a)-(d) (red solid line), where thermal fluctuations are damped down,

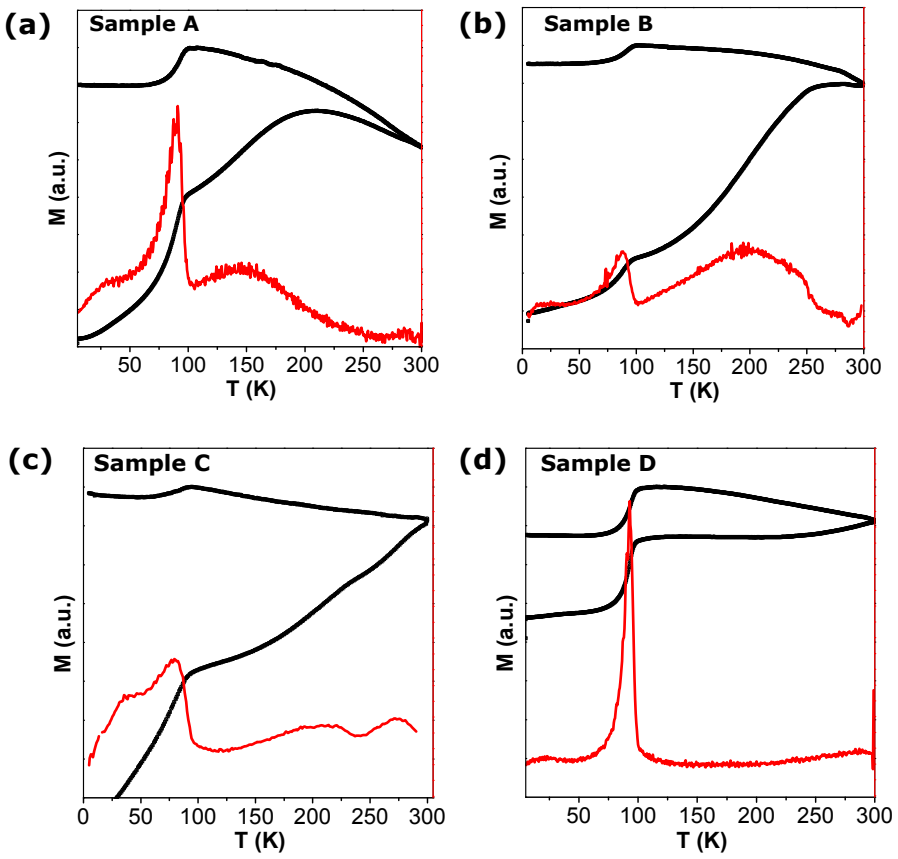

FIGURE 5.2: ZFC-FC curves (black solid line) together with derivatives of ZFC magnetization (red solid line) for samples (a) A, (b) B, (c) C and (d) D.

are characteristic of uniaxial single domains MNPs oriented at random according to SWMBT, with remanence (M_r/M_s) approaching 0.5 and coercive field values, $\mu_0 H_c$, ranging from 40 to 50 mT. This does not necessary mean that our MNPs are magnetically isolated. However, at least, we are certain that particles are not forming large and chaotic clusters where dipolar interactions would favor antiparallel configuration of particles' magnetization and then a remarkably decrease of the reduced remanence.

Thermal fluctuation effects become strongly significant at room temperature (Figure 5.3 (a)-(d) (black solid line)), to the point of almost removing the hysteresis loop (remanence and coercivity) in two of the samples with sizes of 16 and 19 nm. The two smallest samples show clear blocking effect below room temperature whereas in the two largest, 21 and 29 nm, thermal effects are small (see insets of Figure 5.3).

Additionally, saturation magnetization values have been obtained by measuring dried powder samples up to high DC field. The total magnetic moment can be correctly normalized by subtracting the organic contribution to the total mass, which is

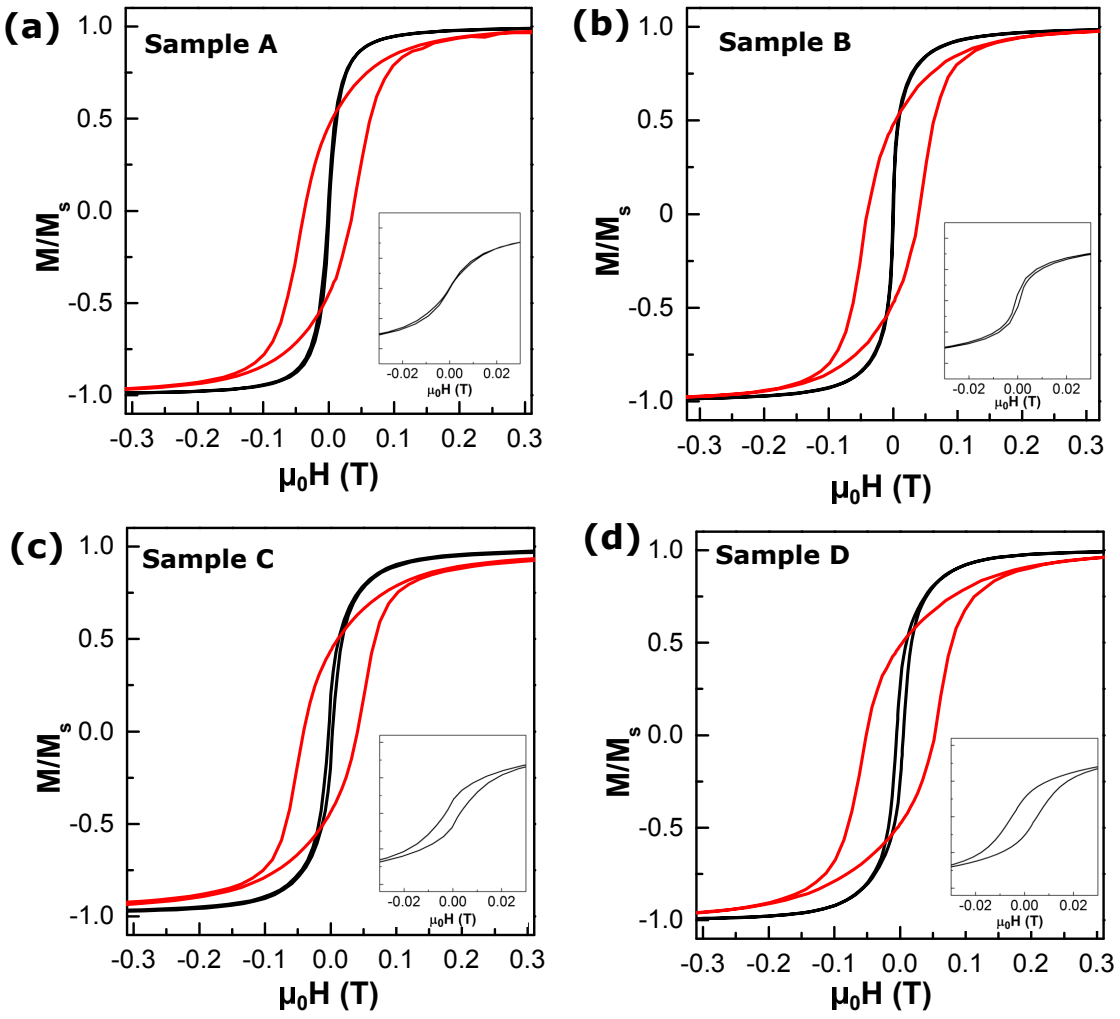

FIGURE 5.3: DC hysteresis loops at 5 K (red solid line) and at 300 K (black solid line) for samples (a) A, (b) B, (c) C and (d). In the inset, a zoom of AC loops at 300 K in the origin is presented.

determined by means of a Thermogravimetric Analyzer (TGA). The single domain magnetization values obtained from high field DC measurements (up to 2 T, see Figure 5.4) range from 80 to 89 Am^2kg^{-1}. These values are rather close to that of pure magnetite (92 Am^2kg^{-1}), confirming the high purity of the crystalline phase. In any case, magnetization variations from sample to sample are not very significant, so, we take an average of 86 Am^2kg^{-1} (or conversely 450 kAm^{-1}) for the hysteresis loop simulations that will be discussed later.

Therefore, we can conclude that the selected samples are magnetite phase single crystals showing weak interparticle interactions.

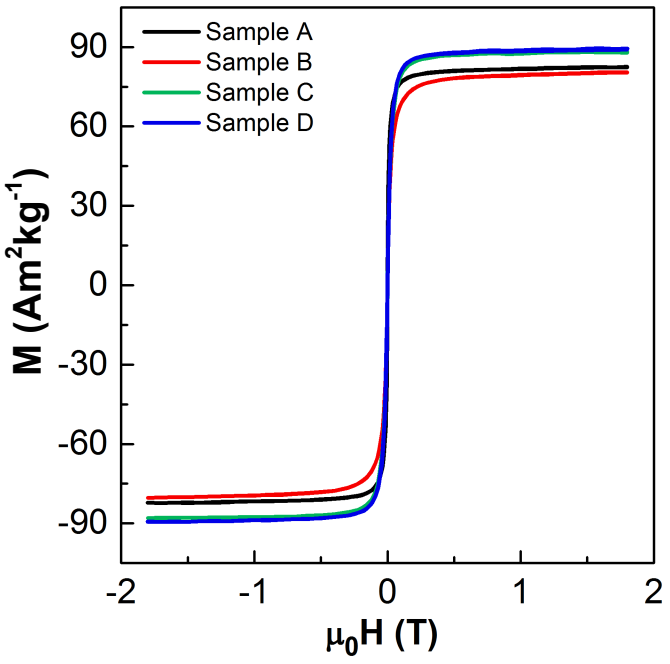

FIGURE 5.4: DC hysteresis loops of dried samples measured at room temperature. Saturation values for samples A-D range from 80 to 89 Am^2kg^{-1}.

5.2.2 AC magnetometry characterization

The AC hysteresis loops of samples A-D dispersed in water are recorded at different magnetic field intensities up to 90 mT at 134 kHz and room temperature (RT). As observed in Figure 5.5 (a)-(d) the magnetization of all the samples saturates at fields higher than 50 mT and hysteresis area remarkably grows with the particles' size. It is noteworthy that the loop of the largest sample has a highly squared shape, with a large remanence close to 80 Am^2kg^{-1}.

Obviously, given that samples are in aqueous solution, the colloidal magnetic particles are able to mechanically rotate during the experiments. It happens due to different mechanical effects that potentially exist in a liquid medium: (1) the rotational Brownian motion of small colloidal particles, (2) the mechanical rotation of magnetic particles towards the magnetic field direction due to the magnetic torque and (3) the potential space rearrangement of particles in chains, either preexisting in the colloidal sample due to dipolar interactions or induced by the applied AC magnetic field during measurements. In order to avoid the potentially complex problem of understanding a mix of different physical mechanisms happening at the same time and to discriminate the effect of physical rotation, AC loops can be directly measured below the freezing point of the

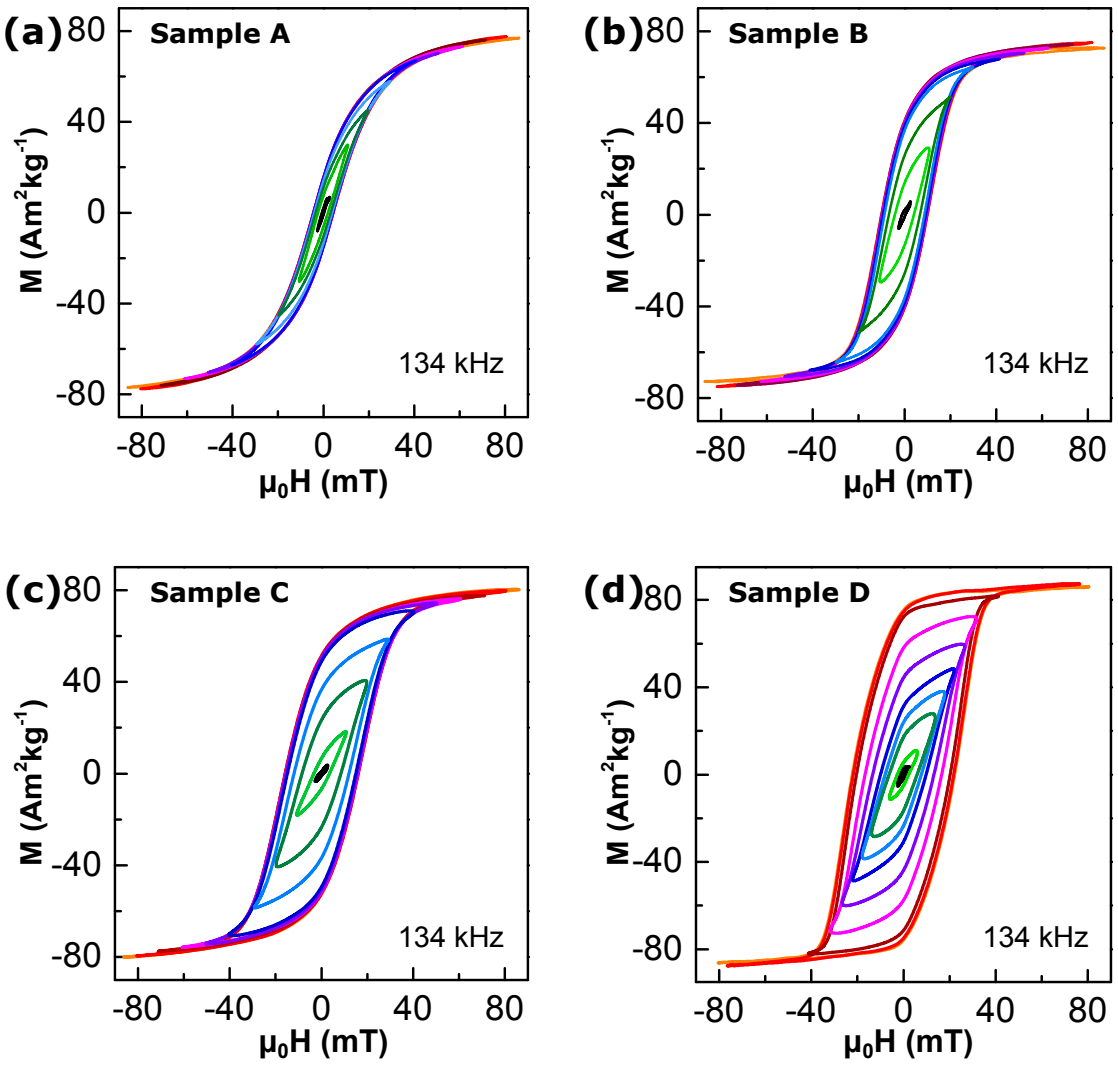

FIGURE 5.5: AC hysteresis loops of samples (a) A, (b) B, (c) C and (d) D measured at room temperature under a maximum magnetic field of 90 mT at 134 kHz. Note that all the samples saturate almost at 50 mT. As the size of the sample increases, the loop broadens obtaining a squared shape loop in the case of sample D.

solvent, water in this case. Figure 5.6 shows the AC hysteresis loops at 253 K (-20 °C), corresponding to a maximum magnetic field of 90 mT at 134 kHz, in the four studied samples after freezing them. These hysteresis loops (red solid lines) are compared with those obtained in liquid samples (black solid lines). In these experiments, the temperature of the air flowing through the sample chamber is kept constant at 253 K, low enough to freeze the water solvent completely.

As can be observed in Figure 5.6 (a) hysteresis loops of sample A remain approximately unchanged after freezing. Considering that the Brownian contribution becomes less important with decreasing the size of MNPs it is reasonable that the immobilization effect produced in frozen medium doesn't affect the behavior of sample A. On the

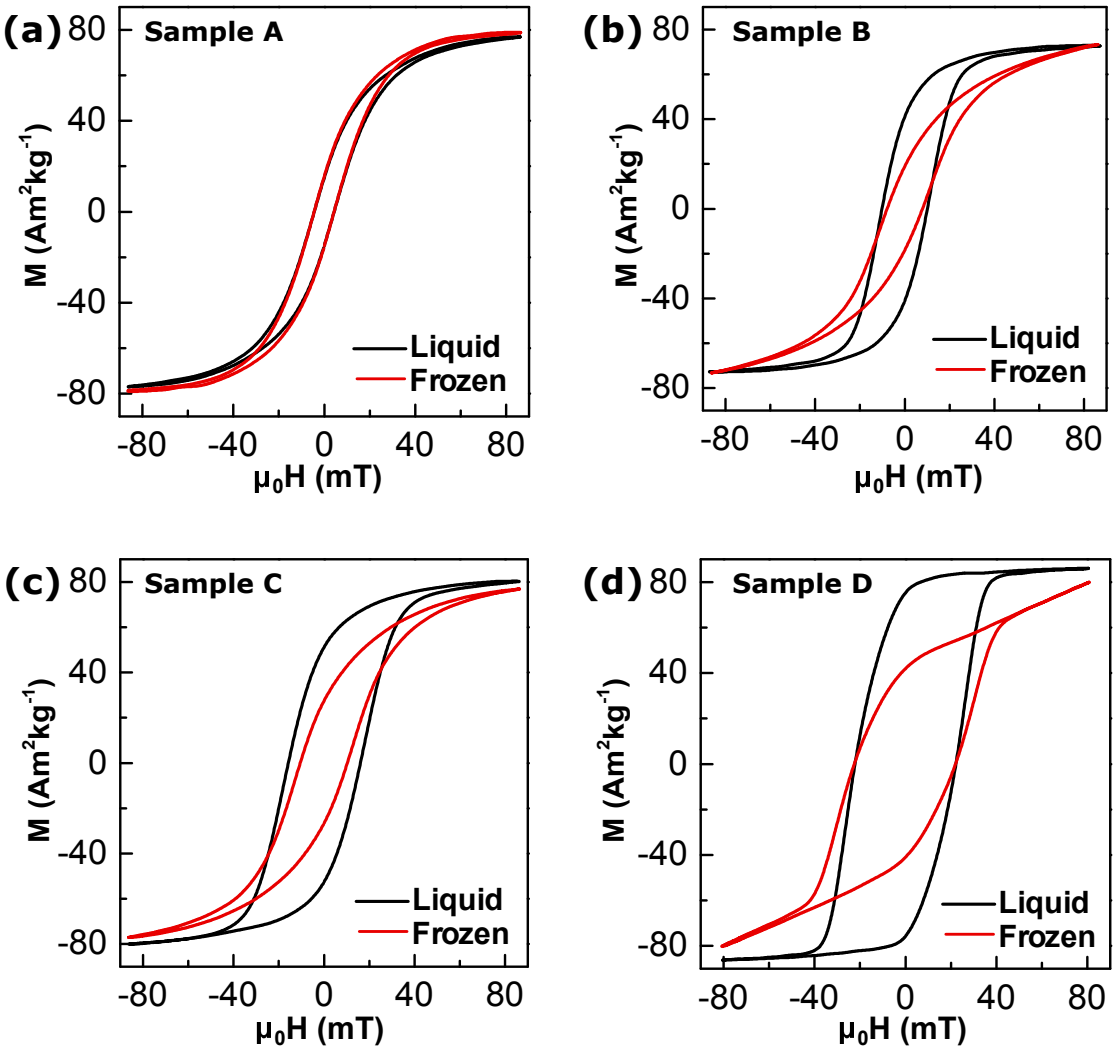

FIGURE 5.6: AC hysteresis loops of samples (a) A, (b) B, (c) C and (d) D under a maximum magnetic field of 90 mT at 134 kHz in room temperature/liquid state (black) and frozen state (red).

contrary, the AC hysteresis loops in water and frozen medium of sample D show different shape. In water the shape of the AC hysteresis loop becomes squared with high remanence magnetization. However, when particles are dispersed in frozen medium they show tilted AC hysteresis loops with smaller remanence magnetization. A possible explanation of this relies on the ability of sample D to form chains and align them along the magnetic field. Finally, samples B and C (Figure 5.6 (b)-(c)) stands in the midway between the behavior of samples A and D. Figure 5.7 shows the experimental *SAR* curves built after computing the hysteresis loop area as function of the external field amplitude in liquid and frozen states.

It is to note that, in the samples with the largest particles' size (samples C and D), *SAR* increases with field in a strongly non-linear way, saturating with field amplitudes

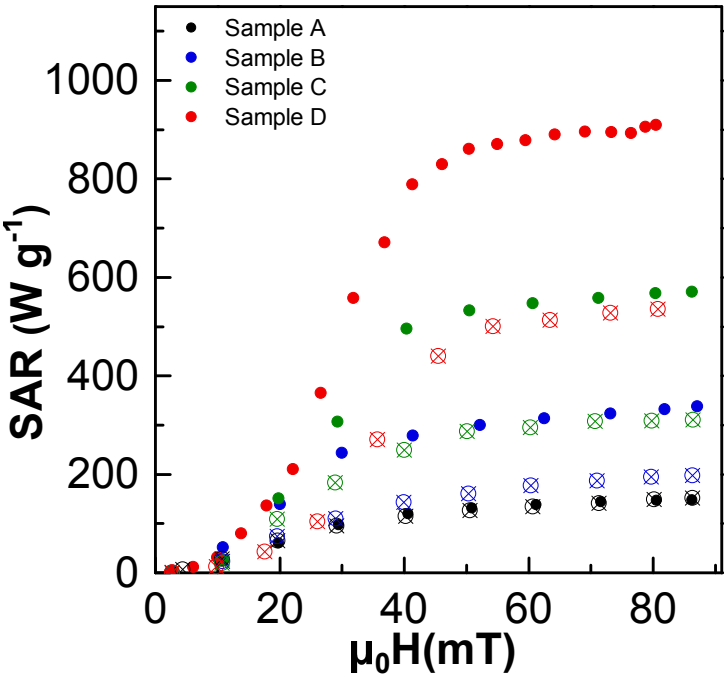

FIGURE 5.7: *SAR* versus field intensity curves obtained from the area of AC hysteresis loops under the field frequency of 134 kHz at liquid (solid dots •) and frozen state (empty dots ⊗).

above the threshold of 50 mT. The slope changes of SAR versus $\mu_0 H$ curve presented in Figure 5.7 are less pronounced in the smallest particles (samples A and B). Remarkable differences between liquid and frozen samples are very visible in Figure 5.7. Sample D (largest particles) shows much less hysteresis area in the frozen state. This is basically due to the much smaller value of the remanence magnetization, while the coercive field remains almost unchanged. In consequence, the maximum SAR value of sample D in the frozen state is reduced by a factor of 0.6 relative to the liquid case (540 Wg^{-1} vs 910 Wg^{-1}, red curves in Figure 5.7). On the contrary, hysteresis loops of sample A remains approximately unchanged after freezing (Figure 5.6 (a)) and consequently the SAR value doesn't vary. As shown before, samples B and C stands on the midway between the behavior of samples A and D. In these cases, SAR is reduced by a factor of 0.52 and 0.58 in Samples B and C, respectively.

Figure 5.8 presents the dependence of AC hysteresis loops and their area with frequency. Figure 5.8 (e)-(h) shows the experimental values of SAR/f versus magnetic field intensity at 134 kHz, 561 kHz and 835 kHz frequencies in frozen media. The hysteresis area increases with frequency for particles in frozen solution, but this increment depends critically on particle's size. Thus, for instance, the increase of SAR/f with frequency is

particularly intense in the case of sample A, composed of particles of 16 nm size (Figure 5.8 (e)). As particle's size increases, SAR/f curves tend to collapse (Figure 5.8 (f)-(g)). Finally, SAR/f curves in sample D almost collapse in a single one (Figure 5.8 (h)). This behavior can also be observed in Figure 5.8 (a)-(d), where AC hysteresis loops of the four samples are plotted at different frequencies under 30 mT magnetic field intensity. Note that in sample A (Figure 5.8 (a)), as frequency increases the hysteresis loop broadens. This hysteresis growth is less pronounced in sample B and C (Figure 5.8 (b)-(c)). Finally, in sample D (Figure 5.8 (d)), the hysteresis loops of different frequencies are almost superimposed in a single curve.

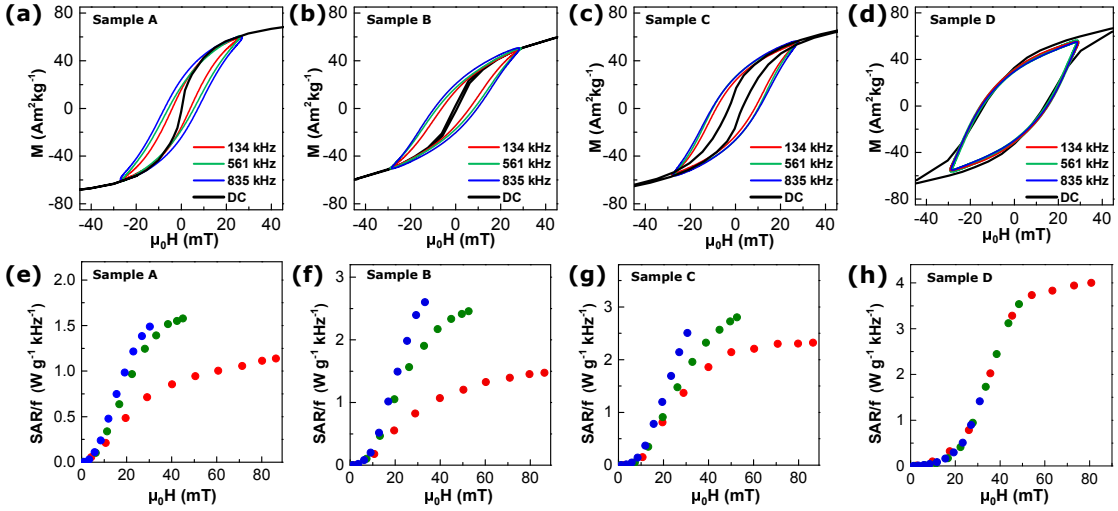

FIGURE 5.8: First row: AC hysteresis loop of samples (a) A, (b) B, (c) C and (d) D at 134kHz (red), 561kHz (green), 835kHz (blue) and DC (black) in frozen media at 30 mT. Second row: SAR/f versus field intensity curves obtained from the area of AC hysteresis loops at 134kHz (red), 561kHz (green) and 835kHz (blue) of samples (e) A, (f) B, (g) C and (h) D.

5.3 Beyond saturation: Analysis of an unexplored area

As mentioned before, the main purpose of this chapter is not aimed neither to present new theoretical models nor to discuss the magnetic properties of new samples. Rather, we intend to understand previous results in the light of the existing models, which have proved useful to explain and predict, to a great extent, the magnetic properties pertaining to hyperthermia. We will focus on those properties for which our novel AC magnetometer provides new experimental data that has not been available, so far. Our aim is to answer some of the issues previously raised at the beginning of this chapter.

5.3.1 The question of the mechanical rotation contribution to hyperthermia

When magnetic particles immersed in a liquid medium are considered as free-rotating isolated objects, whose magnetization is supposed to be pinned to an easy magnetization axis, their dynamical response to AC magnetic fields can be calculated in the framework of magnetic single domain theories [5–7]. In brief, the available predictions suggest that at small enough field amplitudes (meaning much smaller than the anisotropy field, $H_k = 2K_{eff}/\mu_0 M_s$, for single domains particles with uniaxial anisotropy), the external torque exerted by the alternating magnetic field should produce forced angular oscillations of the particles at the excitation frequency of the field [6]. The amplitude and phase of these angular oscillations will depend on the applied magnetic field frequency and will peak (they are in resonance) when excitation frequency approaches the Brownian relaxation time [8]. This relaxation time can be determined from the particle's size (hydrodynamic volume V_h), the viscosity of the medium η, and the external AC magnetic amplitude H, by the following expression [8]:

$$2\pi\tau_{B-eff}(H)) = \tau_B \left[1 + \left(\frac{\mu\mu_0 H}{k_B T}\right)^2\right]^{-0.5} \tag{5.1}$$

where τ_B is the well-known Brownian relaxation time at zero field, ${}^{3\eta V_h^3}/_{k_B T}$, k_B is the Boltzmann constant and μ the relative magnetic permeability. According to this model, pseudo-spherical particles of magnetite ($M_s = 480$ kAm^{-1}) in the size range 16-20 nm are expected to turn around at a rate of the order of hundreds of kHz, just in the range of the AC excitation frequency used in hyperthermia. Note that, if thermal energy is much higher than the anisotropy energy, the particle magnetic moment "unpins" from the easy axis and therefore becomes mostly collinear with the external AC field at all times. Thus, the magnetic torque and Brownian effect tend to be removed.

However, the strength of AC fields of interest to hyperthermia is far from being small relative to the anisotropy field, particularly for magnetite particles. Assuming that the anisotropy field of a typical magnetite particle lies around 50 mT, hyperthermia AC fields easily approach or overcome the anisotropy energy barrier for magnetization reversal ($K_{eff}V$).

In general, Néel relaxation time as a function of the external field can be estimated from the following equation [8]:

$$\tau_N(H)^{-1} = \tau_0^{-1}\left(1-h^2\right)\left\{(1+h)\,exp\left[\left(\frac{-K_{eff}V}{k_BT}\right)(1+h)^2\right] + (1-h)\,exp\left[\left(\frac{-K_{eff}V}{k_BT}\right)(1-h)^2\right]\right. \tag{5.2}$$

where $h = H/H_k$ and τ_0 is a constant (10^{-9}-10^{-10} s). In these conditions, Néel relaxation can be strongly accelerated by several orders of magnitude depending on the field strength [8], leading Brownian rotations to be accordingly suppressed.

The results of Figure 5.6 (a) indicate that in sample A, thermal fluctuations alone remove the Brownian rotation contribution to the *SAR*: hysteresis loops obtained at any AC amplitude remain almost unchanged upon the freezing of water. If the anisotropy constant is in the range of 10-15 kJm^{-3} [4, 9], Néel relaxation time is always smaller than $\sim 10^{-8}$-10^{-9} s and therefore always much faster than Brownian relaxation time calculated from Equation 5.2.

In this case reversal mechanisms largely dominate over rotation ones. For samples B, C and D, composed of the largest particles, Brownian relaxation becomes faster than Néel relaxation at zero field, particularly for sample D (29 nm), assuming that particles of the assembly do not form clusters and the hydrodynamic volume is similar to particle's volume. Given that Néel relaxation will be much faster at high enough field amplitudes, the changeover between rotation and reversal mechanisms could lead to a complex behavior of the hysteresis area as a function of the AC amplitude in samples B, C and D, as predicted from the available calculations in the literature [6].

On the other hand, particles with permanent magnetization tend to agglomerate easily in pseudo spherical clusters and/or to form chains. The size of these large objects makes them unable to respond to the magnetic field excitation in the form of angular oscillations. However, when magnetization moment vector of a magnetic object (a single particle or a whole chain for instance) irreversibly switches between different orientations driven by the applied magnetic field, the time averaged magnetic torque over such object is non-zero. As a result, the magnetization easy axis is impelled to rotate towards the

magnetic field lines after a given number of field cycles. This alignment effect has been predicted from direct numerical calculations of the dynamical equations for single magnetic domains [6], but it can be also qualitatively understood appealing to simpler arguments. For instance, let's assume that the instantaneous net magnetic moment vector $\boldsymbol{m}(t)$ takes the following simple form as a function of time in response to an external AC magnetic field given by $\boldsymbol{H}(t) = H_0 \sin(\omega t)\boldsymbol{u}_H$:

$$\boldsymbol{m}(t) = m_0 \sin(\omega t - \varphi)\boldsymbol{u}_H + m_0 \cos(\omega t - \varphi)\boldsymbol{u}_\perp \tag{5.3}$$

where $\boldsymbol{u}_\perp$ is the unit vector perpendicular to $\boldsymbol{u}_H$ (see Figure 5.9) and φ the phase shift of $m_\perp$ relative to H. Even though, Equation 5.3 cannot represent a correct solution of the dynamical problem, it works here as a crude approximation that can represent the first harmonic of the magnetic moment components, parallel and perpendicular to the magnetic field direction (μH). Assuming that the easy axis of the magnetic object does not have time to appreciably rotate during a complete cycle of the external field, this torque can be averaged in a field cycle as:

$$\langle T \rangle_{cycle} = \frac{\omega}{2\pi} \int_0^{\frac{2\pi}{\omega}} \mu_0 m_0 H_0 \sin(\omega t) \cos(\omega t - \varphi)\, dt = \frac{1}{2}\mu_0 m_0 H_0 \sin\varphi \tag{5.4}$$

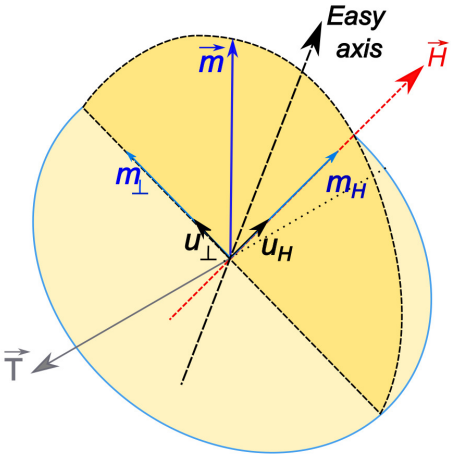

FIGURE 5.9: Definitions of vectors used in Equations 5.3 and 5.4: $\boldsymbol{u}_H$ and $\boldsymbol{u}_\perp$ unit vectors define the direction of the magnetic moment vector, $\boldsymbol{u}_H$ is the unit vector of the magnetic field and $\boldsymbol{u}_\perp$ its perpendicular.

In consequence, this effective mechanical torque is acting always, provided that the magnetic moment component perpendicular to the magnetic field is non-zero. Note that when particles become randomly agglomerated the net magnetic moment of the whole cluster m_0 tend to be close to zero at the remanence state of the system (H=0) and collinear with H at some other instants, so, the net magnetic torque becomes negligible.

Naturally, thermal or stochastic fluctuations of the object in the liquid works to remove the orientation effect, so, large and permanent magnetic moments are essential to produce a full alignment of the magnetic object with the field. In such case, the reduced remanence magnetization becomes much higher than 0.5 for almost any AC field amplitude. The mechanical orientation along the field lines can be observed very clearly in sample D, and in a weaker way in samples B and C, composed of particles of smaller size. It is obvious that this mechanism is size-sensitive, and also happens with isolated or non-interacting particles. However, this effect has been reported as particularly intense in magnetotactic bacteria as it was analyzed in Chapter 3 [10], where the chain arrangement of magnetosomes strongly favors the orientation of bacteria in water-based solutions. Similar behaviours have been observed in free Fe MNPs at 25 mT [11] and FeC MNPs at 44 mT (both at 93 kHz) [12]. It is worthy to note that particles of samples B, C and D have a trend towards chaining with the aim of reducing the magnetostatic energy (as shown in Figure 5.1 (d)). These chains can carry a large permanent magnetic moment. Particularly in sample D, this tendency is stronger and the large squareness of the AC loops (for any field amplitude) could suggest the formation of large chains with well-defined easy axis that become mostly aligned in the magnetic field lines during AC magnetometry experiments. However, the rotation of each individual particle towards the field lines can also contribute to this mechanism and must be considered as a possible explanation.

In any case, the opportunity of fast "removing" any possible mechanical motion *in situ* is interesting for hyperthermia characterization because magnetic objects are not expected to be freely rotating when they are attached to biological entities and quantitative models are aimed at immobilized particles [13].

5.3.2 Validation of Stoner-Wohlfarth model based theories (SWMBTs)

Stoner-Wohlfarth model based theories (see Appendix C) for magnetic single domains predict two properties related to SAR vs magnetic field curve: (1) a very steep increase of the hysteresis area at around a certain threshold field amplitude followed by a saturation field amplitude at which the hysteresis does not increase any longer and (2) this maximum hysteresis area and SAR increase with particle size [14, 15].

The results presented in Figures 5.5, 5.6 and 5.7 imply, to a large extent, the experimental confirmation of the just mentioned theoretical predictions. Note that, until now, the complete lack of full experimental data was still hindering the validation of this model. Figure 5.7 shows the most eye-catching agreement between experiments and theory. Indeed, it arises immediately: the four experimental SAR versus field intensity curves tend to saturate at some values.

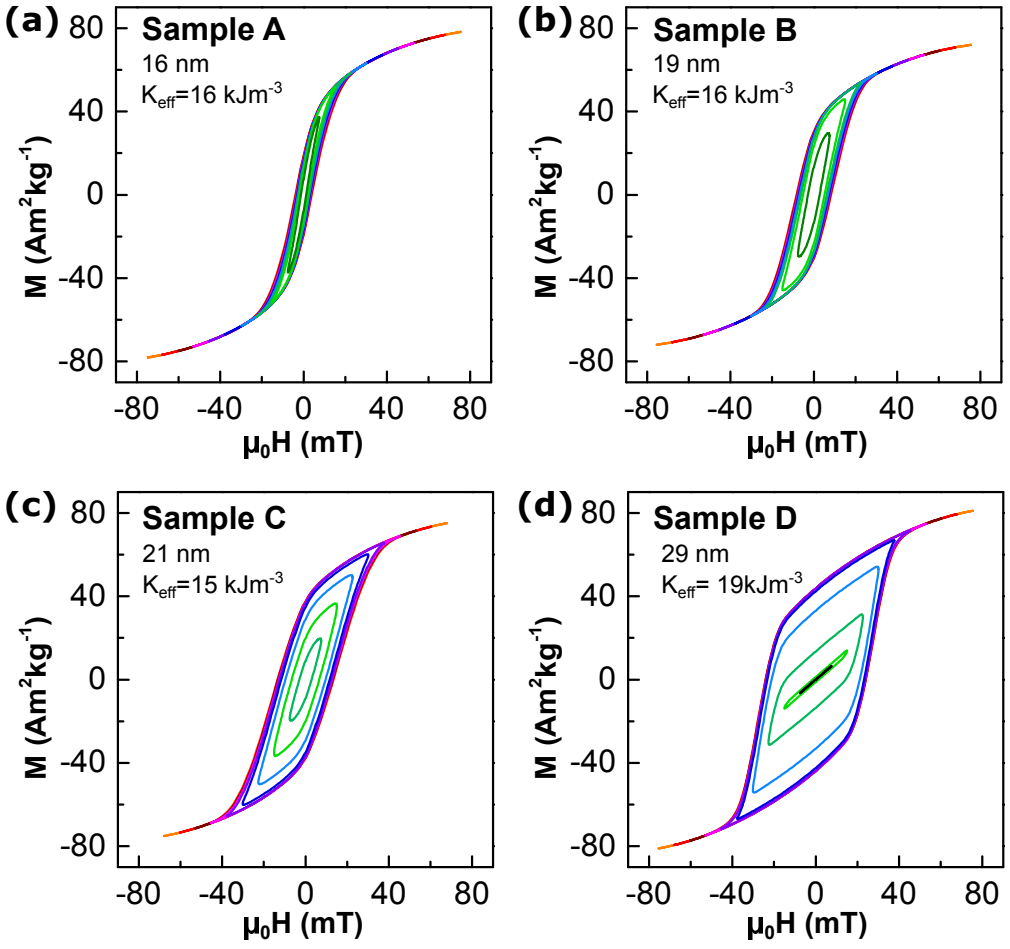

FIGURE 5.10: Simulated AC hysteresis loops of sample (a) A, (b) B, (c) C and (d) D obtained using SWMBTs with uniaxial effective anisotropy.

AC hysteresis loops and SAR values are numerically calculated using SWMBTs. This method was developed explicitly by Carrey *et al.* [15] for the case of uniaxial single domain magnetic particles. However, the approach can be generalized for more complex problems, as those involving cubic, mixed or multiaxial anisotropies [16]. With the aim of building a more realistic and predictive model for our particular samples, we have considered a normal distribution of uniaxial anisotropy constants. We are implicitly assuming that this uniaxial effective anisotropy is the result of combining the magnetocrystalline and the shape effects as well as any hypothetical contribution from dipolar interactions, particularly intense in chains [6, 17]. Note that TEM images (see Figure 5.1) show particles with different degree of elongations and forming chains of different lengths and both effects should favor the onset of a wide range of effective anisotropies.

Figure 5.10 shows the simulated AC hysteresis loops. Best fits with experimental data are obtained by averaging a normal distribution of anisotropy constants with a standard deviation of 5 kJm^{-3} and centered at: Sample A 16 kJm^{-3}, Sample B, 16 kJm^{-3}, Sample C, 15 kJm^{-3} and Sample D, 19 kJm^{-3}. It should be noted that size distribution is not implicitly considered in the simulations, so this standard deviation value (5 kJm^{-3}) should also reflect the particle's size dispersion. For simplicity, the magnetization (450 kAm^{-1}) has been kept equal for all of them.

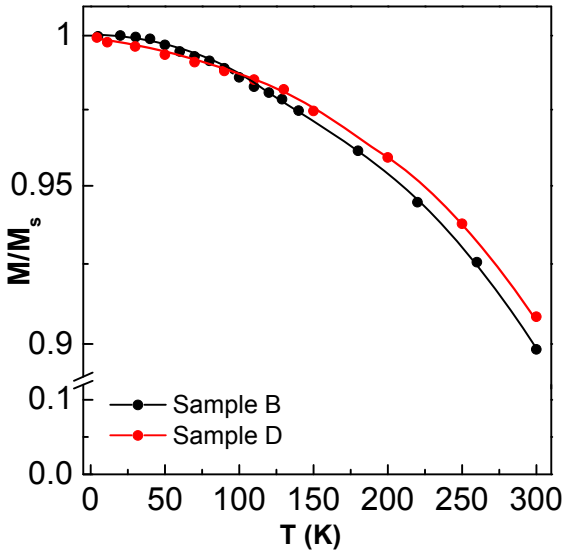

FIGURE 5.11: Normalized magnetization, M/M_s, as function of temperature of samples B and D.

These values for the effective anisotropy constants would be valid at 253 K (temperature of the frozen samples). If one assumes that shape anisotropy contribution is dominant, these effective magnetic anisotropies will depend on temperature as $\propto M^2$, being M the particle's magnetization. Since the magnetization decrease between 253 and 300 K is near 2% (see Figure 5.11), effective anisotropy constant would experience a 4% reduction from 253 K to 300 K, which is not significant because it is within the tolerance of the theoretical approach. It should be noted that, such form of thermal dependence (as M^2) cannot be extrapolated to lower temperatures in our case, due to the presence of the *Verwey phase transition* at around 100 K. A detailed analysis of this issue requires the collection of additional data as a function of temperature and a more complex modelling to take account for the thermal dependence of the magnetocrystalline contribution to the anisotropy. This type of study have been already done in the literature, either with magnetosome [18] , whose thermal behavior is expected to be similar to the samples presented in this work, or very recently with Mn-Zn ferrites [19].

From the numerically obtained AC hysteresis loops, simulated *SAR* values are calculated using Equation 2.8. Figure 5.12 compares the experimental and theoretical *SAR* values at 134 kHz.

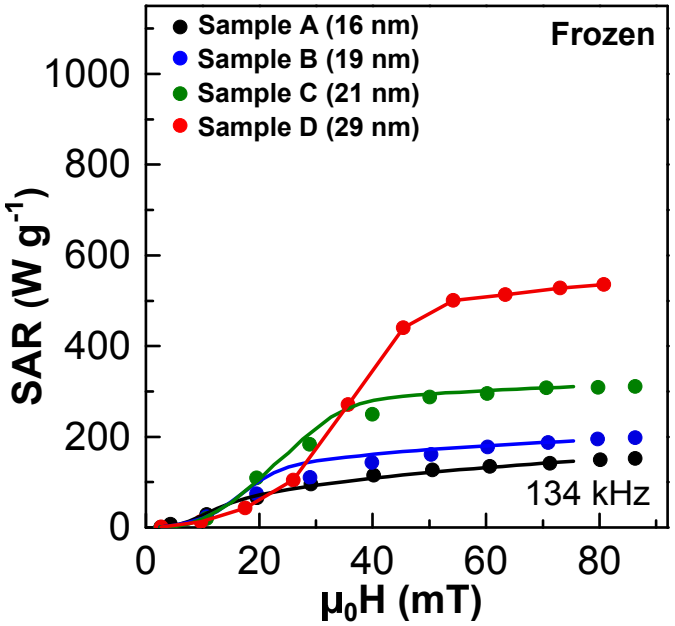

FIGURE 5.12: *SAR* versus field intensity curves obtained from the area of AC hysteresis loops under the field frequency of 134 kHz at frozen state. The dots indicate the experimental results and the lines their corresponding simulations using SWMBTs.

The overall agreement between experiments and simulations in SAR evolution (Figure 5.12) is quite surprising since simplifications made in the modeling are really strong: size distribution has been not taken into account and, most importantly, magnetic dipolar interactions have not been explicitly considered. Obviously, given that the sample D is composed of relatively large particles of 29 nm and they seem to be linked in chains, with minor influence from thermal effects, the SAR versus field curve displays a sharper saturation effect and, in overall, a better matching with the SWMBTs model. Even the samples composed of significantly smaller particles (A and B) follow the qualitative trends predicted by SWMBTs (Figure 5.12).

These findings have two important implications:

- The heating power of MNPs, calculated by AC magnetometry, is a "safe" starting point for modeling the thermal transfer from MNPs to different surrounding media, which is the ultimate goal of magnetic hyperthermia experiments. Therefore, AC magnetometry and calorimetry become very complementary techniques: the former can be used to know the input heat power the latter detects the transfer rate of this power to the environment as the final outcome of the magnetic actuation.

- In "small" particles the effective anisotropy constant, K_{eff}, can be obtained from blocking temperature measurements, but for larger particles this temperature can be unattainable. In the latter case, the determination of SAR vs AC intensity curve up to high field intensities becomes a powerful way to roughly estimate K_{eff}, for instance, through the derivative of the curve. For isolated particles, this estimation can also be done either by directly "matching" SAR values versus field intensity experimental curve to a model for dynamical loops, or by using some analytical formula, as proposed in the literature [15]. Note that, in general, the effective anisotropy constant, as estimated from SAR versus AC field curve, will include the contribution from dipolar interactions, particularly when MNPs are arranged in chains.

Also, the influence of the excitation frequency can be qualitatively understood within

the same framework provided by the SWMBTs because the simulations reproduce reasonably well the experiments (Figure 5.13). Simulations performed at different frequencies predict the marked contrast between the dispersion obtained in sample A (Figure 5.13 (a)), where curves of SAR/f versus field intensity at different frequencies strongly diverge and sample D, where these curves are mostly frequency independent (Figure 5.13 (d)).

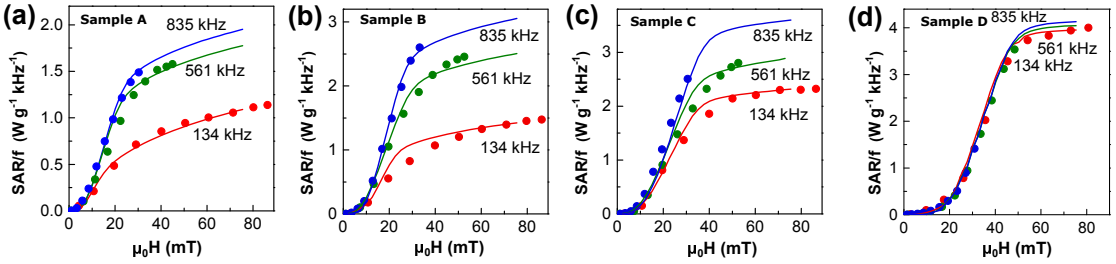

FIGURE 5.13: SAR/f versus field intensity curves obtained from the area of AC hysteresis loops at 134kHz (red), 561kHz (green) and 835kHz (blue) of samples (a) A, (b) B, (c) C and (d) D. The dots indicate measurements performed in frozen solutions and lines their corresponding simulations. SAR/f curve of sample D is frequency independent because all the curve collapse in a single curve, whereas those of sample A, B and C shows a frequency dependence.

5.3.3 The influence of particle size on *SAR*

If the AC excitation available is limited by technical or biomedical considerations the size of particles really matters to maximize SAR value [2, 20]. This question has been largely discussed in the literature. In brief, Linear Response Theory (LRT) [21] clearly predicts that the optimal size for particles of magnetite is situated around 18-20 nm [22]. We explicitly say magnetite because this optimal size depends ultimately on the anisotropy energy of the particle: it would be greatly different in cobalt containing ferrites or in Fe metallic alloys, for instance. But LRT only applies to small AC amplitudes. So, the existence or absence of a well-defined peak in the curves of SAR versus size of particles becomes a tricky question. The best answer is, that it depends on the excitation (frequency and field), and our results presented in Figure 5.14 confirm this point.

Figure 5.14 shows SAR/f as a function of particle's diameter at 22 mT, 28 mT and 45 mT magnetic field intensities. Figure 5.14 (a) and (b) present a maximum at 21 nm at 134 kHz frequency that shifts down to 19 nm at higher frequencies (561 and 835 kHz). In addition, hysteresis area (and SAR) of samples A and B increases very significantly with frequency (Figure 5.8 (e) and (f)). For higher field values (see Figure 5.14(c)), it is

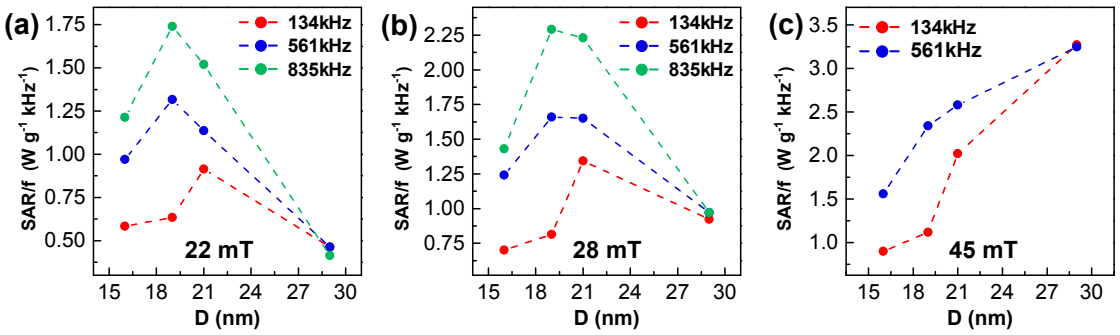

FIGURE 5.14: SAR/f versus particles' size curves at (a) 22 mT (b) 28 mT and (c) 45 mT magnetic field intensities and 134 kHz (red solid line), 561 kHz (blue solid line) and 835 kHz (green solid line) frequencies.

noteworthy that SAR/f clearly increases with particles' size (in the studied range), which is also evident by quick inspection of the major loops of each sample. This behavior has been successfully predicted by several authors [23, 24], using different models. Suffice it to say, that our results confirm the predictions of these models.

Additionally, this frequency driven effect reflects, in fact, the dependence of the coercive field on frequency. Indeed, it was also analyzed by Carrey *et al.* [15]. In this article, the coercive field is given by the following expression:

$$H_C/H_K = 0.48(1 - \kappa^{0.8}) \tag{5.5}$$

where H_K is the anisotropy field ($H_K = 2K_{eff}/\mu_0 M_s$) and the dimensionless parameter κ (proposed by Usov *et al.* [25]) takes the following form:

$$\kappa = \frac{k_B T}{K_{eff} V} ln\left(\frac{k_B T}{4\mu_0 H_{max} M_s V f \tau_0}\right) \tag{5.6}$$

where f is the frequency of the AC field, k_B the Boltzmann constant, μ_0 is the vacuum permeability and τ_0 represents a relaxation time depending on material properties (the gyromagnetic constant, magnetization, magnetic anisotropy) and experimental parameters (temperature, magnetic field). For simplicity, τ_0 can be fixed to 1.10^{-10} s. With most of parameters in Equation 5.6 being approximately equal for all magnetite samples, κ depends basically on the particle's volume and excitation frequency.

Figure 5.15 shows the dependence of κ and H_c/H_k for samples A-D. As observed, the influence of size makes a remarkably difference between samples: the coercive field

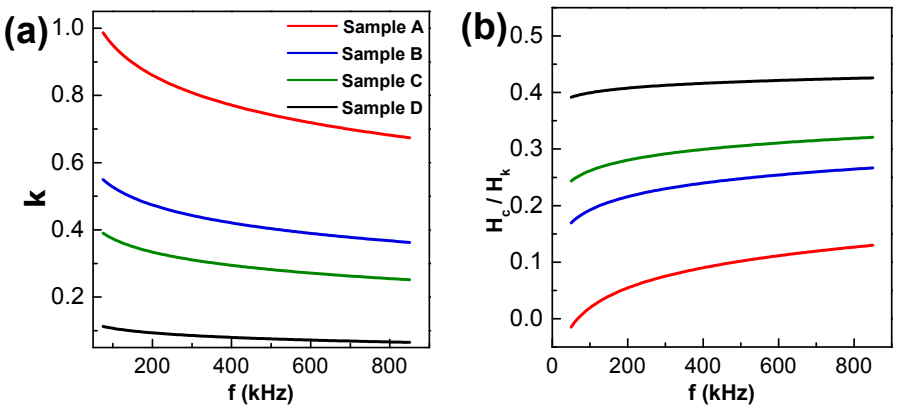

FIGURE 5.15: Expected dependence of dimensionless parameter κ on frequency for samples A-D according to Equation 5.6 . (b) Expected dependence on frequency of the ratio H_C/H_K according to Equation 5.5 for samples A-D, corresponding to average sizes of 16, 19, 21 and 29 nm, respectively.

of sample D (the largest one) is expected to change little (black curve) with frequency while, at the other end, the coercive of sample A (the smallest one) should be strongly dependent on frequency (red curve). These simulations confirm the results obtained using our AC magnetometer.

5.3.4 Optimizing the excitation conditions for practical magnetic hyperthermia treatment as a function of particles' size

As it is analyzed in Chapter 1, during the magnetic hyperthermia treatment eddy current produce an undesired heating on healthy tissue. The safety limits restrict the external magnetic field excitation that can be employed in magnetic hyperthermia. For this reason, the optimal magnetic field excitation parameters to maximize the SAR within human tolerable limit need to be calculated.

Magnetic field amplitude and frequency, for each sample can be deduced from the dependence on field amplitude of the SAR normalized by the frequency, SAR/f (Figure 5.8 (e)-(h)). Although different safety limits can be found in literature, for this analysis Hergt criterion $(H.f) < 5{\times}10^9$ $\mathrm{Am^{-1}s^{-1}}$ is considered. Given a field amplitude (H), the maximum acceptable frequency is determined by: $f_{limit}(H) = 5{\times}10^9$ $\mathrm{Am^{-1}s^{-1}}/H$, so the maximum achievable SAR (named as SAR_{limit}) can be calculated as:

$$SAR_{limit}(H) = \left(\frac{SAR}{f}\right)_{f_{limit},H} \cdot f_{limit}(H) = \left(\frac{SAR}{f}\right)_{f_{limit},H} \cdot \frac{5 \times 10^9}{H} \qquad (5.7)$$

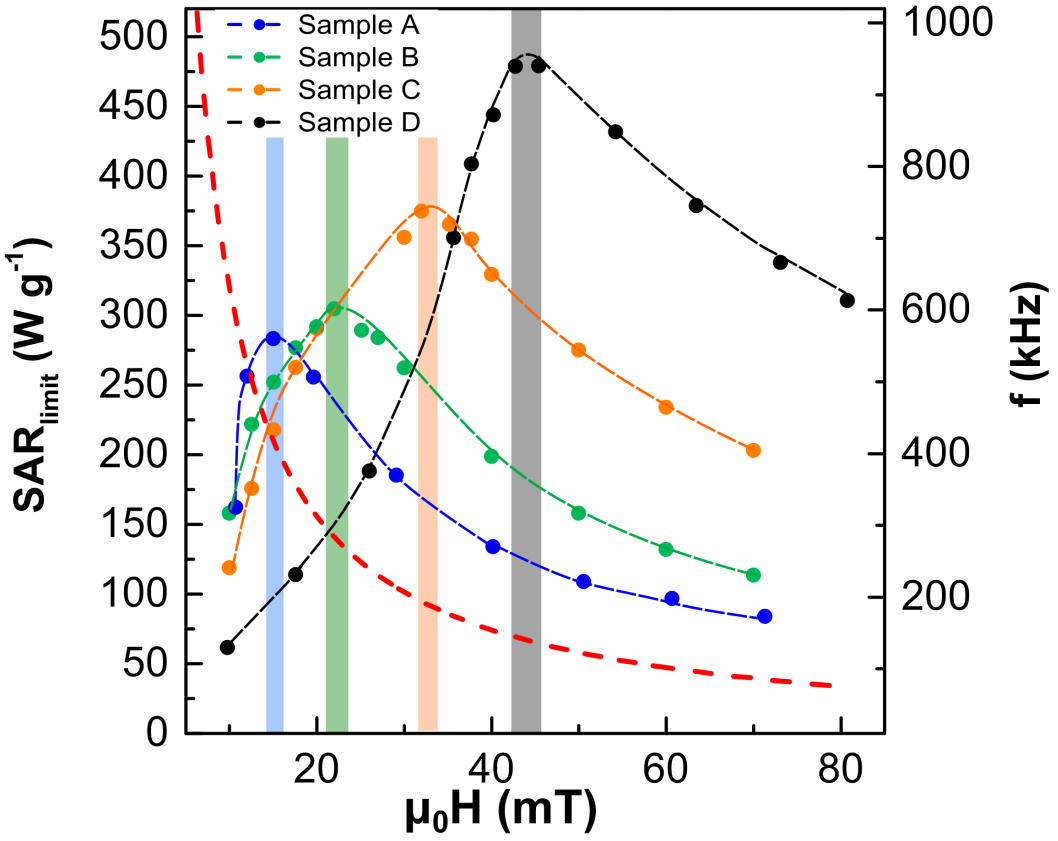

FIGURE 5.16: Maximum achievable SAR, SAR_{limit}, under the Hergt criterion for all the studied samples. The red dashed curve is the acceptable maximum frequency, $f_{limit}(\mathrm{H}) = 5{\times}10^9\ \mathrm{Am^{-1}s^{-1}}/H$, for a given magnetic field intensity following the Hergt criterion. The optimal excitation intensity to get the maximum SAR_{limit} value is indicated with colored bars (each color corresponds to one of the samples). The intersection of the red dashed curve and the colored bar of each sample shows the optimal frequency for obtaining the maximum SAR_{limit} value.

Note that SAR/f will be, in general, a function of the frequency as well as the field, so it must be calculated for $f = f_{limit}$, except in those cases where curves $SAR/f(H)$ collapse in a single universal curve, as in sample D. Since the experimental data and/or the corresponding modelling points are only available for three discrete frequencies, $SAR_{limit}(H)$ has been obtained by interpolation of the existing SAR/f curves, for sample A, B and C. Figure 5.16 shows the $SAR_{limit}(H)$ curve calculated from Equation 5.7 for the four samples, A-D. In this figure, the red dashed curve is the hyperbolic

function f_{limit}=5×10^9/H and serves up to determine which frequency corresponds to a given SAR_{limit}. The following features can be highlighted:

- All curves peak at some optimal magnetic field amplitude whose values are increasing with particle's size. Obviously, the corresponding working frequencies under the safety limit of Hergt are decreasing accordingly.
- Maxima of the curves $SAR_{limit}(H)$ are increasing with size, in such a way that larger particles can potentially produce more heat by choosing the appropriate excitation conditions. The maxima and the corresponding excitation parameters found are: Sample A, 285 Wg^{-1} at (15 mT and 417 kHz), Sample B, 305 Wg^{-1} at (22 mT and 284 kHz), Sample C, 375 Wg^{-1} at (32 mT and 195 kHz) and Sample D, 480 Wg^{-1} at (45 mT and 139 kHz).

Of course, previous features hold for a series of particles with similar composition and morphology. Finally, it is worthy to mention that determining these optimal conditions requires AC magnetometers as versatile as possible, meaning that the available field span and working frequencies should be broad enough.

5.4 Summary

In this chapter the potential of the high field, high frequency and temperature adjustable AC magnetometer has been analyzed. AC hysteresis loops and SAR values are measured in a test series of magnetite nanoparticles (16-29 nm) in liquid and frozen media at magnetic fields up to 90 mT and three different magnetic hyperthermia frequencies.

The designed AC magnetometer is able to generate magnetic fields high enough to saturate the MNPs employed in the studied samples. The obtained results indicate that the MNPs saturates at magnetic fields higher than 50 mT. To our knowledge is the first time that saturated AC hysteresis loops and SAR curves are obtained.

The AC hysteresis loops of liquid and frozen media are studied. The particles of the smallest size, sample A, show roughly similar AC hysteresis loops; whereas, the biggest size MNPs, sample D, produces a highly variable outcome in each medium: Squared AC hysteresis loop in water and titled and leaner in frozen medium. The temperature system

of the AC magnetometer has allowed us to decouple pure mechanical effects from the intrinsic relaxation of the magnetization. In this way, the squareness shape is associated to the ability of chain like formations (such as those observed in sample D) to orient their easy axis toward the applied magnetic field present in MNPs. So far, the immobilization of clusters of MNPs was done using agar medium. However, freezing MNPs dispersion media become more easy and reliable way to avoid any possible rotation of MNPs.

Another outstanding accomplishment is the experimental validation of SWMBTs. The impossibility of obtaining the saturation of MNPs has limited the confirmation of theoretical model. Consequently, some of the parameters obtained up to now from simulations, like magnetic anisotropy, were not accurately estimated.

Additionally, the ability of working in a wide magnetic field and frequency range allows us to study the influence of the size in the heating efficiency and verify theoretical models predicting their behavior.

Understanding the physical parameters that influence the heating efficiency is of extreme importance. However, considering that the real objective of the MNPs is being used in biomedical applications, analyzing the optimal excitation parameters to maximize heating production under human safety limits becomes even more important. So far, the experimental limitation of the current AC magnetometers restrains this kind of study, and consequently this issue is overlooked. In this chapter the optimal magnetic field intensity and frequency for maximizing the SAR within the safety limit have been calculated for each sample. From this data, the best samples for magnetic hyperthermia treatment can be obtained and selected.

Bibliography

[1] I. Rodrigo, I. Castellanos-Rubio, E. Garaio, O. K. Arriortua, M. Insausti, I. Orue, J. García, and F. Plazaola, "Exploring the potential of the dynamic hysteresis loops via high field, high frequency and temperature adjustable AC magnetometer for magnetic hyperthermia characterization," *International Journal of Hyperthermia*, vol. 37, no. 1, pp. 976–991, 2020.

[2] I. Castellanos-Rubio, I. Rodrigo, R. Munshi, O. Arriortua, J. S. Garitaonandia, A. Martinez-Amesti, F. Plazaola, I. Orue, A. Pralle, and M. Insausti, "Outstanding heat loss *via* nano-octahedra above 20 nm in size: from wustite-rich nanoparticles to magnetite single-crystals," *Nanoscale*, vol. 11, no. 35, pp. 16635–16649, 2019.

[3] B. D. Cullity and S. R. Stock, *Elements of X-ray Diffraction, Third Edition*. 2001.

[4] M. B. Fernández van Raap, P. Mendoza Zélis, D. F. Coral, T. E. Torres, C. Marquina, G. F. Goya, and F. H. Sánchez, "Self organization in oleic acid-coated CoFe2O4 colloids: a SAXS study," *Journal of Nanoparticle Research*, vol. 14, no. 9, p. 1072, 2012.

[5] Y. L. Raikher and V. I. Stepanov, "Absorption of AC field energy in a suspension of magnetic dipoles," *Journal of Magnetism and Magnetic Materials*, vol. 320, no. 21, pp. 2692–2695, 2008.

[6] N. A. Usov and B. Y. Liubimov, "Dynamics of magnetic nanoparticle in a viscous liquid: Application to magnetic nanoparticle hyperthermia," *Journal of Applied Physics*, vol. 112, no. 2, p. 023901, 2012.

[7] T. Yoshida and K. Enpuku, "Simulation and Quantitative Clarification of AC Susceptibility of Magnetic Fluid in Nonlinear Brownian Relaxation Region," *Japanese Journal of Applied Physics*, vol. 48, no. 12R, p. 127002, 2009.

[8] H. Mamiya, "Recent Advances in Understanding Magnetic Nanoparticles in AC Magnetic Fields and Optimal Design for Targeted Hyperthermia," 2013.

[9] G. Bertotti, *Hysteresis in Magnetism - 1st Edition*. 1998.

[10] D. Gandia, L. Gandarias, I. Rodrigo, J. Robles-García, R. Das, E. Garaio, J. García, M.-H. Phan, H. Srikanth, I. Orue, J. Alonso, A. Muela, and M. L.

Fdez-Gubieda, "Unlocking the Potential of Magnetotactic Bacteria as Magnetic Hyperthermia Agents," *Small*, vol. 15, no. 41, p. 1902626, 2019.

[11] A. Glaria, S. Soulé, N. Hallali, W.-S. Ojo, M. Mirjolet, G. Fuks, A. Cornejo, J. Allouche, J. C. Dupin, H. Martinez, J. Carrey, B. Chaudret, F. Delpech, S. Lachaize, and C. Nayral, "Silica coated iron nanoparticles: synthesis, interface control, magnetic and hyperthermia properties," *RSC Advances*, vol. 8, no. 56, pp. 32146–32156, 2018.

[12] J. M. Asensio, J. Marbaix, N. Mille, L.-M. Lacroix, K. Soulantica, P.-F. Fazzini, J. Carrey, and B. Chaudret, "To heat or not to heat: a study of the performances of iron carbide nanoparticles in magnetic heating," *Nanoscale*, vol. 11, no. 12, pp. 5402–5411, 2019.

[13] D. Cabrera, A. Coene, J. Leliaert, E. J. Artés-Ibáñez, L. Dupré, N. D. Telling, and F. J. Teran, "Dynamical Magnetic Response of Iron Oxide Nanoparticles Inside Live Cells," *ACS Nano*, vol. 12, no. 3, pp. 2741–2752, 2018.

[14] I. Castellanos-Rubio, I. Rodrigo, A. Olazagoitia-Garmendia, O. Arriortua, I. Gil de Muro, J. S. Garitaonandia, J. R. Bilbao, M. L. Fdez-Gubieda, F. Plazaola, I. Orue, A. Castellanos-Rubio, and M. Insausti, "Highly Reproducible Hyperthermia Response in Water, Agar, and Cellular Environment by Discretely PEGylated Magnetite Nanoparticles," *ACS Applied Materials & Interfaces*, vol. 12, no. 25, pp. 27917–27929, 2020.

[15] J. Carrey, B. Mehdaoui, and M. Respaud, "Simple models for dynamic hysteresis loop calculations of magnetic single-domain nanoparticles: Application to magnetic hyperthermia optimization," *Journal of Applied Physics*, vol. 109, no. 8, p. 083921, 2011.

[16] L. J. Geoghegan, W. T. Coffey, and B. Mulligan, "Differential Recurrence Relations for Non-Axially Symmetric Rotational Fokker-Planck Equations," in *Advances in Chemical Physics*, pp. 475–641, John Wiley & Sons, Ltd, 2007.

[17] A. Muela, D. Muñoz, R. Martín-Rodríguez, I. Orue, E. Garaio, A. Abad Díaz de Cerio, J. Alonso, J. García, and M. L. Fdez-Gubieda, "Optimal Parameters for

Hyperthermia Treatment Using Biomineralized Magnetite Nanoparticles: Theoretical and Experimental Approach," *The Journal of Physical Chemistry C*, vol. 120, no. 42, pp. 24437–24448, 2016.

[18] L. Marcano, D. Muñoz, R. Martín-Rodríguez, I. Orue, J. Alonso, A. García-Prieto, A. Serrano, S. Valencia, R. Abrudan, L. Fernández Barquín, A. García-Arribas, A. Muela, and M. L. Fdez-Gubieda, "Magnetic Study of Co-Doped Magnetosome Chains," *The Journal of Physical Chemistry C*, vol. 122, no. 13, pp. 7541–7550, 2018.

[19] V. R. R. Aquino, L. C. Figueiredo, J. A. H. Coaquira, M. H. Sousa, and A. F. Bakuzis, "Magnetic interaction and anisotropy axes arrangement in nanoparticle aggregates can enhance or reduce the effective magnetic anisotropy," *Journal of Magnetism and Magnetic Materials*, vol. 498, p. 166170, 2020.

[20] Z. Nemati, J. Alonso, I. Rodrigo, R. Das, E. Garaio, J. García, I. Orue, M.-H. Phan, and H. Srikanth, "Improving the Heating Efficiency of Iron Oxide Nanoparticles by Tuning Their Shape and Size," *The Journal of Physical Chemistry C*, vol. 122, no. 4, pp. 2367–2381, 2018.

[21] R. E. Rosensweig, "Heating magnetic fluid with alternating magnetic field," *Journal of Magnetism and Magnetic Materials*, vol. 252, pp. 370–374, 2002.

[22] I. Castellanos-Rubio, M. Insausti, E. Garaio, I. G. d. Muro, F. Plazaola, T. Rojo, and L. Lezama, "Fe3O4 nanoparticles prepared by the seeded-growth route for hyperthermia: electron magnetic resonance as a key tool to evaluate size distribution in magnetic nanoparticles," *Nanoscale*, vol. 6, no. 13, pp. 7542–7552, 2014.

[23] R. Hergt, S. Dutz, and M. Röder, "Effects of size distribution on hysteresis losses of magnetic nanoparticles for hyperthermia," *Journal of Physics: Condensed Matter*, vol. 20, no. 38, p. 385214, 2008.

[24] E. C. Vreeland, J. Watt, G. B. Schober, B. G. Hance, M. J. Austin, A. D. Price, B. D. Fellows, T. C. Monson, N. S. Hudak, L. Maldonado-Camargo, A. C. Bohorquez, C. Rinaldi, and D. L. Huber, "Enhanced Nanoparticle Size Control by Extending LaMer's Mechanism," *Chemistry of Materials*, vol. 27, no. 17, pp. 6059–6066, 2015.

[25] N. A. Usov and Y. B. Grebenshchikov, "Hysteresis loops of an assembly of superparamagnetic nanoparticles with uniaxial anisotropy," *Journal of Applied Physics*, vol. 106, no. 2, p. 023917, 2009.

Conclusions

The present Thesis provides a complete study of the development of a new versatile AC magnetometer and its potential, after a thorough study of the limitations of previous state of the art instrumentation in this field.

The main conclusions obtained are summarized in the following lines, organized along the three main blocks that compose this work:

1. AC magnetometry measurements to uncovered the parameters that influence the heating performance of MNPs and to study the shortcoming of the state of the art instrumentation.
2. Design and implementation of the new high field, high frequency and temperature adjustable AC magnetometer.
3. Analysis of the potential of the new AC magnetometer

1. Concerning to the first point:

   1.1. AC magnetometry has been demonstrated as a very reliable and useful technique to understand the parameters that influence the heating performances of MNPs:

   - In the case of *Magnetospirillum gryphiswaldense* magnetotactic bacteria, their high heating performance in water solutions is proven to be originated by the alignment of the bacteria along the magnetic field. This behavior has been deduced by comparing the square hysteresis loops arising both, in water dispersion media and in previously aligned bacteria in agar solution. Additionally, it has been found that the mechanical

rotation of the whole bacteria is not playing an important role, which is relevant because the bacteria will be able to produce heat in biological environments.

- Octahedral shape MNPs show biaxial magnetic anisotropy that generates square AC hysteresis loops and consequently high heating power. The high SAR coming from anisotropy is more desirable that those coming from arrangement formations, because their magnetic response remains invariable in biological environments.
- A new protocol to individually coat MNPs is developed via AC magnetometry. The length of the coating copolymer needs to be adjusted to the size of the MNPs: Larger particles require longer PEG molecules to avoid MNPs aggregation.

1.2. It has also been observed that the saturation region of MNPs is usually outside the experimental limits of the AC magnetometers employed up to now. That provides incomplete information about the magnetization dynamical properties of the MNPs.

2. In regard to the design and implementation of the new high field, high frequency and temperature adjustable AC magnetometer.

2.1. A versatile high field, high frequency and temperature adjustable AC magnetometer has been successfully designed, built and characterized.

2.2. The AC magnetometer is able to work in a large range of frequencies (50 kHz-1 MHz) and capable of applying remarkably higher field intensities that those existing so far: 90 mT at 50 kHz and 30 mT at the maximum frequency of 1 MHz. We have optimized the geometrical properties of the main coil that maximize the generated magnetic field intensity by using a power amplifier limited to 1 kW.

2.3. The AC magnetometer incorporates a temperature system to measure the AC hysteresis loops and SAR value of MNPs at different temperatures between 220 and 380 K.

2.4. An automatized control mechanism to shifting the pick-up coils inside the main one has been implemented. This allows to minimize the feedthrough signal in each measurement which improves the accuracy. In order to remove

the remaining feedthrough an additional shifting mechanism has been added that positions the sample inside each pick up coil for each measurement.

2.5. Magnetization has been successfully calibrated from major AC hysteresis loops, consequently the magnetization values measured with the developed AC magnetometer are highly reliable.

2.6. A home-made LabVIEW program controls the AC magnetometer and acquires and processes automatically the data.

3. With respecto to the analysis of the potential of the new AC magnetometer.

3.1. The magnetic field generated is able to saturate AC hysteresis loops and SAR curves of a series of magnetite MNPs (16-29 nm). The saturation of SAR strongly depends on particles' size and on the angular distribution of easy magnetization axes.

3.2. The temperature system allows to decouple mechanical effects from the intrinsic relaxation of the magnetization. This is very useful to study the influence of different arrangements on SAR.

3.3. The saturated AC hysteresis loops have enabled to accurately validate SWMBTs model. From the matching of the experimental and theoretical curves the effective anisotropy constant has been reliably estimated.

3.4. The wide working magnetic field available has allowed us to analyze the optimal excitation parameters to maximize MNPs heating production (SAR) under human safety limits.

Appendices

Appendix A

LCC resonant circuit

In this appendix the maximum power transference condition is analyzed.

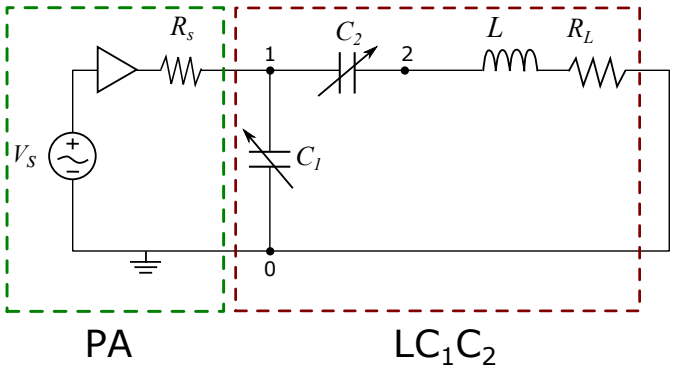

FIGURE A.1: Equivalent electrical circuit of the AC magnetometer. The power amplifier, PA, has real impedance, R_s, of 50 Ω. C_1 and C_2 are the variable capacitors and L and R_L the main coil's inductance and resistance.

The ratio between the actual power delivery to the resonant circuit, P_{LC1C2}, and the maximum power than can be delivered by the amplifier, P_{PA}, is given by Equation A.1:

$$\frac{P_{LC_1C_2}}{P_{PA}} = \frac{4.R_s.R_{LC_1C_2}}{(R_s + R_{LC_1C_2})^2 + (X_s + X_{LC_1C_2})^2} \tag{A.1}$$

where R_s and $R_{LC_1C_2}$ are the resistive parts of the amplifier, PA, and the resonant circuit, LC_1C_2, respectively. X_s and $R_{LC_1C_2}$ are the reactive parts of the amplifier and the resonant circuit, respectively.

$$R_{LC_1C_2} = \frac{X_1^2 R_L}{R_L^2 + (X_1 + X_2)^2} \tag{A.2}$$

$$X_{LC_1C_2} = X_1 \frac{R_L^2 + X_2(X_1 + X_2)}{R_L^2 + (X_1 + X_2)^2} \tag{A.3}$$

where $X_1 = -\frac{1}{2\pi f C_1}$ and $X_2 = 2\pi f L - \frac{1}{2\pi f C_1}$.
As the output impedance of the amplifier used in this Thesis is real (X_s=0 and R_s=50 Ω) the maximum transfer is obtained when the impedance value of the resonant is also real and approximately equal to the output impedance of the power amplifier.

Among all the possible pairs of capacitors values (C_1, C_2), the ones that approximately fulfill the maximum power transfer between the resonant circuit and the power amplifier are selected by measuring R_{LC1C2} using a network analyzer. Table A.1 shows the selected working frequencies, their corresponding (C_1, C_2) values and the power transfer value in the frequency range 100 - 1000 kHz.

$\mathbf{C}_1$ (nF)	$\mathbf{C}_2$ (nF)	**f** (kHz)	P_{LCC}/P_s
1190	shorted	134	0.952
510	shorted	205	0.999
340	1120	300	0.988
340	340	355	0.920
170	141	530	1.000
170	113	561	0.990
170	72	650	0.951
170	51	741.5	0.8487
170	37	835	0.655
170	28.3	939	0.462

TABLE A.1: Working frequency of the AC magnetometer, the corresponding (C_1,C_2) value and the power transfer value in the frequency range 100 kHz - 1 MHz.

Appendix B

Stoner Wohlfarth model

The influence of the applied field in the orientation of the magnetization of a single domain MNP assembly can be described by Stoner-Wohlfarth model [1]. In this model, the magnetization is able to take only discrete orientations, because the model assumes that thermal energy, k_BT, is much smaller than the anisotropy energy, $K_{eff}V$, being K_{eff} the anisotropy energy density and V, the particle volume.

The model is obtained from minimal energy arguments. The orientation of the magnetic moment is then governed by the competition among anisotropy energy, and Zeeman energy. For uniaxial non-interacting single domains MNPs, the energy is given by:

$$E(\theta, \phi, H) = E_A + E_Z = K_{eff}V \sin^2\theta - \mu_0 M_s V H \cos(\theta - \phi) \tag{B.1}$$

where θ is the angle between easy axis and magnetization, K_{eff} the effective uniaxial anisotropy,M_s the saturation magnetization, H the magnetic field and ϕ the angle between easy axis and magnetic field (see Figure B.1 (a)). Equation B.1 can be simplified dividing the energy by k_BT:

$$E/k_BT = K_{eff}V/k_BT \sin^2\theta - h\cos(\theta - \phi) \tag{B.2}$$

where $h = \mu_0 M_s V H/k_BT$.

Figure B.1 (b) displays the energy as function of the magnetic field and the angle θ for a $\phi = 30°$ magnetic field orientation. Two different shapes are visible: When $\mu_0 H$ is greater than the anisotropy field ($\mu_0 H_k = {}^{2K_{eff}}/_{M_s}$) , the energy displays only one minimum, which defines the equilibrium position, that is, along the anisotropy axis direction. On the other hand, when $\mu_0 H$ is less than $\mu_0 H_k$, the energy as a function of θ displays two minima at the coordinates (θ_1,E_1) and (θ_2, E_2).

As it can be seen from the figure, in the absence of applied field the magnetization can take two equivalent equilibrium values (θ_1=0° and θ_2=180°). For a positive h, the magnetic field initially favors one of the two minima (θ_1=0°, in this example). Increasing the applied magnetic field the abscissa of this minimum shifts, so, that the magnetization parallel to the magnetic field is favored. In Figure B.1 (b) the abscissa of the minimum tends towards $\theta_1 = 30°$. For a negative h, the other minimum is initially favored and tends towards θ_2=210°.

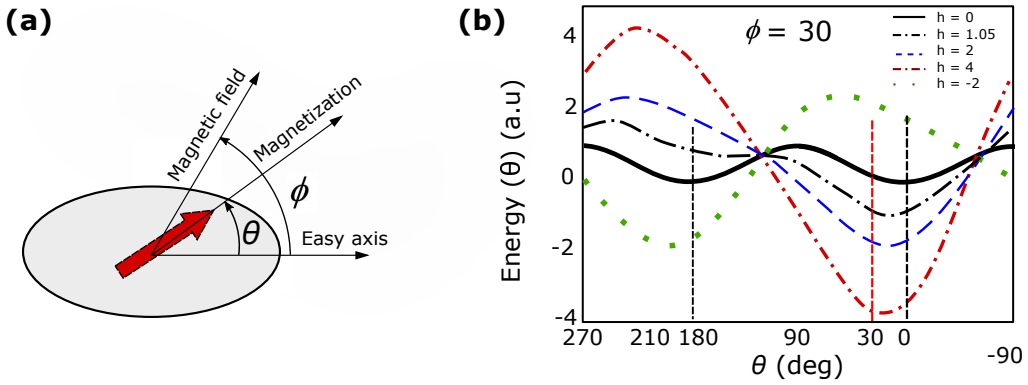

FIGURE B.1: (a) Angle distribution showing the direction of magnetization, magnetic field, and easy axis of a single domain MNP with unixial anisotropy. The red arrow presents the magnetization of the particle, θ the angle between the magnetization and the easy axis and ϕ the angle between magnetic field and the easy axis.(b) Energy as function of θ at $\phi = 30°$ magnetic field orientation and different reduced field values. The vertical black dashed lines, corresponds to the equilibrium position in absence of magnetic field (θ_1=0° and θ_2=180°) and red dashed line to magnetic field orientation. Figure adapted from [2].

The Stoner–Wohlfarth model does not take into account any thermal activation (T=0). As a consequence of neglecting thermal activation, the magnetization can only stay along one of the two equilibrium positions. At T=0 and when the magnetization is in one of the two minima of energy, the switch of the magnetization from the metastable state to the equilibrium position can only occur when the energy barrier is fully removed by the magnetic field.

Bibliography

[1] E. C. Stoner and E. P. Wohlfarth, "A mechanism of magnetic hysteresis in heterogeneous alloys," *Philosophical Transactions of the Royal Society of London. Series A, Mathematical and Physical Sciences*, vol. 240, no. 826, pp. 599–642, 1948.

[2] J. Carrey, B. Mehdaoui, and M. Respaud, "Simple models for dynamic hysteresis loop calculations of magnetic single-domain nanoparticles: Application to magnetic hyperthermia optimization," *Journal of Applied Physics*, vol. 109, no. 8, p. 083921, 2011.

Appendix C

Stoner Wohlfarth Model Based Theories

The influence of the applied field in the orientation of the magnetization, considering the effect of temperature of a single domain MNP assembly, can be described by Stoner-Wohlfarth Model Based Theories developed by Carrey *et al.* [1]. In this approach, the thermal energy can induce the magnetization to spontaneously switch between energy minima, when the applied field is below anisotropy field, at a rate w_{ij}, given by:

$$w_{ij}(t) = c_{ij} \exp(\Delta E_{ij} V / K_B T) \tag{C.1}$$

where V is the particle volumen, ΔE_{ij} is the energy barriers between energy minima (i and j) and pre-factor c_{ij} is the maximum jump rate related to the natural frequency of the particle magnetization, which has been considered a constant equal to 10^{-10} s

The dynamical problem to calculate magnetization, $M(t)$, is reduced to the calculation of the probabilities of finding the magnetization in any of the minimum energy states at a given time t. The time evolution of the probabilities, $p_i(t)$, can be calculated by solving a set of ordinary differential equations as:

$$\frac{\partial p_i}{\partial t} = \sum_{j \neq i} w_{ji} p_j - \left(\sum_{j \neq i} w_{ij} \right) p_i \tag{C.2}$$

Carrey *et al.* [1] developed the model, for the case of uniaxial single domain magnetic particles (two level model) where energy has two minima. Thus, the equation C.2 reduces to:

$$\frac{\partial p_{1(2)}}{\partial t} = w_{21(12)} p_{2(1)} - w_{12(21)} p_{1(2)} \tag{C.3}$$

Knowing the occupancy probabilities, the magnetization can be calculated according to:

$$M_\phi(t) = M_s(p_1 \cos(\theta_1 - \phi) + p_2 \cos(\theta_2 - \phi)) \tag{C.4}$$

To calculate the magnetization for a random magnetic field orientation, the magnetization should be averaged, over all the possible orientations of easy axis with respect to the applied magnetic field as:

$$M_{random} = \frac{\int_{\phi=\pi/2}^{\phi=0} M_H(t) \sin\phi d\phi}{\int \sin\phi d\phi} \tag{C.5}$$

Bibliography

[1] J. Carrey, B. Mehdaoui, and M. Respaud, "Simple models for dynamic hysteresis loop calculations of magnetic single-domain nanoparticles: Application to magnetic hyperthermia optimization," *Journal of Applied Physics*, vol. 109, no. 8, p. 083921, 2011.

Publications Originated from this Thesis

1. I. Rodrigo, I. Castellanos-Rubio, E. Garaio, O. K. Arriortua, M. Insausti, I. Orue, J. García, and F. Plazaola,"Exploring the potential of the dynamic hysteresis loops via high field, high frequency and temperature adjustable AC magnetometer for magnetic hyperthermia characterization," *International Journal of Hyperthermia*, vol. 37, no. 1, pp. 976–991, 2020.

2. I. Castellanos-Rubio, I. Rodrigo, A. Olazagoitia-Garmendia, O. Arriortua, I. Gil deMuro, J. S. Garitaonandia, J. R. Bilbao, M. L. Fdez-Gubieda, F. Plazaola,I. Orue, A. Castellanos-Rubio, and M. Insausti, "Highly Reproducible Hyperthermia Response in Water, Agar, and Cellular Environment by Discretely PEGylatedMagnetite Nanoparticles," *ACS Applied Materials & Interfaces*, vol. 12, no. 25,pp. 27917–27929, 2020

3. I. Castellanos-Rubio, I. Rodrigo, R. Munshi, O. Arriortua, J. S. Garitaonandia, A. Martinez-Amesti, F. Plazaola, I. Orue, A. Pralle, and M. Insausti, "Outstanding heat loss via nano-octahedra above 20 nm in size: from wustite-rich nanoparticles to magnetite single-crystals," *Nanoscale*, vol. 11, no. 35, pp. 16635–16649, 2019.

4. D. Gandia, L. Gandarias, I. Rodrigo, J. Robles-García, R. Das, E. Garaio, J. García, M.-H. Phan, H. Srikanth, I. Orue, J. Alonso, A. Muela, and M. L. Fdez-Gubieda, "Unlocking the Potential of Magnetotactic Bacteria as Magnetic Hyperthermia Agents," *Small*, vol. 15, no. 41, p. 1902626, 2019.

5. J. Alonso-Valdesueiro, B. Sisniega, I. Rodrigo, Perez-Muñoz, J.-M. Collantes, and F. Plazaola, "Design, Construction, and Characterization of a Magic Angle Field Spinning RF Magnet," *IEEE Transactions on Instrumentation and Measurement*, vol. 68, no. 10, pp. 4094–4103, 2019.

Other publications

6. I. Rodrigo, B. Herrero, E. Garaio, O. Arriortua, F. Plazaola, J.A García, J.J Echevarría-Uraga, M. Insausti, and I. García-Alonso, *"In vivo"* saiakerak kolon-ondesteko gibel metastasia hipertermia magnetikoaren bitartez tratatzeko, *IkerGazte2017 Nazioarte Ikerketa Euskaraz*, vol. Osasaun Zientziak, pp.108-113, 2017.

7. R. Das, C. Witanachchi, Z. Nemati, V. Kalappattil, I. Rodrigo, J. García, E. Garaio,J. Alonso, V. D. Lam, A.-T. Le, M.-H. Phan, and H. Srikanth, "Magnetic Vortex and Hyperthermia Suppression in Multigrain Iron Oxide Nanorings," *Applied Sciences*,vol. 10, p. 787, 2020.

8. Z. Nemati, J. Alonso, I. Rodrigo, R. Das, E. Garaio, J. García, I. Orue, M.-H. Phan,and H. Srikanth, "Improving the Heating Efficiency of Iron Oxide Nanoparticles by Tuning Their Shape and Size," *The Journal of Physical Chemistry C*, vol. 122, no. 4,pp. 2367–2381, 2018

9. G. Hemery, A. C. Keyes, E. Garaio, I. Rodrigo, J. A. García, F. Plazaola,E. Garanger, and O. Sandre, "Tuning Sizes, Morphologies, and Magnetic Proper-ties of Monocore Versus Multicore Iron Oxide Nanoparticles through the Controlled Addition of Water in the Polyol Synthesis," *Inorganic Chemistry*, vol. 56, pp. 8232–8243, 2017